National Laser Users' Facility and External Users' Programs

Under the facility governance plan implemented in FY08 to formalize the scheduling of the Omega Laser Facility as a National Nuclear Security Administration (NNSA) User Facility, Omega Facility shots are allocated by campaign. The majority of the FY15 target shots were allocated to the Inertial Confinement Fusion (ICF) Campaign conducted by integrated teams from Lawrence Livermore National Laboratory (LLNL), Los Alamos National Laboratory (LANL), Naval Research Laboratory (NRL), and LLE and the High-Energy-Density (HED) Campaigns conducted by teams led by scientists from the national laboratories, some with support from LLE.

The Fundamental Science Campaigns accounted for 24% of the Omega Facility target shots taken in FY15. Nearly half of these were dedicated to university fundamental science under the National Laser Users' Facility (NLUF) Program, and the remaining shots were allotted to the Laboratory Basic Science (LBS) Program, comprising peer-reviewed fundamental science experiments conducted by the national laboratories and by LLE, including the Fusion Science Center (FSC).

The Omega Laser Facility was also used for several campaigns by teams from the Commissariat à l'énergie atomique et aux energies (CEA) of France. These programs are conducted at the facility on the basis of special agreements put in place by DOE/NNSA and participating institutions.

The facility users during this year included 13 collaborative teams participating in the NLUF Program; 14 teams led by LLNL and LLE scientists participating in the LBS Program; many collaborative teams from the national laboratories conducting ICF experiments; investigators from LLNL and LANL conducting experiments for high-energy-density–physics programs; and scientists and engineers from CEA.

In this article, we briefly review all the external user activity on OMEGA during FY15.

FY15 NLUF Program

FY15 was the first of a two-year period of performance for the NLUF projects approved for FY15–FY16 funding and Omega Laser Facility shot allocation. Thirteen NLUF projects (see Table 144.XIV) were allotted Omega Laser Facility shot time and conducted a total of 198 target shots at the facility. The FY15 NLUF experiments are summarized in this section.

Fast-Electron Energy Coupling and Transport in Warm Dense Plasmas

Principal Investigator: F. N. Beg (University of California, San Diego)
Co-investigators: C. M. Krauland (University of California, San Diego); M. S. Wei (General Atomics); J. J. Santos (Centre Lasers Intenses et Applications, Université Bordeaux); W. Theobald and A. A. Solodov (LLE); and P. Keiter (University of Michigan)
Graduate Students: P. Belancourt (University of Michigan) and R. Hua (University of California, San Diego)

Understanding the transport physics and energy loss of an intense relativistic electron beam in warm dense matter is crucial for various high-energy-density systems, including advanced ignition schemes (e.g., fast ignition, shock ignition) and energetic proton source generation. This University of California, San Diego-led NLUF award is an international collaboration with General Atomics, LLE, University of Michigan, and University of Bordeaux that aims to perform a systematic investigation of fast-electron propagation in preassembled, uniform, large-volume plasmas under controlled conditions of density and temperature, including the examination of the effectiveness of resistive magnetic-field collimation of these electrons. Warm dense plasmas can be produced by high-energy, long-pulse, laser-driven shock compression and heating of a low-density foam or solid foil targets. In FY15, we performed a plasma characterization experiment of shocked carbonized resorcinol formaldehyde (CRF) foam and Al foil

Table 144.XIV: NLUF proposals approved for shots at the Omega Laser Facility for FY15–FY16.

Principal Investigator	Institution	Title
F. N. Beg	University of California, San Diego	Fast-Electron Energy Coupling and Transport in Warm Dense Plasmas
A. Bhattacharjee	Princeton University	Dynamics of Magnetic Reconnection and Instabilities of Current Sheets in High-Energy-Density Plasmas
R. P. Drake	University of Michigan	Experimental Astrophysics on the Omega Laser Facility
T. Duffy	Princeton University	Dynamic Compression of Earth and Planetary Materials Using the OMEGA Laser
P. Hartigan	Rice University	Magnetic Accretion Shocks and Magnetospheres in the Laboratory
R. Jeanloz	University of California, Berkeley	Exploring the Quantum Mechanics of Dense Matter
K. Krushelnick	University of Michigan	X-Ray Measurements of Laser-Driven Relativistic Magnetic Reconnection Using OMEGA EP
D. Q. Lamb	University of Chicago	Nonlinear Amplification of Magnetic Fields in Laser-Produced Plasmas
E. P. Liang	Rice University	Creation of a Magnetized Jet Using a Hollow Ring of Laser Beams
R. D. Petrasso	Massachusetts Institute of Technology	Explorations of Inertial Confinement Fusion, High-Energy-Density Physics, and Laboratory Astrophysics
A. Spitkovsky	Princeton University	Generation of Collisionless Shocks in Laser-Produced Plasmas
M.-S. Wei	General Atomics	Hot-Electron Scaling in Long-Pulse Laser–Plasma Interactions Relevant to Shock Ignition
L. Willingale	University of Michigan	High-Energy Electron-Beam Acceleration from Underdense Plasma Using OMEGA EP

in order to understand those plasma conditions prior to the addition of an intense relativistic electron beam produced from high-intensity, short-pulse laser–matter interaction.

The OMEGA EP experiment employed a laser configuration of one UV beam smoothed by an SG8 (eighth-order super-Gaussian spatial profile) distributed phase plate (DPP) with a 4-ns square pulse for an intensity of roughly 1.8×10^{14} W/cm^2 to launch a shock into both materials being evaluated. In the case of the CRF foam (340-mg/cm^3 initial mass density), a target platform being developed at LLE for x-ray Thomson scattering was utilized. This required the creation of an x-ray source, which used the remaining three UV beams with the same SG8 DPP's and a total of 6.1 kJ in a 2-ns pulse duration. These beams diverged into a 750-μm spot incident on a 20-μm Ni foil mounted such that the x-ray emission from the coronal plume directed 50° off of the foil normal will interact with the CRF foam (see Fig. 144.52). We used the imaging x-ray Thomson spectrometer (IXTS) with a toroidally bent crystal to resolve both the spectral shift of scattered (primarily) Ni He$_\alpha$ x rays and the spatial position of the propagating shock wave. X rays scattered at a 90° angle were observed with the IXTS. This diagnostic allows us to confidently deduce the temperature,

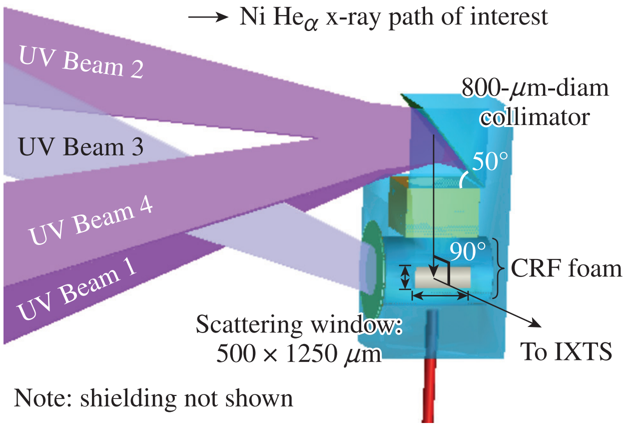

Figure 144.52
Schematic of the carbonized resorcinol formaldehyde (CRF) foam target in the OMEGA EP chamber. UV Beam 3 irradiates a 30-μm CH ablator in front of a 10-μm Cu tracer and 2.35-mm-long, 340-mg/cm^3 CRF foam encased in a large plastic superstructure. UV Beams 1, 2, and 4 are incident on a 20-μm Ni foil mounted above and at a 50° angle to the CRF target axis such that x-ray emission passes through a Ta collimator before scattering off of the foam and being collected at a 90° angle with the imaging x-ray Thomson spectrometer (IXTS).

ionization state, and density of the warm dense plasma in the spatially resolved scattering volume (along the shock propagation direction); time delaying of the x-ray source beams allows us to probe at various shock positions in the foam.

Results shown in Fig. 144.53 suggest an average shock velocity of 10 km/s and an average Compton shift of 110 eV. Ongoing spectral fit analysis with the x-ray scattering (XRS) code (provided by G. Gregori at the University of Oxford) uses the experimental Ni spectrum to compute theoretical scattering profiles over a 2-D parameter space created from varying the temperature and ionization inputs and will produce best-fit inferred values for those parameters.

For the Al foil configuration, we used a machined step target to detect shock breakout at different thicknesses of the material in a single shot. The streaked optical pyrometry (SOP) system was used to measure the time-resolved self-emission in the ~600- to 750-nm-wavelength range at the back of a target (see Fig. 144.54). The shock propagation velocity inferred from the SOP measurement is 28.6 km/s, which will be used to benchmark radiation hydrodynamic modeling using the

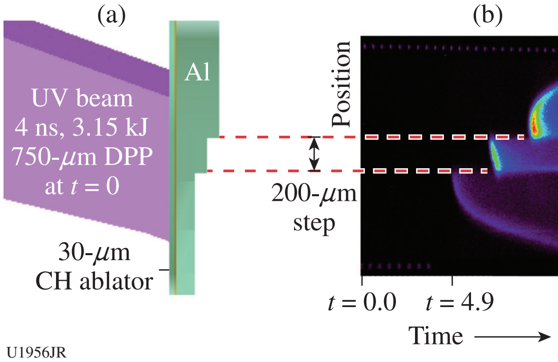

Figure 144.54
(a) Zoomed schematic of a target in the OMEGA EP target chamber. A single 4-ns UV beam is incident upon a 30-μm CH ablator layer, which is followed by a 10-μm Cu tracer and then machined Al steps where the layer thicknesses are 100 μm, 170 μm, and 240 μm. (b) Streaked optical pyrometry (SOP) data showing the shock breakout of the rear of each step layer, averaging a velocity ~28 km/s over the entire target thickness.

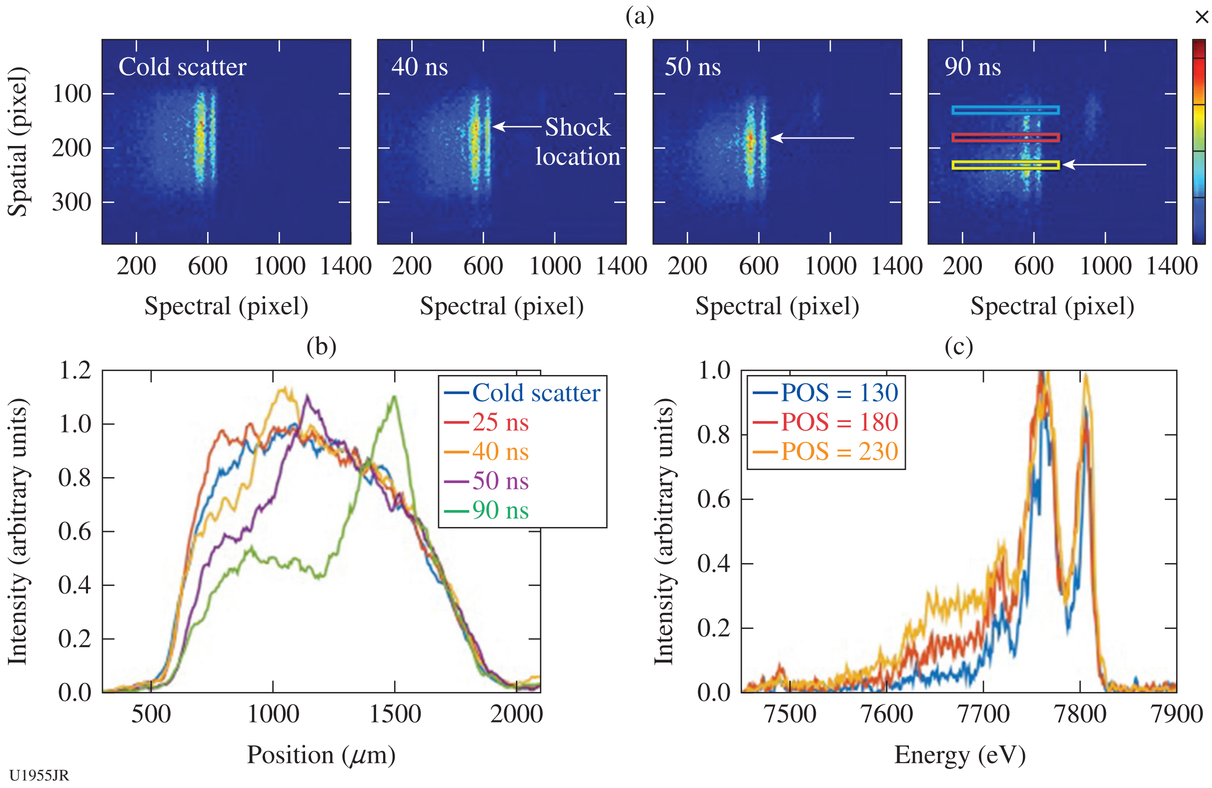

Figure 144.53
(a) Raw IXTS data for scattering off of (left to right) an undriven foam, and a driven foam at 40 ns, 50 ns, and 90 ns after initial laser ablation for shock creation. The vertical axis shows the spatial dimension for an ~1250-μm section of the foam, and shock travels down in the image in time. (b) Spatial lineout comparison of five separate shots showing shock propagation through foam, suggesting a 10-km/s average velocity. (c) Spectral lineouts, normalized to the height of the elastic peak, corresponding to a 90-ns shot (top rightmost frame) at different spatial positions, show the Compton shift sensitive to temperature ionization.

1-D *HYADES* and 2-D *FLASH* codes to obtain shock pressure and other plasma parameters. The information obtained about the shock propagation and the condition of the shocked warm dense plasma provides the basis for our planned fast-electron transport study in FY16.

Experimental Astrophysics at the Omega Laser Facility

Principal Investigators: R. P. Drake, C. C. Kuranz, and P. A. Keiter (University of Michigan)
Co-investigators: G. Malamud, Y. Elbaz, and D. Shvarts (University of Michigan and Nuclear Research Center, Israel); B. van der Holst (University of Michigan); and A. Frank and E. Blackman (University of Rochester)

Our work on this project includes research in radiation hydrodynamics and complex hydrodynamics. In the present report, we focus on the latter. Hydrodynamic instabilities in fluid and plasma flows can lead to the development of small-scale structure and the intermixing of fluids in both natural and engineering systems. It is important to understand the behavior of these instabilities in high-energy-density systems to ensure that we can properly predict and understand the data from fusion experiments and astrophysical research. The Kelvin–Helmholtz instability (KHI) is found in shear flows, where small modulations create forces that cause small perturbations to evolve into "roll-ups" that eventually become turbulent. In a supersonic flow, some of the energy that would contribute to the growth of the instability is instead used to support the compression of the fluids, reducing the growth rate of the KHI.

The advanced capabilities of the OMEGA EP Laser System enabled us to design experiments capable of probing the evolution of the KHI in unprecedented detail.[1] Our target design, illustrated in Fig. 144.55(a), utilizes three 10-ns beams fired in sequence to create a 28-ns, 12.5-kJ, nominally square pulse with a 1.1-mm-diam spot size. The resulting ablation pressure can sustain a shock wave for roughly 70 ns before the velocity begins to decay. In the upper layer of the target, the shock wave propagates to the right into carbon foam of 0.1-g/cm^3 density. In the lower layer, the presence of a dense shock blocker prevents the shock wave from directly entering the 1.4-g/cm^3 plastic (on time scales of interest). Instead, the pressure in the shocked foam drives a shock down into the plastic, creating a shear flow between the shocked foam and the shocked plastic. The initial plastic surface is precision machined to have a sinusoidal modulation with an initial wavelength of 100 μm and initial amplitude of 5 μm. This seed perturbation evolves under the influence of the KHI until it is disturbed by the presence of entrained material from the driver section. Figure 144.55(b) shows the spatial profile of density from a 2-D simulation of the experimental system using the code *DAFNA*.

We used this platform to obtain the first observations of the evolution of the KHI from well-defined, single-mode seed perturbations in a supersonic flow, as part of the doctoral thesis research of W. C. Wan.[3] The primary diagnostic was a spherical crystal imager that recorded a radiograph of the Cu K_α x rays transmitted through the target using an image-plate detector. Figure 144.56 shows a sample of the radiographic data. One

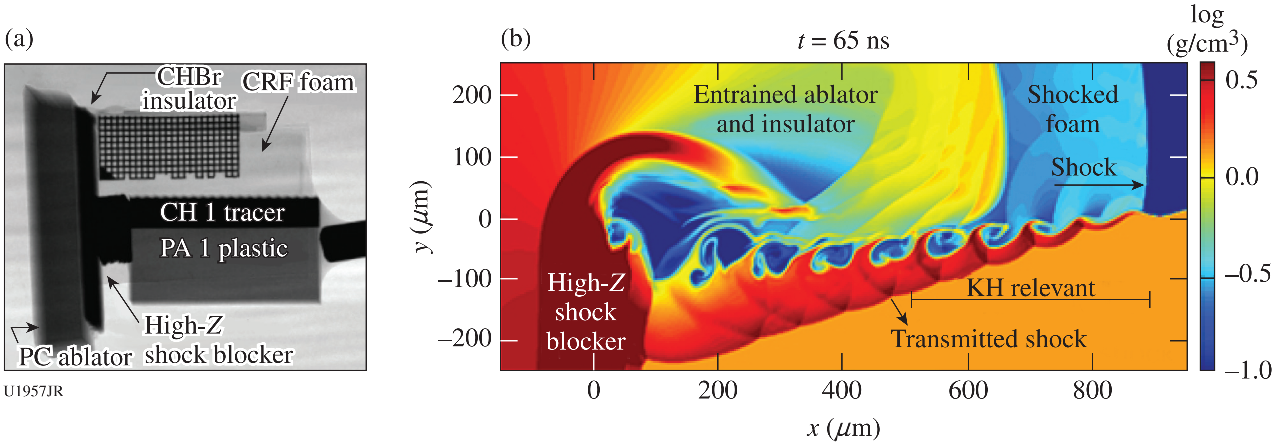

Figure 144.55
(a) Radiographic image of an unshocked target (Credit J. Cowan).[2] The laser beams are incident from the left. (b) Density plot from a 2-D *DAFNA* simulation (adapted from Ref. 3). The KHI develops behind the shock, which is moving to the right, at the interface with the shocked plastic, which has been deflected downward.

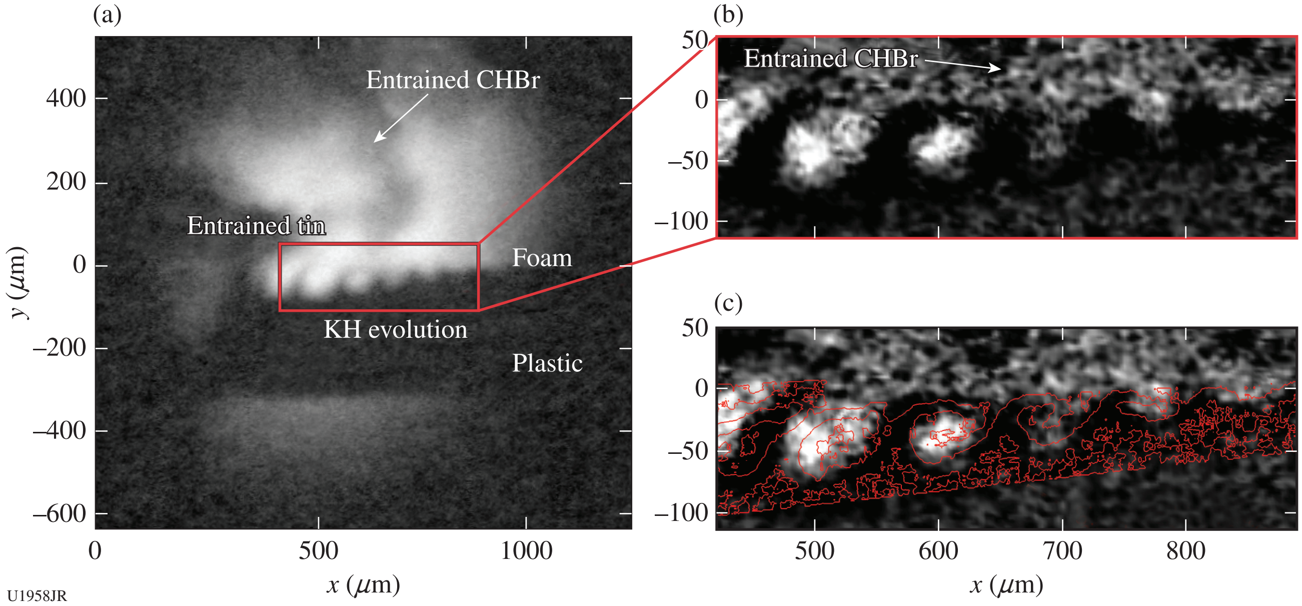

Figure 144.56
(a) Raw radiographic data; (b) contrast-enhanced data; (c) interface extracted from the *DAFNA*-simulated radiograph and overplotted onto the experimental data (adapted from Ref. 3).

can see from Fig. 144.56(c) that the interface extracted from the simulations, featured in red, is in good agreement with the data until it is disturbed by the entrained driver material at $x \sim 600$ μm. There are discrepancies on spatial scales near our diagnostic resolution limit (~10 to 15 μm) that could be the result of instrumental limitations, experimental variability, or true errors in how simulation codes handle the development of small-scale structures and turbulence. Future experiments can seek to explore these discrepancies.

Dynamic Compression of Earth and Planetary Core Materials on OMEGA

Principal Investigator: T. Duffy (Princeton University)
Co-investigators: J. Wicks (Princeton University); R. Smith, R. Kraus, and F. Coppari (LLNL); M. Newville (California Institute of Technology); and T. R. Boehly (LLE)

The earth's core is composed of iron alloyed with lighter elements, the identity of which is crucial for understanding the bulk chemistry of the earth and for constraining the process of core formation. The iron/light-element alloy controls phase relationships and melting temperatures in the core and may influence potential chemical reactions between the core and mantle. Silicon is a strong candidate for the core's major light element based on both cosmochemical and geochemical considerations. In addition to the earth, there is strong interest in understanding the interior structure of the large rocky exoplanets that have been discovered in recent years. These extrasolar planets have internal pressures that are up to an order of magnitude larger than those in the earth, making them inaccessible to conventional experimental techniques. In this study, we used OMEGA to compress an Fe/Si alloy to pressures equal to and beyond those of the center of the earth. This work is part of a continued collaboration among Princeton University, Lawrence Livermore National Laboratory, and the University of Rochester.

Laser ramp-compression experiments on Fe/Si alloys were carried out to a maximum pressure above 1200 GPa. Six OMEGA laser beams in a ramp-shaped drive were focused onto a target package, which consisted of an annealed pellet of Fe/7-wt% Si alloy sandwiched between two diamonds or between a diamond ablator and an LiF window (Fig. 144.57). While at peak compression, the sample was illuminated with quasi-monochromatic x rays produced by laser irradiation of Cu, Fe, or Ge foils. *In-situ* powder x-ray diffraction patterns were collected using the powder x-ray diffraction image plate (PXRDIP) diagnostic (Fig. 144.57).

Diffraction patterns are consistent with the stability of a hexagonal close-packed (hcp) alloy over the entire measured pressure range. In Fig. 144.58(a), our measured interplanar *d*-spacings (circles) are consistent with static 300-K diamond anvil cell (DAC) data at low pressures but extend the measured pressure range by a factor of 6. Our results indicate that alloying geophysically relevant amounts of Si into Fe does change the

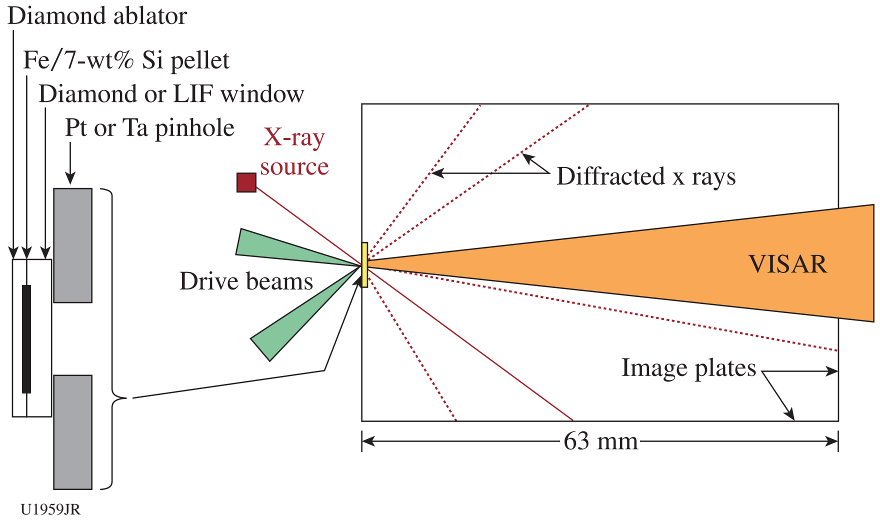

Figure 144.57
Schematic of dynamic ramp-compression experiments with *in-situ* x-ray diffraction.

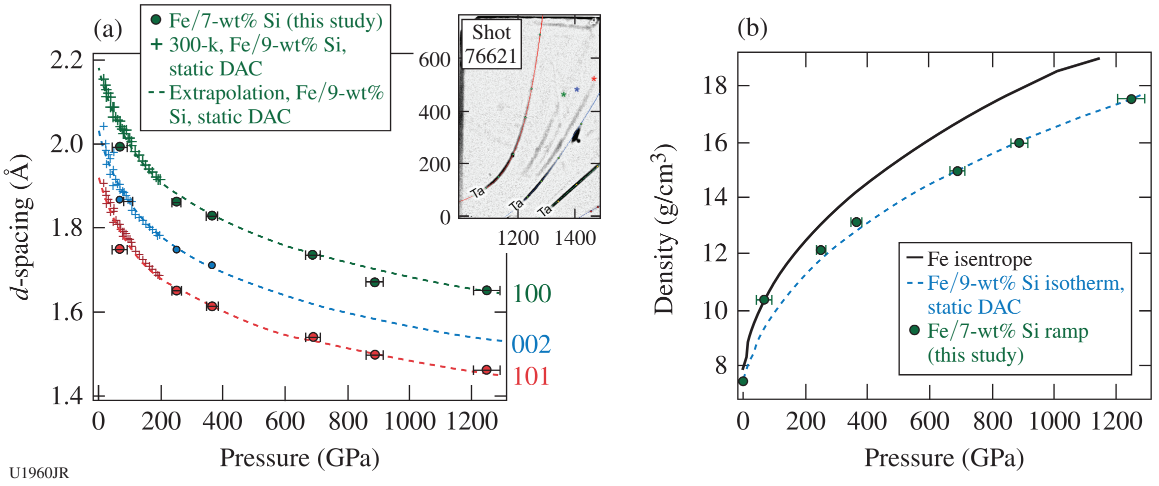

Figure 144.58
(a) Measured interatomic *d*-spacings of Fe/7-wt% Si alloy as a function of pressure obtained by x-ray diffraction in ramp-compression experiments on OMEGA. The inset plots an image plate with diffraction lines recorded from a sample at 365 GPa showing a triplet of reflections consistent with the hcp crystal structure. Colored asterisks denote reflections corresponding to colors in the main figure. (b) Compression behavior of the Fe/7-wt% Si alloy as determined by the measured *d*-spacings in (a). For comparison, a calculated isentrope for Fe and an extrapolated isotherm for Fe/9-wt% Si are also shown.

stability of the hcp phase at high pressure. The addition of Si produces a significant change, however, in the compressibility: the pressure–density relationship of Fe/7-wt% Si alloy deviates from the calculated isentrope of end member Fe [Fig. 144.58(b)].

Our study provides direct evidence that an Fe/Si alloy in the earth's solid inner core would adopt the hcp crystal structure. This structure would be expected to remain stable in Si-containing cores for terrestrial-composition planets up to at least four earth masses in size. In combination with data on pure iron, our study will also enable us to determine the density change associated with Si alloying at core pressures. These constraints on the core composition of exoplanets will enable one to develop better models of their interior structure and the evolution of the earth and extrasolar planets.

High-Pressure Phase Transitions in Forsterite as Determined by **In-Situ** *X-Ray Diffraction*

NLUF Principal Investigator: T. Duffy (Princeton University)
Shot Principal Investigator: R. G. Kraus (LLNL)
Co-investigators: M. G. Newman and J. Wicks (Princeton University) and R. Smith and F. Coppari (LLNL)

Our understanding of the high-pressure and temperature properties of magnesium silicates such as forsterite is critical to our understanding of the deep earth as well as the mantles of super earths. The objective of this NLUF campaign was to measure the high-pressure properties of forsterite along its principal Hugoniot from 100 to 200 GPa. In particular, we measured thermodynamic states near the solid–liquid phase boundary, searching for decomposition of forsterite into periclase + bridgmanite.

We performed seven shots, varying the laser energies to measure the properties of forsterite at several different pressures. The primary diagnostics for this campaign were VISAR (velocity interferometer for any reflector) and PXRDIP, both of which produced excellent data. The VISAR data are used to measure the interface velocity between our sample and a lithium fluoride window. This velocity is then used to determine the pressure in the forsterite sample while the x rays probe the sample. For the lowest-energy shots, we saw an elastic precursor wave in the forsterite, which was an interesting and unexpected physical phenomenon to observe at this high of a pressure. The PXRDIP diagnostic is used to probe the crystal lattice structure of the forsterite sample in the shock state. Notably, we saw intense diffraction peaks give way to diffuse scattering for the highest-energy experiments, indicating a transition from a solid to a liquid state. This provides a valuable constraint on the melting curve of this material.

Magnetized Accretion Shocks and Magnetospheres in the Laboratory

Principal Investigator: P. Hartigan (Rice University)
Co-investigators: C. Kuranz, M. Trantham, and R. Young (University of Michigan); J. Foster and P. Graham [Atomic Weapons Establishment (AWE), UK]; G. Fiksel (University of Wisconsin, Madison); A. Frank (University of Rochester); A. Liao (Rice University); and C. K. Li (MIT)

Supersonic magnetized flows occur in many astrophysical contexts and affect the evolution of both stellar and planetary objects. As part of our NLUF campaign in the past year, we developed experiments designed to explore two supersonic flow phenomena—accretion flows and magnetospheres. The long-term goal is to create a platform that we can use to study strongly magnetized, high-Mach-number shock waves in a controlled laboratory environment, with applications to stellar winds, jets from young stars and black holes, interacting binary systems, planetary magnetospheres, and exoplanet evolution.

Results of the accretion column experiment are shown in Fig. 144.59. A collimated flow results as the lasers illuminate a cone-shaped target, and the flow proceeds through a gap and impacts upon a surface. Diagnostics included the optical imager and, for the magnetized experiments, proton radiography. The images below demonstrate that the experimental design successfully reproduces a collimated shocked system, but we were unable to see any clear effects from imposing an ~8-T magnetic field upon the system with the magneto-inertial fusion electrical discharge system (MIFEDS) coils. We are in the process of redesigning the drive of the experiment to produce a lower ram pressure while retaining sufficient ionization to minimize magnetic diffusion. These experiments form the basis of the Ph.D. thesis of R. Young at Michigan.

Our second set of experiments involved creating a magnetosphere analog by propagating a supersonic flow past a current-carrying wire. Numerical simulations show that for fields like those realized with the MIFEDS coils, pressure from the magnetic field that surrounds the wire will induce a measurable offset of the bow shock from the wire. Our experiment

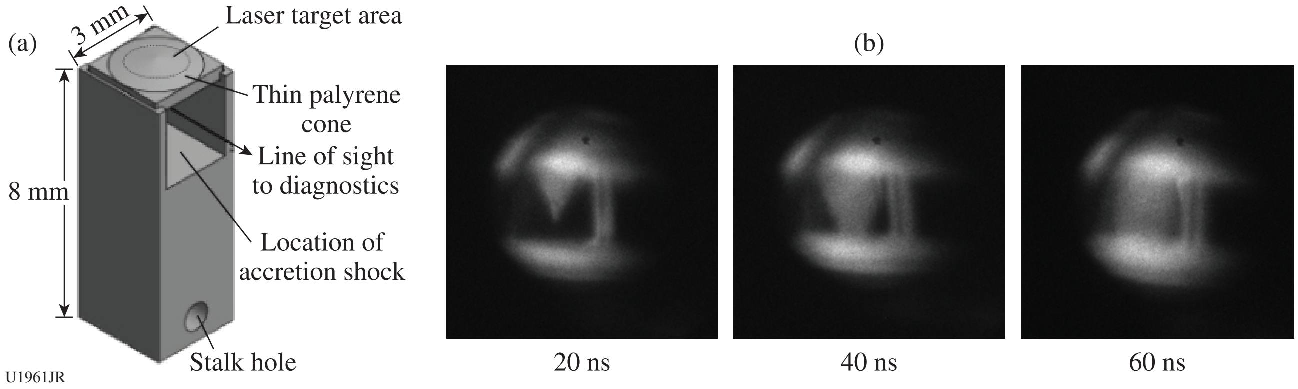

Figure 144.59
Accretion shock experiment. (a) Target design. A collimated flow emerges from the laser irradiation area and impacts a surface, developing an accretion shock. (b) Experimental data. These three optical images show how the collimated flow progresses with time.

drove a strong shock past the wire and analyzed the resulting bow shock with both streaked optical pyrometry and optical imaging as diagnostics.

Results from the first attempt at these experiments are shown in Fig 144.60. Some differences appear between the magnetic and nonmagnetic cases in both the images and streaked optical pyrometer (SOP) data. However, the interpretation is complicated by ablation from the wire that sets up an outward flow that interacts with the incident blast wave from the laser drive as it accelerates material from the target. As with the accretion column work, we are currently testing new ideas for drives that will provide a longer, more-steady ionized flow with lower ram pressure to help make the magnetic dynamical effects more readily visible.

Exploring the Quantum Mechanics of Dense Matter

Principal Investigator: R. Jeanloz (University of California, Berkeley)

Co-investigators: P. Loubeyre and S. Brygoo (CEA); M. Millot, R. Rygg, J. Eggert, P. Celliers, and G. Collins (LLNL)

In FY15, the University of California, Berkeley–CEA–LLNL team continued to explore the properties of warm dense hydrogen isotopes at extreme density using ultrafast optical diagnostics under shock compression. We conducted two half days of experiments, using a 6-kJ, 1-ns drive to launch strong shocks in hydrogen precompressed to 12 GPa—twice the maximum precompression achieved previously on OMEGA. Active shock breakout (ASBO, velocimetry) and SOP (pyrometry) were used to monitor the shock-front velocity, reflectivity/absorptivity, and

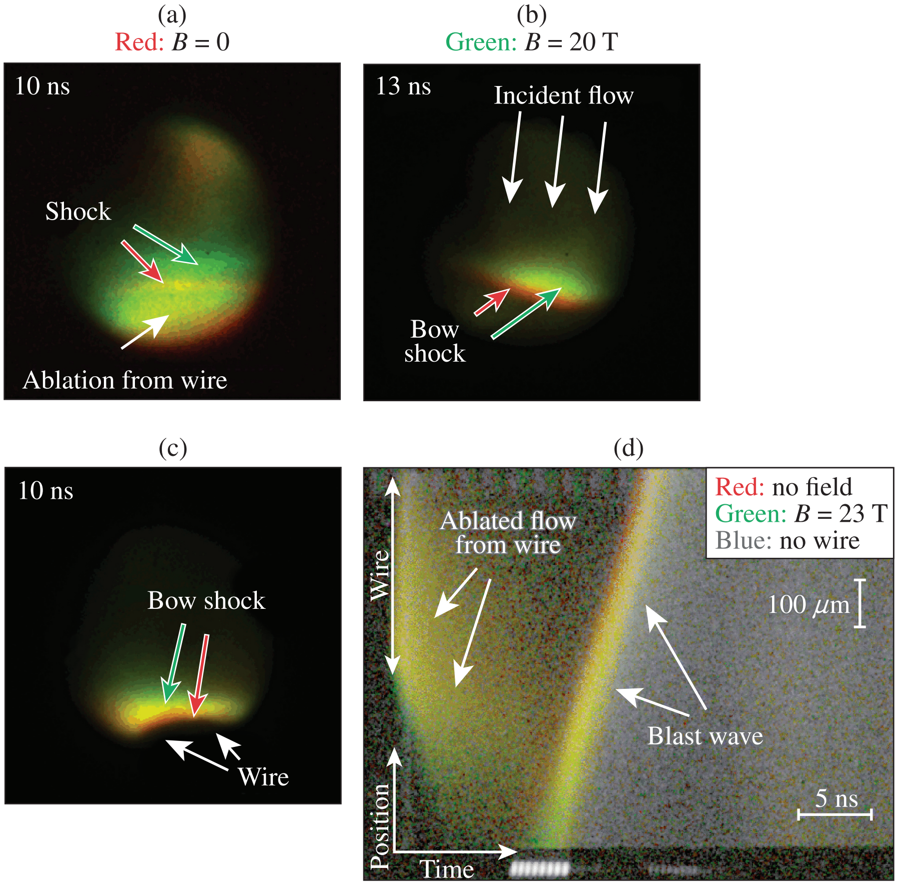

Figure 144.60
Magnetosphere experiment. [(a)–(c)] Optical images of the bow shock that forms around a wire. The color offset between the red and green shocks suggests an offset in the sense one would expect for a magnetic field, but the effect is near the limit of the spatial resolution in the data. (d) Streaked optical pyrometer (SOP) image of the blast wave as it moves past the wire. At early times there is significant ablation from the wire in response to irradiation from the laser drive.

thermal emission during its travel in the hydrogen layer and in the quartz reference plate (Fig. 144.61). Using impedance matching, new pressure–density–temperature equation-of-state data were obtained, and new data were collected on the metallization of hydrogen at unprecedented conditions approaching the predicted plasma-phase transition. In parallel, the team also developed an indirect-drive platform, with first shots planned for the first quarter of FY16, to pave the way for future NIF experiments.

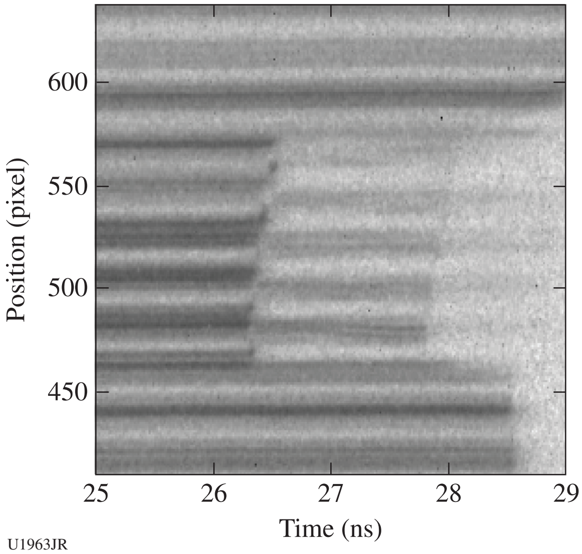

Figure 144.61
Raw velocimetry [active shock breakout (ASBO)] data for an ~2-Mbar reflecting shock in deuterium precompressed to 12 GPa, which will provide new insight into hydrogen's insulator-to-metal transition.

X-Ray Measurements of Laser-Driven Relativistic Magnetic Reconnection Using OMEGA EP

Investigators: K. Krushelnick, A. Raymond, L. Willingale, A. Thomas, and T. Batson (University of Michigan); P. M. Nilson and C. Mileham (LLE); G. J. Williams and H. Chen (LLNL); and W. Fox (Princeton University)

The interaction of two relativistic intensity laser pulses ($I \gtrsim 10^{18}$ W/cm^2) with an overdense plasma has been used to investigate magnetic reconnection (MR) in a relativistic electron-driven regime. To generate the MR geometry, two 20-ps pulses, with energies of either 500 J or 1000 J each, were focused with a variable separation of 250 to 1000 μm onto a copper foil. The radially expanding relativistic electron current generates azimuthal magnetic fields around each focal spot, so that opposing field lines are driven together in the focal midplane. The breaking and reconnecting of opposing field lines requires the generation of a target-normal electric field. This is directed to drive electrons into the dense copper target within a localized midplane region. A spherical crystal imager (SCI) for copper K_α x rays was utilized to image the x-ray emission. This indicates regions of hot electrons within the target and clearly shows an enhancement in the midplane region. Figure 144.62 depicts the SCI results as a function of the pulse energy and focal-spot separation.

The brightness of the midplane emission, along with its dimensional characteristics, may be used to determine the optimal conditions for MR. A single photon counter (SPC)

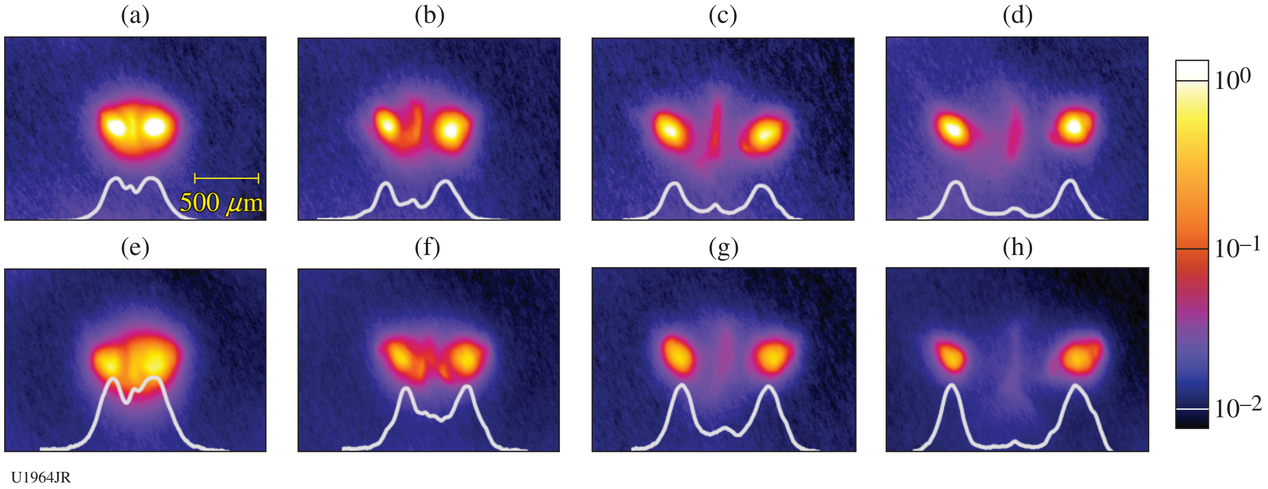

Figure 144.62
Spherical crystal imager (SCI) results observing copper K_α emission from copper foil targets as a function of a pulse energy of [(a)–(d)] 500 J and [(e)–(h)] 1 kJ and focal separation (250 μm, 500 μm, 750 μm, and 1000 μm from left to right). The two regions of focal-spot heating are visible, as well as an enhanced midplane, where electrons are driven into the target by an electric field generated during MR.

was utilized to collect front-side x-ray emissions and guarantee the midplane region brightness recorded by the SCI is not artificially affected by K_α spectral shifting. Three-dimensional particle-in-cell simulations are underway to understand the role of the relativistic electrons in generating the azimuthal magnetic fields and their behavior in the midplane region during MR. In particular, the comparison to similar geometries generated by lower-intensity, nanosecond-duration lasers warrants significant interest because of the higher magnetic-field magnitudes and faster electrons participating in the interaction in the relativistic case.

Nonlinear Amplification of Magnetic Fields in Laser-Produced Plasmas

Principal Investigator: D. Q. Lamb (University of Chicago)

The experiments (TDYNO NLUF Campaign) we performed on OMEGA during our first shot day (14 July 2015) studied one of the greatest puzzles of modern astrophysics: the generation and amplification of magnetic fields ubiquitously found in the universe [Fig. 144.63(a)]. The experiments aim to demonstrate nonlinear amplification of magnetic fields by the turbulent dynamo mechanism—a process that is believed

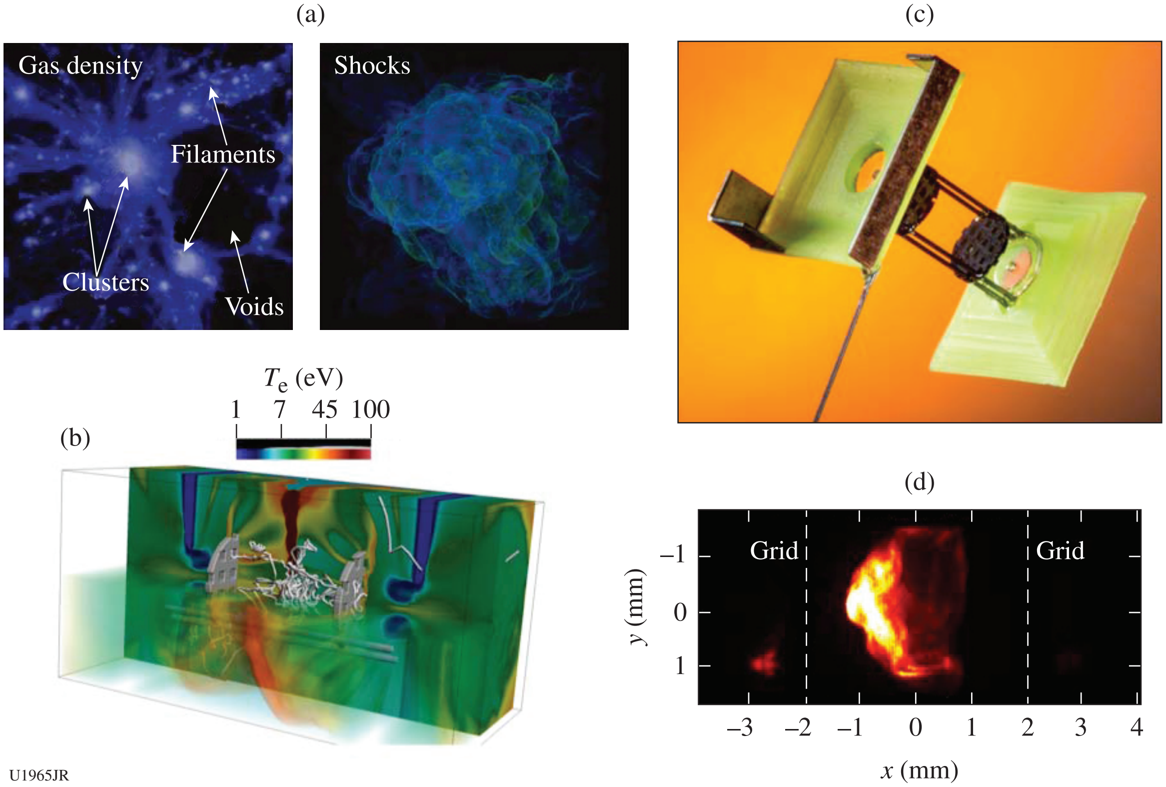

Figure 144.63
(a) It is an observational fact that the universe is magnetized: planets, stars, galaxies, filaments, clusters of galaxies, and even the voids in between filaments and galaxy clusters have magnetic fields. The two simulated images (courtesy of F. Miniati, ETH Zurich)[4] display the large-scale structure characteristics of galaxy clusters, where nonlinear dynamo field amplification is believed to operate. (b) Three-dimensional radiation magnetohydrodynamic simulation of the experimental platform, performed with the multiphysics code *FLASH*. A large simulation campaign on Argonne National Laboratory's *Mira* BG/Q supercomputer leveraged the previous experimental data to design a platform capable of probing the nonlinear dynamo regime. The figure displays a 3-D rendering of the simulated electron temperature (in eV) after the jets collide (see text). Its large values are important to minimize ohmic dissipation. The white tangled lines are sample magnetic-field lines in the turbulent region. (c) A snapshot of the experimental target, consisting of two CH foils and a pair of meshes, held together by four boron rods. The foils and meshes were carefully designed and machined to optimize the conditions in the interaction region for turbulent field amplification. The shields and flaps protect the interaction region, the imploding D^3He capsule, and the diagnostics from the direct view of the laser spots. (d) X-ray image of the interaction region after the collision. The flow exhibits strong turbulence and is considerably hot. The wealth of experimental diagnostics has enabled us to characterize the magnetized plasma and possibly witness, for the first time, nonlinear turbulent dynamo.

to significantly increase the magnetic field, starting from tiny seed fields that exist in the plasma. Building on preparatory campaigns on smaller laser facilities and aided by the numerical modeling effort on one of the nation's leadership supercomputers [Fig. 144.63(b)], the experimental platform we designed is uniquely fitted to bring the generated turbulent plasma into the large magnetic Reynolds numbers range and the nonlinear dynamo regime. The configuration [Fig. 144.63(c)] consists of two diametrically opposed foil targets—8 mm apart—that are backlit with temporally stacked beams (delivering 5 kJ of energy on each side). These beams drive a pair of colliding plasma jets that carry seed magnetic fields generated by the Biermann battery effect. Prior to colliding, the jets propagate through a pair of grids that destabilize the flow and produce turbulence with a driving scale of 300 μm. The turbulent jets meet at the target chamber center (TCC), and the resulting hot, turbulent plasma amplifies the seed magnetic fields with the potential to reach saturation. This process has not yet been achieved in a laboratory setting.

The wealth of diagnostics fielded with the 13 shots we performed enables us to thoroughly characterize the magnetized, turbulent plasma and study the distribution of turbulent energy among the velocity, magnetic field, and density fluctuations, providing a comprehensive experimental characterization of the energy cascade. More specifically, time-resolved x-ray imaging [Fig. 144.63(d)] allows us to probe the density spectrum and the jet propagation speed. The Thomson-scattering (TS) system provided information on the plasma ion/electron temperature, as well as the characteristic bulk flow velocity in the interaction region. In our experiment, TS collection was coupled through a Wolaston prism to separate two orthogonal polarizations and thereby provide a time series of Faraday rotation angles. Combining the latter with proton radiography enables us to quantify the properties and structure of the magnetic field as a function of space and time. The abundance of experimental data we obtained, which is still being analyzed, holds the promise of bringing us a step closer to understanding the holy grail of astrophysical and experimental physics: the nonlinear amplification of magnetic fields by the turbulent dynamo mechanism.

Explorations of Inertial Confinement Fusion, High-Energy-Density Physics, and Laboratory Astrophysics

Principal Investigators: R. D. Petrasso and C. K. Li (MIT)
Co-investigators: F. H. Séguin, J. A. Frenje, and M. Gatu Johnson (MIT); T.C. Sangster, V. Yu. Glebov, and R. Bettii (LLE); and O. L. Landen (LLNL)

MIT work in FY15 included a wide range of experiments applying proton radiography, charged-particle spectrometry, and neutron spectrometry methods developed by MIT and collaborators to the study of high-energy-density physics (HEDP) and inertial confinement fusion (ICF) plasmas. Two MIT Ph.D. theses[5,6] and 17 papers[7–23] (including one by an MIT undergraduate[22]) about NLUF-related research were published in FY14; there were also many invited talks and contributed talks at conferences. Awards for NLUF-related work were won by several students, including two MIT undergraduates: Mr. J. Rojas-Herrera received the *Irving Kaplan Award for Academic Excellence by an Undergraduate* at MIT, and the *Wunsch Foundation Award for Outstanding Research* at MIT; Ms. E. Armstrong won an award for an outstanding poster presentation at the 2015 OMEGA Laser Users Group Workshop.

The two graduate students who received Ph.D.'s have joined NNSA facilities: Los Alamos National Laboratory (Dr. A. Zylstra as a Reines Fellow) and Lawrence Livermore National Laboratory (H. Rinderknecht as a Lawrence Fellow). Three new Ph.D. students (Mr. G. Sutcliffe, Mr. N. Kabadi, and Mr. W. Han) and a new masters degree student (Mr. C. Wink) joined our division and will become active participants in the NLUF program, working alongside continuing graduate students Mr. H. Sio and Mr. Br. Lahmann.

One of the major areas of research this year focused on the stopping of ions in plasmas. Figure 144.64 illustrates one kind of such research: the stopping of ions in classical plasmas.[7] This work utilized charged fusion products from ICF implosions and measurements of their energy losses in passing through the ICF-capsule plasma using charged-particle spectrometers. Another kind of stopping-power research focused on energetic protons passing through moderately coupled, degenerate "warm dense matter."[9] The data demonstrated agreement with stopping models based on an *ad hoc* treatment of free and bound electrons, as well as an average-atom, local-density approximation. In this case the stopping medium was an isochorically heated, solid-density Be plasma, and the source of monoenergetic, 14.7-MeV D^{3}He protons was an "exploding-pusher" ICF implosion functioning as a proton backlighter.

Other areas of research represented in publications this year include kinetic effects in plasmas[8,11,13,15,17] and magnetic reconnection.[10,16,19] Research performed and to be submitted shortly for publication includes the study of nuclear reactions relevant to stellar and big-bang nucleosynthesis; the study of

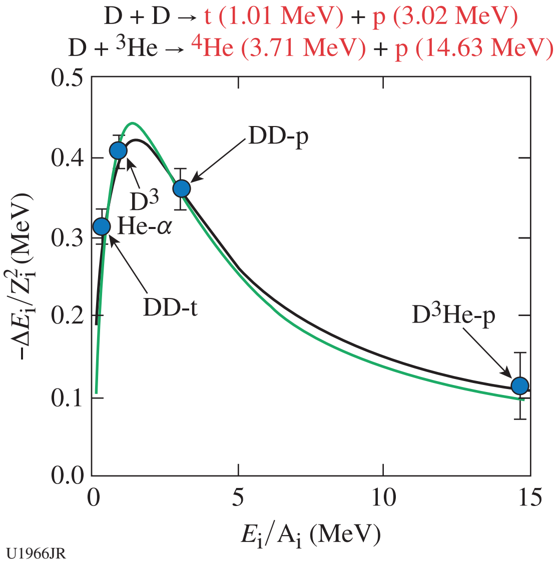

Figure 144.64
Sample data from a study of ion stopping in plasmas[6] that is important for its relevance to ICF ignition experiments. The experiments were performed on OMEGA by measuring the energy losses (shown on the vertical axis) of four types of charged fusion products (see equations) with different initial energies (shown on the horizontal axis) as they passed through the plasma in ICF implosions. Data points are in blue, and the black and green lines show best fits using two stopping theories. Other measurements showed how ion stopping at energies around the Bragg peak (or peak ion stopping) depends strongly on electron temperature (T_e) and number density (n_e). The data in this plot correspond to $T_e \approx 0.6$ keV and $n_e \approx 10^{23}$.

astrophysical jets using scaled, laser-driven plasma jets in the laboratory; and studies of the effects of externally applied magnetic fields on the propagation of plasma jets.

An important ongoing task of the MIT Division has been the organization of the OMEGA Laser Users Group (OLUG), which by this year has grown to include 428 scientists, students, academics, and researchers from 55 universities, 35 centers and national laboratories, and 21 countries on four continents who have an interest in the experimental programs on the OMEGA and OMEGA EP Laser Systems. The Seventh Annual OLUG Workshop was held this year at LLE on 22–24 April (see Fig. 144.35 of **The Seventh Omega Laser Facility Users Group Workshop**, p. 202), and included invited science talks by world experts and 70 contributed posters including 7 by undergraduate and 44 by graduate students and postdocs. It also included talks and meetings about the Omega Laser Facility, which culminated in the formation of a list of **Findings and Recommendations** (p. 204) for improvements in hardware and procedures for OMEGA and OMEGA EP. The next annual Workshop is scheduled for 27–29 April 2016.

Generation of Collisionless Shocks in Laser-Produced Plasmas

Principal Investigator: A. Spitkovsky (Princeton University)

The MagShock-EP Campaign investigates the interaction of a plasma flow with an ambient magnetic field, in an effort to create the kind of magnetized collisionless shocks that commonly occur in astrophysical plasma flows. In such systems the magnetic fields may be advected and compressed by the plasma, producing regions of high magnetic-energy density where shocks can occur. In this experiment the ambient field is created using the MIFEDS (magneto-inertial fusion electrical discharge system) device in a Helmholtz-like geometry, producing a 6- to 8-T field in a background plasma. A strong plasma flow is generated by laser ablation of a separate target, oriented so the flow expands across (perpendicular to) the magnetic-field lines [Fig. 144.65(a)]. In this way the background field is compressed, and the resulting structure is probed with the 4ω suite of diagnostics and with short-pulse [target normal sheath acceleration (TNSA)]–generated protons. An example of an image obtained from each of these diagnostics is shown in Figs. 144.65(b) and 144.65(c). The sharp feature in the 4ω shadowgraphy is consistent with a shock front; analysis is underway to compare features observed in proton radiographs with synthetic proton radiographs generated from simulations.

Hot-Electron Scaling in Long-Pulse Laser–Plasma Interactions Relevant to Shock Ignition

Principal Investigator: M. S. Wei (General Atomics)
Co-investigators: C. M. Krauland and F. N. Beg (University of California, San Diego); and W. Theobald, R. Betti, D. Haberberger, and E. M. Campbell (LLE)
Graduate Students: S. Zhan and J. Peebles (University of California, San Diego)

Energy conversion from high-power lasers to energetic hot electrons is a fundamental phenomenon in laser–plasma interactions. At laser intensities above a few times 10^{14} W/cm^2, nonlinear laser–plasma instabilities such as the stimulated Raman scattering (SRS) and the two-plasmon decay (TPD) can strongly grow and lead to the generation of hot electrons with a broad energy distribution at typical slope temperatures of tens to hundreds of kilo-electron volts (keV). The fraction of laser energy transferred to hot electrons, their energy distribution, transport, and energy coupling to the targets are strongly affected by the laser intensity, wavelength, and the plasma condition. The objective of this General Atomic NLUF project in collaboration with the University of California, San Diego and LLE is to systematically study the scaling of hot-electron

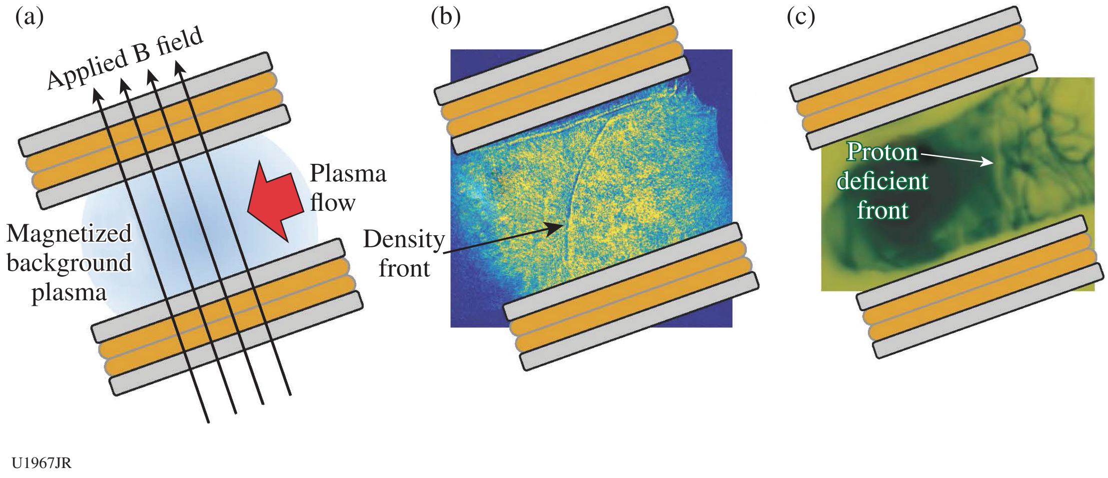

Figure 144.65
(a) Geometry of the experiment: a fast plasma flow is driven across the B-field, which is generated by the MIFEDS coils; (b) the spherically expanding plasma front is evident in the 4ω shadowgraphy image; (c) in proton radiography, the leading edge of the expanding plasma is indicated by a deficiency of protons, consistent with the compressed magnetic field in this area.

generation with parameters, including target ablator material, at high laser intensities (>10^{16} W/cm^2) with a long-scale-length hot plasma, pertinent to shock-ignition (SI) target physics. SI separates compression and ignition with a shaped laser pulse that has a spike pulse with intensities ~5 to 10 × 10^{15} W/cm^2 at the end of a quasi-isobaric fuel-assembly phase to launch a high-pressure converging shock to ignite the compressed fuel. Moderate-energy electrons (50 to 100 keV) can be stopped in the compressed high-density outer shell region and can potentially augment the ignitor shock strength and enhance the target performance, thereby benefitting the SI scheme. Our first-year experiment in FY15 conducted on the OMEGA EP laser in a planar geometry was designed to investigate the feasibility of a beneficial hot-electron source using a high-energy IR laser pulse (1ω, 1.054-μm wavelength) compared to the commonly used short-wavelength UV pulse (3ω, 0.351 μm), both at intensities greater than 10^{16} W/cm^2. In addition, a low-Z lithium ablator was also used for the first time to compare with the usual CH ablator for hot-electron production.

The experiment was performed using the multiple kilojoule-scale OMEGA EP lasers that utilized two UV beams (Beams 3 and 4) for long-scale-length, hot (>1-keV) plasma creation followed by one high-intensity main interaction beam at chosen time delays. The main interaction beam was either the 1-ns UV Beam 1 or the 100-ps IR backlighter beam. The plasma-creation beams smoothed by SG8 (eighth-order super-Gaussian spatial profile) distributed phase plates (DPP's) with a 4-ns square pulse were focused with a 750-μm spot onto the target ablator with a total energy of 6.25 kJ. The UV Beam 1 was tightly focused (~100-μm vacuum focal spot without a DPP) with maximum energy of ~1.3 kJ to achieve a high intensity at 2 × 10^{16} W/cm^2, and the focal plane was located ~215 μm in front of the target, corresponding to the position of $n_c/4$ density (for 0.35-μm light) at roughly 1.5 to 2 ns into the plasma-creation beams predicted by the 1-D radiation–hydrodynamic modeling. Given the same motivation, the IR backlighter beam was defocused to a 100-μm spot diameter roughly 800 μm in front of the target. The two different laser configurations can be seen in Fig. 144.66 with the lines of sights to the various diagnostics employed. For this study we used multilayered planar-foil targets that consisted of an ablator layer (either 25 μm of CH or 50 μm of lithium) followed by a 20-μm Cu tracer layer to measure hot-electron–induced Cu K-shell florescence emission and a 50-μm Al back layer to stop <200-keV electrons and prevent reflexing. The lithium ablator targets also had a 2-μm plastic overcoating layer to protect Li from oxidation when exposed in air during the necessary target mounting and handling process. The plasma density profile and laser–plasma interaction phenomena were measured via 10-ps, 4ω optical probing with an angular filter refractometer (AFR). Hot electrons were characterized by measuring their induced Cu fluorescence emission and high-energy bremsstrahlung radiation.

Figure 144.67 shows the measured 2-D Cu K_α images from shots with the CH ablator target for each of the laser configurations, including a background shot with only the plasma-creation beams. While UV Beam 1 produced slightly additional hot electrons relative to the plasma-creation beams, a significant (factor-of-4) enhancement of a hot-electron–produced Cu K_α signal was observed when the IR beam was used as the main interaction beam at an intensity ~2×10^{17} W/cm^2 with a maximum energy of 2.5 kJ. Hot electrons produced by the IR beam appear to be well contained in a 465-μm full width at half maximum (FWHM) spot inside the solid target. This phenomenon may be elucidated by the measured AFR image shown in Fig. 144.68. While being able to determine the plasma density profile from the ARF contour map, propagation of the high-intensity IR beam in the long-scale-length hot plasma was also observed with strong interactions occurring near the $n_c/4$ density region. The laser beam was found to break out into many filaments that further propagated without merging over a distance of 800 μm from the $n_c/4$ to n_c. This was not observed when the IR beam intensity was dropped to 6×10^{16} W/cm^2 at the same plasma condition. Bremsstrahlung emission suggests an electron population with $T_{\text{hot}} \sim 70$ keV produced by the high-intensity IR beam with a laser-to-electron energy conversion efficiency of a few percent, while the plasma-

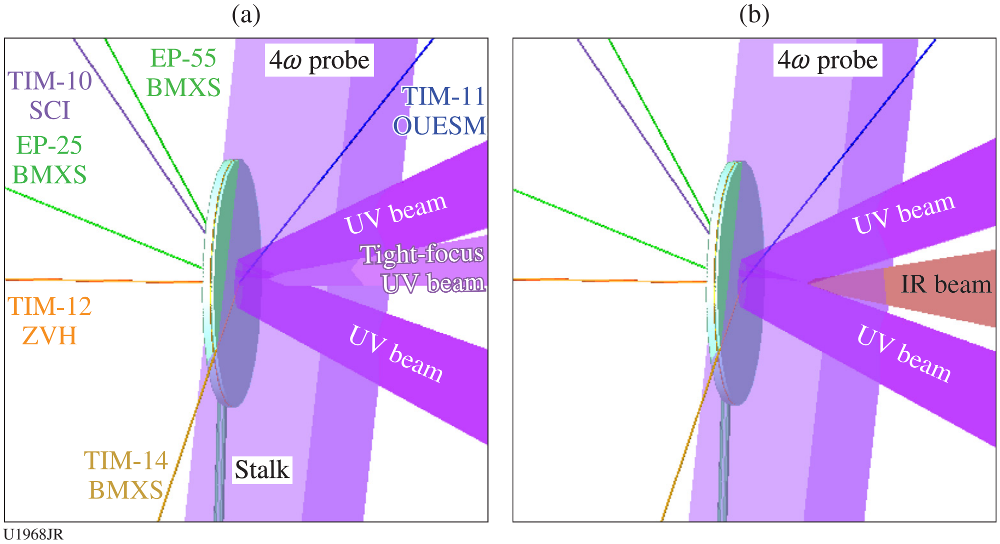

Figure 144.66
Experimental layout of laser beams and diagnostics with (a) the 1-ns UV Beam 1 and (b) the 100-ps IR backlighter beam as the high-intensity main interaction beam, respectively.

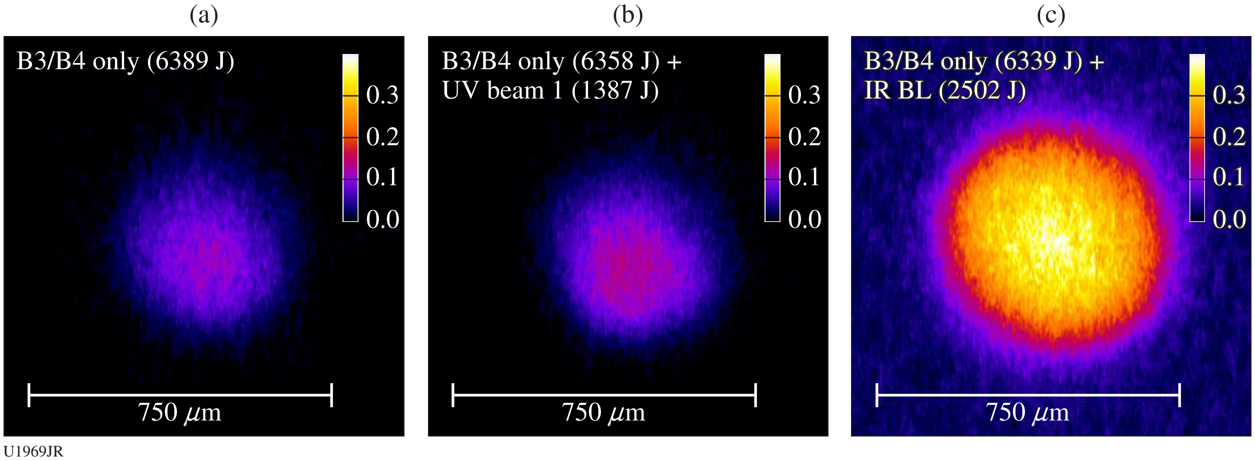

Figure 144.67
The measured 2-D Cu K_α images with (a) only the two plasma-creation beams (UV Beams 3 and 4), (b) the addition of UV Beam 1 as the main interaction beam, and (c) the IR backlighter (BL) beam as the high-intensity main interaction beam. The main interaction beam was injected at 1.5 ns into the plasma-creation beams.

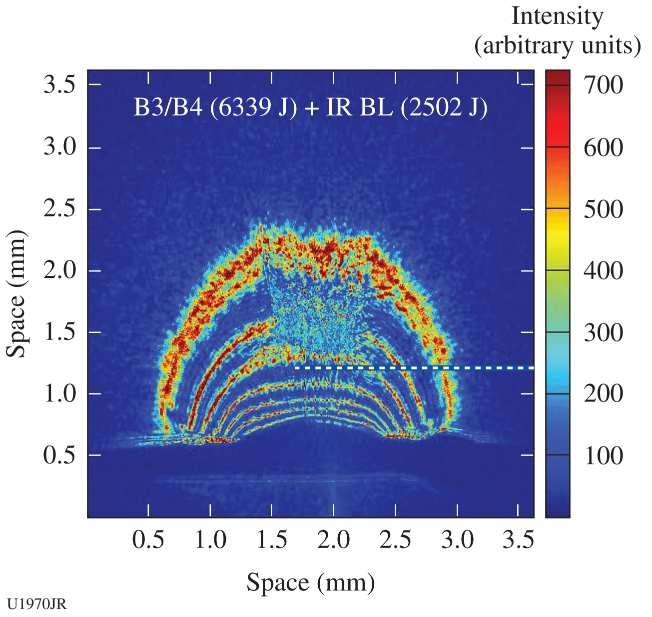

Figure 144.68
The 4ω probe AFR data shows the high-intensity IR beam strongly interacting with the long-scale-length plasma near the $n_c/4$ region and the laser beams breaking out into many filaments that propagate from roughly $n_c/4$ to n_c without merging. The dashed white line denotes ~800 μm from the target surface, where the IR beam was defocused with a vacuum spot size of 100 μm.

creation beams generated a smaller population of low-energy (~20-keV) hot electrons with energy conversion efficiency of ~0.4%, consistent with a previous study that used the UV beams at similar plasma and laser-intensity conditions. This first-time test result using the 100-ps-long IR beam at SI-relevant conditions is encouraging and will be further explored in FY16 in the spherical geometry on OMEGA. Additionally, lithium ablator targets produced weaker x-ray signals, indicating few numbers of hot electrons were produced compared to the CH ablator targets at the same laser condition. Detailed data analysis and particle-in-cell modeling to understand the underlying physics are underway.

High-Energy Electron-Beam Acceleration from Underdense Plasmas Using OMEGA EP

Principal Investigators: L. Willingale, T. Batson, A. Raymond, and K. Krushelnick (University of Michigan); P. M. Nilson, D. H. Froula, D. Haberberger, A. Davies, and W. Theobald (LLE); J. G. Williams and H. Chen (LLNL); and A. V. Arefiev (University of Texas, Austin)

In FY15, studies of laser channeling in underdense plasmas outlined in Ref. 24 were continued with the particular addition of the 4ω optical probe diagnostic. A 1200-J, 2.5-ns UV laser pulse heating a CH-foil target formed an underdense plasma plume. A 0.7-ps, 400-J IR pulse was then focused through the expanding plasma plume. Because of the ponderomotive force acting to expel the electrons from the focal volume, a laser channel was formed. The angular filter refractometry (AFR) arm of the 4ω probe was used to characterize the plasma-plume density and to observe the channel formation. An example AFR image is shown in Fig. 144.69. The peak plasma density through which the channel was formed was determined to be 1×10^{20} cm^{-3}, or 0.1 n_c for the 1.053-μm OMEGA EP laser. Simultaneously, a proton probe diagnostic was run using the second high-energy short-pulse beam. Focusing 750-J, 10-ps laser light onto a Cu foil produced a beam of protons that transversely probed the main interaction. A radiochromic film (RCF) stack detected the deflected proton beam to form an image corresponding to the electromagnetic fields of the channel.

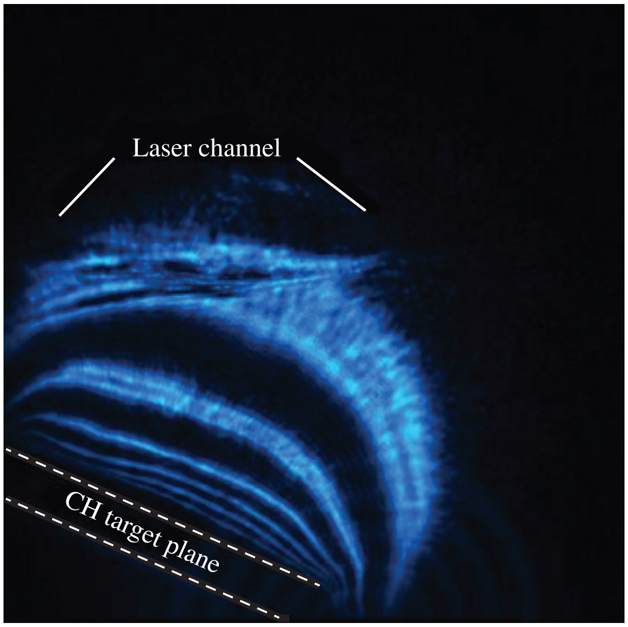

Figure 144.69
An angular filter refratometry image of the channel formation through the expanding plasma plume.

While the channel was cavitated, electrons were injected from the channel wall and subjected to the laser fields, enabling energy gain via a direct laser acceleration (DLA) mechanism.[24] The energy of the electrons exiting the channel was then measured using a magnetic spectrometer. En route to the spectrometer, the electrons passed through an RCF stack with a 1-cm hole cut through the center. An example RCF is shown in Fig. 144.70, where the electron beam consistently emerged from the target at an angle of 14° from the original laser beam

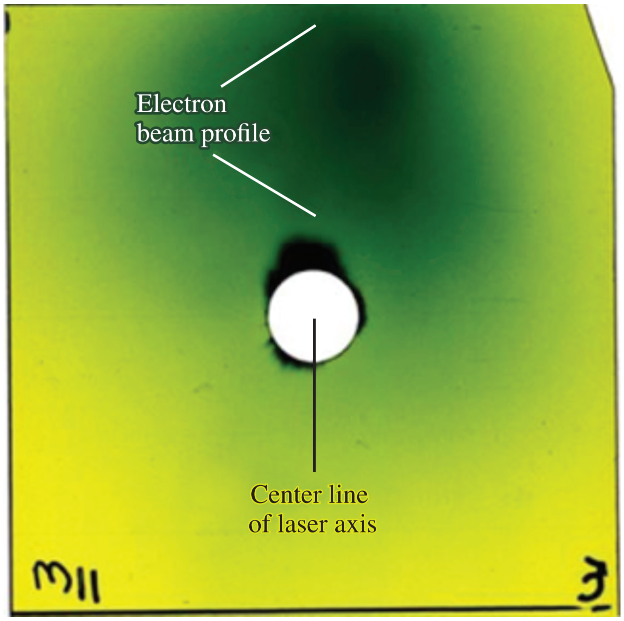

Figure 144.70
The electron-beam profile and pointing was recorded on radiochromic film (RCF). The peak signal occurred at 14° from the original laser beam axis.

axis. This effect has also been seen in particle-in-cell simulations and is caused by refraction of the laser by the density gradient of the plasma. As a result, the most dense, presumably highest-energy section of the electron beam was not sampled by the electron spectrometer. A high-energy tail of 300 MeV was recorded, however, from the edge of the beam. This is a promising result since the beam-centered electrons likely have greater energy.

Future shots on OMEGA EP will involve creating a channel through a plasma without a significant radial-density gradient. This should minimize refraction of the laser pulse so that the DLA electron beam can be directed along the original laser axis and, therefore, centered on the spectrometer. A scan of different target densities will then be performed to optimize the electron acceleration.

FY15 Laboratory Basic Science (LBS) Studies

In FY15, LLE issued a solicitation for LBS proposals to be conducted in FY16. A total of 23 proposals were submitted. An independent review committee reviewed and ranked the proposals; on the basis of these scores, 14 proposals were allocated 20 shot days at the Omega Laser Facility in FY16. Table 144.XV lists the approved FY16 LBS proposals.

Fourteen approved LBS projects were allotted Omega Facility shot time and conducted a total of 235 target shots at the facility in FY15 (see Table 144.XVI). The FY15 LBS experiments are summarized in this section.

Extended X-Ray Absorption Fine Structure Measurements of Iron-Melting Temperature at Earth's Core Conditions

Principal Investigators: M. Beckwith and Y. Ping (LLNL)
Co-investigators: R. Kraus, F. Coppari, J. Eggert, G. Collins, and T. Duffy (LLNL)

The melting temperature of iron at high pressure is a key for developing reliable thermal models of the deep Earth. This two-day OMEGA campaign used the previously developed EXAFS (extended x-ray absorption fine structure) platform to obtain high-quality EXAFS data of compressed Fe up to 200 GPa along the Hugoniot. On both days we used a dual drive with 37 beams on the backlighter, which worked well and will allow for more flexibility in pulse shaping for future campaigns. The 14 shots in the first campaign were complicated by target issues and unexpected differences in nominally identical spectrometers. The 13 shots on the second day were successful, with good EXAFS and VISAR (velocity interferometer system for any reflector) data obtained on all shots. Figure 144.71 shows a sample image from the multicrystal XRS (x-ray scattering code) array used to collect the Fe EXAFS data; Fig. 144.72 shows a sample of raw VISAR data. The EXAFS data, together with VISAR data obtained under the same conditions, will provide high-accuracy temperature measurements with error bars substantially smaller than previous data.

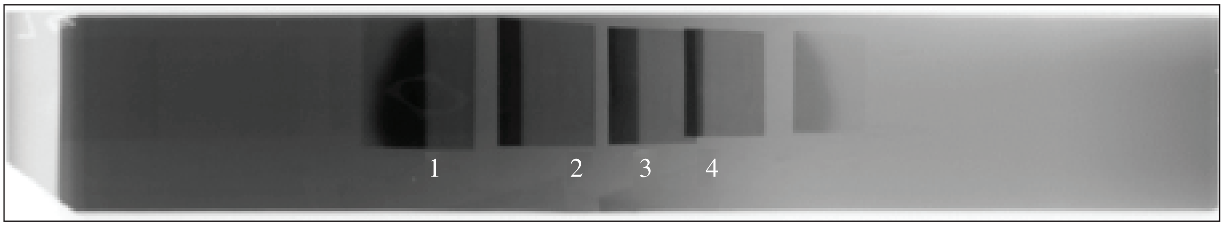

Figure 144.71
Raw image from the multicrystal XRS array. The Fe K edge is clearly seen in four of the five channels.

Table 144.XV: LBS proposals approved for FY16.

Principal Investigator	Title	Institution	Facility required	OMEGA shot days allocated	OMEGA EP shot days allocated	Joint shot days allocated
R. Betti	Ultra-Strong Spherical Shocks for Nuclear and Materials Studies	LLE	OMEGA	1	0	–
J. H. Eggert	Development of Compressed Ultrafast Photography (CUP) Diagnostic for Dynamic Laser Compression Experiments	LLNL	OMEGA EP	0	1	–
C. J. Forrest	Studies of (n,2n) Reactions of Light Nuclei at E_n = 14 MeV Using High-Energy-Density Laser Plasmas (HEDLP)	LLE	OMEGA	1	0	–
S. Ivancic	Integrated Channeling of High-Intensity Laser Beams in Implosions	LLE	Joint	1	1	1
A. E. Lazicki	Structural Studies of Electride Phases of High-Density Matter: Structures of Mg to Above 10 Mbars	LLNL	OMEGA	2	0	–
D. D. Meyerhofer	High-Field–Assisted X-Ray Source	LLE	Joint	1	1	1
J. D. Moody	Characterization of Laser-Driven Magnetic Fields Using Proton Deflectometry	LLNL	OMEGA EP	0	2	–
P. M. Nilson	Study of Particle Energization During Magnetic Reconnection in High-Energy-Density Plasmas	LLE	OMEGA EP	0	2	–
A. Pak	Ion Acceleration from Laser-Driven Electrostatic Shock Waves	LLNL	OMEGA EP	0	1	–
H.-S. Park	Weibel Instabilities and Astrophysical Collisionless Shocks from Laser-Produced Plasmas	LLNL	OMEGA	2	0	–
Y. Ping	Pressure Ionization in Ramp-Compressed Materials	LLNL	OMEGA	1	0	–
C. Stoeckl	Spectroscopy of Neutrons Generated Through Nuclear Reactions with Light Ions in Short-Pulse Laser Experiments	LLE	OMEGA EP	0	1	–
W. Theobald	Proton Transport and Coupling into Shock-Compressed CH Targets for Proton Fast Ignition	LLE	OMEGA EP	0	1	–
C. E. Wehrenberg	Kinetics, Mechanism, and Shear Strain of the bcc-to-hcp Transition in Shock-Compressed Iron from Laue Diffraction	LLNL	OMEGA	1	0	–

Table 144.XVI: Approved FY15 LBS proposals.

Principal Investigator	Institution	Title
M. Beckwith	LLNL	Extended X-ray Absorption Fine Structure Study of Iron Melting Temperature at Earth's Core Conditions
R. Betti	LLE	Ultrastrong Spherical Shocks for High-Energy-Density Physics Studies
H. Chen	LLNL	Demonstration of a Relativistic Electron–Positron Pair Plasma
J. R. Davies	LLE	Laser-Driven Adiabatic Compression of Magnetized Plasmas
G. Fiksel	LLE	Detailed Study of Magnetic Fields During Magnetic Reconnection in a High-Energy-Density Plasma
C. J. Forrest	LLE	Studies of the Deuteron Breakup Reaction at E_n = 14 MeV Using High-Energy-Density Laser Plasmas (HEDLP)
D. E. Fratanduono	LLNL	Exploring Earth's Lower Mantle
D. Martinez	LLNL	Eagle Pillar Formation on OMEGA EP
A. Pak	LLNL	Phase Separation of Hydrocarbons at High Pressure
H.-S. Park	LLNL	Weibel Instabilities and Astrophysical Collisionless Shocks from Laser-Produced Plasmas
E. Smith	LLNL	X-Ray Diffraction Study to Outpressure–Temperature Phase Space in a Key Planetary Mineral: MgO
C. Stoeckl	LLE	Spectroscopy of Neutrons Generated Through Nuclear Reactions with Light Ions in Short-Pulse Laser-Interaction Experiments
W. Theobald	LLE	Integrated Channeling for Fast Ignition
C. Wehrenberg	LLNL	Flow Stress and Deformation Mechanisms for Plasticity in Shock-Compressed Vanadium

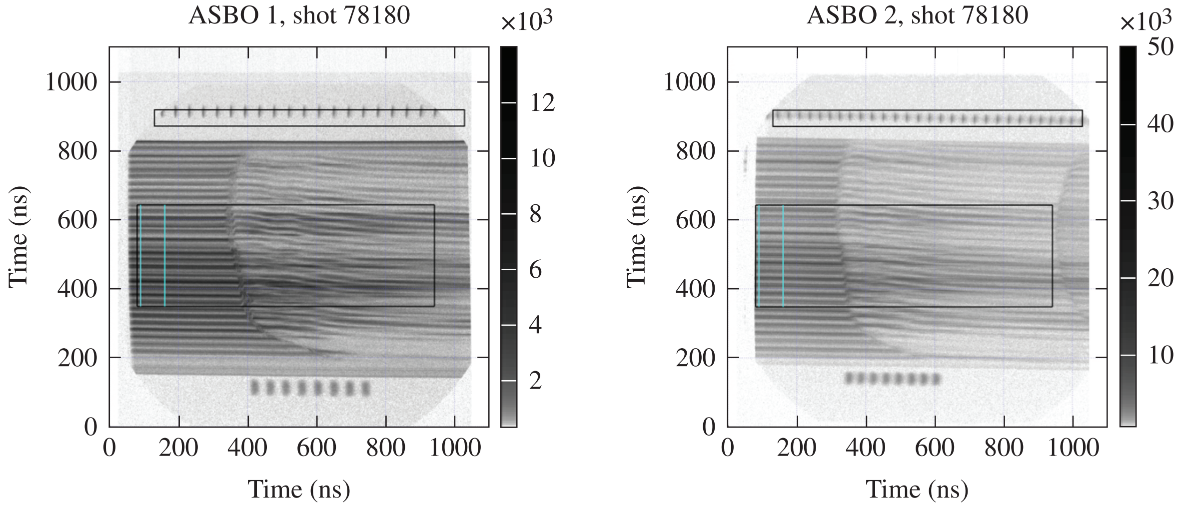

Figure 144.72
Raw VISAR data from (a) ASBO 1 and (b) ASBO 2. ASBO: active shock breakout.

Ultrastrong Spherical Shocks for High-Energy-Density-Physics Studies

Principal Investigators: R. Betti and W. Theobald (LLE)
Co-investigators: W. Seka and C. Stoeckl (LLE); R. Nora (LLNL); A. Casner (CEA); and X. Ribeyre (University of Bordeaux)

The shock-ignition concept[25] is an alternative to the conventional hot-spot approach of inertial confinement fusion; it involves the generation of an intense shock at the end of the laser pulse by a power spike. A key milestone for shock ignition to be a credible path to ignition is to demonstrate the generation of a seed shock pressure of at least 0.3 Gbar at laser intensities of 5×10^{15} to 1×10^{16} W/cm^2. The spherical strong-shock platform was developed to study the seed pressures at shock-ignition–relevant laser intensities on OMEGA. The experiments demonstrated seed pressures exceeding 0.3 Gbar (Refs. 26 and 27). At such intensities, laser–plasma instabilities play an important role in the coupling of laser energy to the target. The 60 UV beams from the OMEGA laser are focused to high intensity (overlapping beam intensity of up to $\sim 6 \times 10^{15}$ W/cm^2) on the surface of spherical solid targets to launch a shock wave that converges in the center. The shock wave converges in the center of the solid target and heats a small volume (radius $< 10\ \mu$m) to temperatures of several hundred electron volts (eV). The heated plasma is ionized and emits a short burst of x-ray radiation that is detected with x-ray framing cameras and an x-ray streak camera.

The goal of this LBS campaign was to optimize the shock strength and the hot-electron production with various targets for the development of a high-energy-density platform to study gigabar (Gbar) pressures in target samples. The hot electrons are characterized from the measured hard x-ray bremsstrahlung emission with several diagnostics. Various target types were studied including cores made out of plastic (CH), deuterated plastic, and plastic doped with titanium with an atomic concentration of 5%. A few targets with a Ti-doped CH core contained an embedded 20-μm layer of a medium-*Z* material (Si) for hot-electron stopping. A 50-μm-thick outer ablator layer made out of CH or CH$_2$ covered the spheres. For the first time, we measured the neutron yield produced from the convergent shock in solid deuterated-plastic targets. A clean neutron measurement was obtained with the 6×8 neutron time-of-flight (nTOF) diagnostic that is able to discriminate the neutron signal from the strong x-ray emission. Standard neutron diagnostics were severely perturbed by the strong x-ray emission from the target. Figure 144.73 shows the measured nTOF traces for two different laser-smoothing conditions: smoothing by spectral dispersion (SSD) on (blue) and SSD off (red). Each trace is the average from two shots. A neutron yield of $(4.0\pm1.5) \times 10^6$ was produced with SSD off and $(9\pm1.6) \times 10^6$ with SSD on. It is currently unclear why the laser smoothing has an effect on the neutron yield. Hydrodynamic simulations with *LILAC* using a flux limiter of 0.06 resulted in a neutron yield of 7×10^6. We studied the hot-electron generation in the different targets. Figure 144.74(a) shows the measured hot-electron temperatures from two independent diagnostics. The inferred hot-electron temperatures agree within the experimental uncertainties and vary in the range from 60 to 90 keV. Figure 144.74(b) shows the amount of hot-electron energy deposited in the target for the different target types. The targets with a CH$_2$ ablator layer produced the highest amount of hot electrons. We successfully measured the x-ray flash times for the different target types for SSD on and off. A much brighter x-ray flash was observed with the undoped targets, which made it possible to measure the duration of the x-ray flash with the picosecond time-resolving ultrafast x-ray streak-camera (UFXRSC) diagnostic. An example of such a measurement is displayed in Fig. 144.75(a), showing the corona emission and the short burst created by the shock convergence. Different filter combinations were applied. Figure 144.75(b) presents a temporal lineout of the x-ray flash from the shock, indicating a fast rise within ~10 ps and a slower decay over 100 ps.

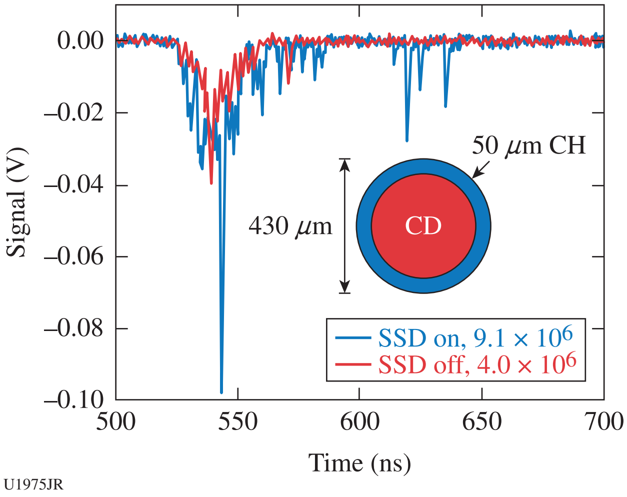

Figure 144.73
Neutron time-of-flight traces for SSD on (blue) and SSD off (red).

The final goal of studying Gbar pressures in a small Ni grain embedded in a solid plastic ball with x-ray spectroscopy is the subject of our FY16 campaign.

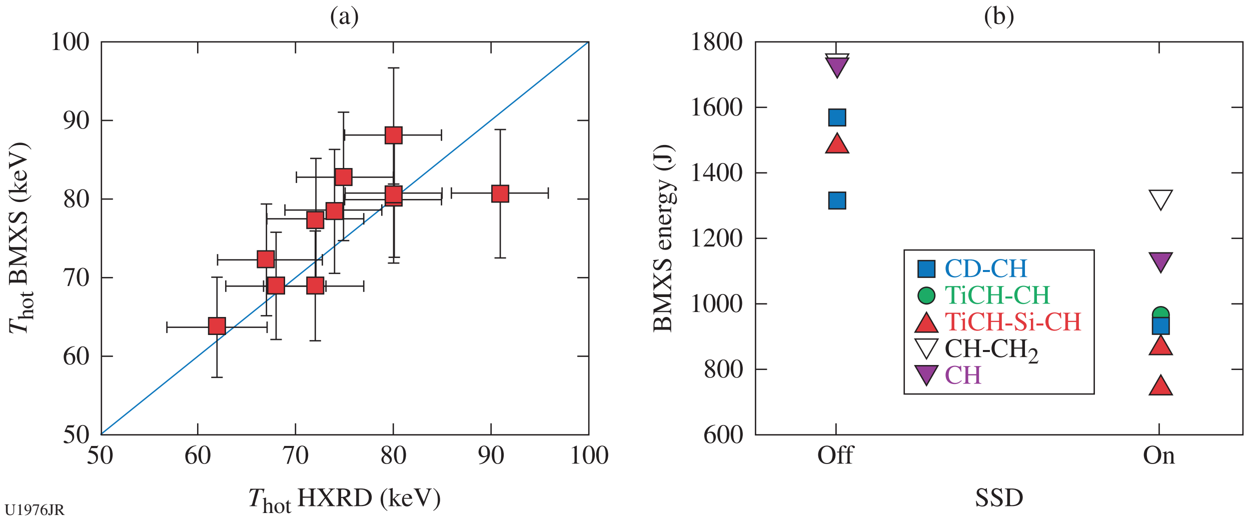

Figure 144.74
(a) Inferred hot-electron temperature from two independent diagnostics; (b) deposited hot-electron energy in the target for different ablator layers and smoothing by spectral dispersion (SSD) on and off. BMXS; bremsstrahlung MeV x-ray spectrometer; HXRD: hard x-ray spectrometer.

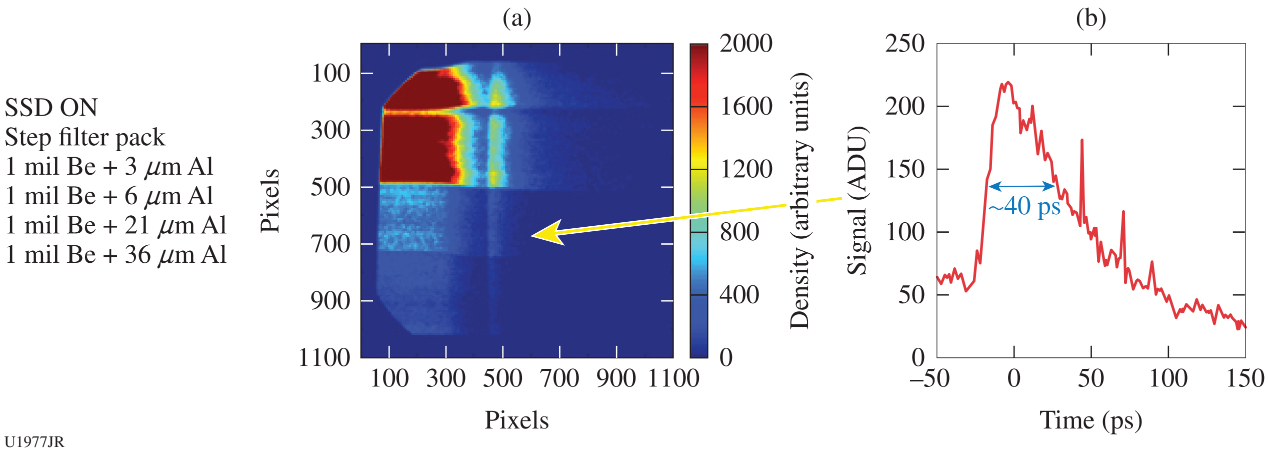

Figure 144.75
(a) X-ray streak-camera measurement of the corona emission and the short burst created by the shock convergence. Different filter combinations were applied. (b) Temporal lineout of the x-ray flash from the shock.

Exploring Pair Plasmas and Their Applications
Principal Investigator: H. Chen (LLNL)

In FY15, an LLNL/LLE team continued this project with two LBS shot days on OMEGA EP. The experiments used the short-pulse beams to produce jets of electron–positron antimatter pairs. The experiments focused on measuring the pair yield and its dependence on the target material. The experiments successfully probed the basic physics processes involved in pair generation, and the data reveal discrepancies between experiments and theory. By alternating beams, a total of 28 shots were performed in two days.

The OMEGA EP short-pulse beams (~1 kJ in 10 ps) irradiated 1-mm-thick targets of Au, Pb, and U. In addition, 1-mm-thick Au targets with a gold nanowire front layer were also shot to study the nanowire's effect on the yield of high-energy photons and pairs. It was found that for the same laser energy, positron yields could be increased dramatically, depending on the target materials and the target surface. This finding is important to future experiments and applications using laser pair jets. Previous experiments used gold targets almost exclusively. These prior experiments showed that quasi-monoenergetic relativistic positron jets are formed during high-intensity irradiation of thick gold targets,[28,29] and that these jets can be strongly collimated[30] using the magneto-inertial fusion electrical discharge system (MIFEDS).[31] The external field produces a 40-fold increase in the peak positron and electron signal.[30] The positron yield was previously found to scale as the square of the laser energy,[32] but the FY15 results revealed another dimension of scaling by varying the target materials. The favorable scaling would enable the laboratory study of relativistic pair plasmas that are important to understanding some of the most exotic and energetic systems in the universe.[33]

Laser-Driven Magnetized Liner Inertial Fusion (MagLIF)

Principal Investigator: J. R. Davies (LLE)

A laser-driven version of Sandia's magnetized liner inertial fusion (MagLIF) scheme is being developed that is 10× smaller in linear dimensions than the targets used on Sandia's Z machine. Three shot days were requested by Sandia and carried out in FY15: one on the LBS program and two as part of the SNL ICF program.

The first two shot days concentrated on preheating the gas fill. The transmission through 1.84-μm polyimide foils, used for the laser entrance windows, was measured and found to exceed 50%, increasing with laser energy. Backscatter from foils only and from gas-filled targets was similar, lasted about 0.5 ns, and accounted for less than 1% of the total laser energy, indicating that there was no backscatter from the gas. Figure 144.76 shows the time dependence of the total transmitted and backscattered laser power for a foil, determined from measurements at three angles to the laser axis on two shots, one measuring backscatter and the other transmission. Soft x-ray emission measurements indicate that the minimum-required preheat temperature of 100 eV was achieved, but the limited spectral resolution of Dante and the soft x-ray (SXR) framing camera nose does not allow for an accurate temperature determination. Streaked optical pyrometry showed that targets were fully heated and started to expand after the laser pulse, providing further confirmation of sufficient energy deposition in the gas.

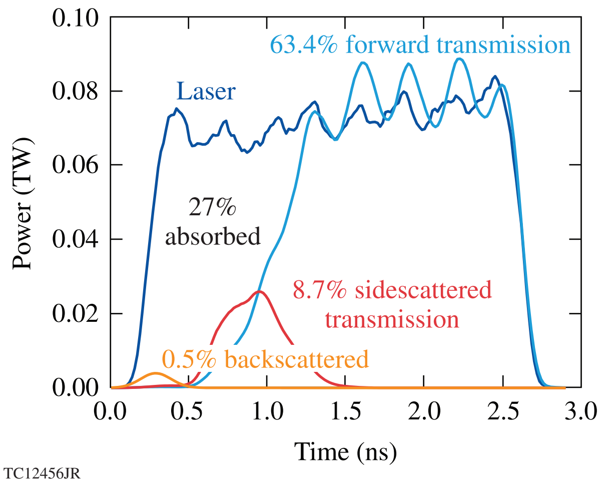

Figure 144.76
Time dependence of the incident laser power, total backscattered power, transmitted power along the original beam path, and sidescattered transmitted power for a foil, determined from measurements at three angles to the laser axis on two shots, one measuring backscatter and the other transmission.

On the second shot day, four implosion shots were also taken with empty, 30-μm-thick, parylene-N cylinders using either ring 3 or 4 beams at the same intensity. The implosion velocities determined from x-ray framing-camera images of self-emission were 124.3±4.0 km/s for rings 3 and 178.1±1.2 km/s for rings 4; the objective is an implosion velocity of ~100 km/s. Figure 144.77 shows sample results from these shots. The lower

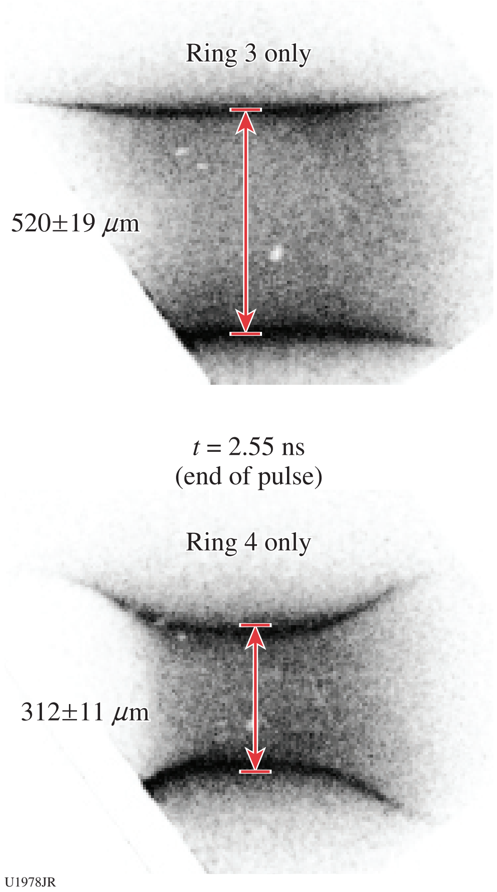

Figure 144.77
X-ray framing-camera images of self-emission from empty 30-μm-thick parylene-N cylinders imploded using either rings 3 or rings 4 at the same intensity with a 2.55-ns square temporal profile.

drive from rings 3 was expected because of their greater angle of incidence.

On the third shot day, 40-μm-thick, parylene-N cylinders filled with 10 atm of D_2 were imploded using rings 3 overlapped in the middle and rings 4 to drive the ends, in order to overcome the reduced drive found for rings 3 in the previous shots. The center was found to be overdriven, so the energy in rings 3 was progressively reduced. The uniformly compressed length was found to be optimized at around 700 μm for 70% to 80% of the full energy in rings 3. This has led to the design of a new irradiation scheme with greater separation between rings, which should give uniform compression over a greater length at full energy.

Detailed Studies of Magnetic Fields During Magnetic Reconnection in a High-Energy-Density Plasma

Principal Investigator: G. Fiksel,* P. M. Nilson, S. X. Hu, D. H. Froula, and D. Haberberger (LLE); and W. Fox and A. Bhattacharjee (Princeton University)
*currently at the University of Wisconsin–Madison

During the FY13–FY14 LBS campaigns, we successfully demonstrated the reconnection of an external magnetic field by counter-streaming high-energy-density plasmas.[34] The experimental results and numerical simulations show the formation and collision of magnetic ribbons, the pileup of the magnetic flux, and the reconnection of the magnetic field. The reconnection is fast, with a transient reconnection rate comparable to the Alfvén reconnection rate.

The main thrust of the LBS FY15 campaign was to detect and characterize particle energization during reconnection. To date, the presence of energetic electrons, detected via x-ray imaging, resulted from the electrons striking a high-Z mesh placed to intercept the electron flow [Fig. 144.78(a)]. The flow of the energetic electrons was very directional and coincided with the direction of the electric field in the reconnection layer. The width of the electron beam was about 150 μm, in agreement with simulations. The time duration of the electron burst was about 100 μs, also in agreement with simulations.

The main goal of next year's campaigns will be more-detailed characterization of the electron energization, including measurements of their energy spectra.

Measuring Neutron-Induced d-Breakup Reactions Using High-Yield DT Implosions on OMEGA

Principal Investigator: C. J. Forrest (LLE)

Theoretical calculations suggest that if the strong force includes three-nucleon force (3N) contributions, an enhancement in the total d(n,2n)p differential cross sections for the neutron–deuteron scattering will be present. The majority of the available d(n,2n)p cross-section values at a neutron energy of 14.1 MeV are inferred from the proton spectrum and are con-

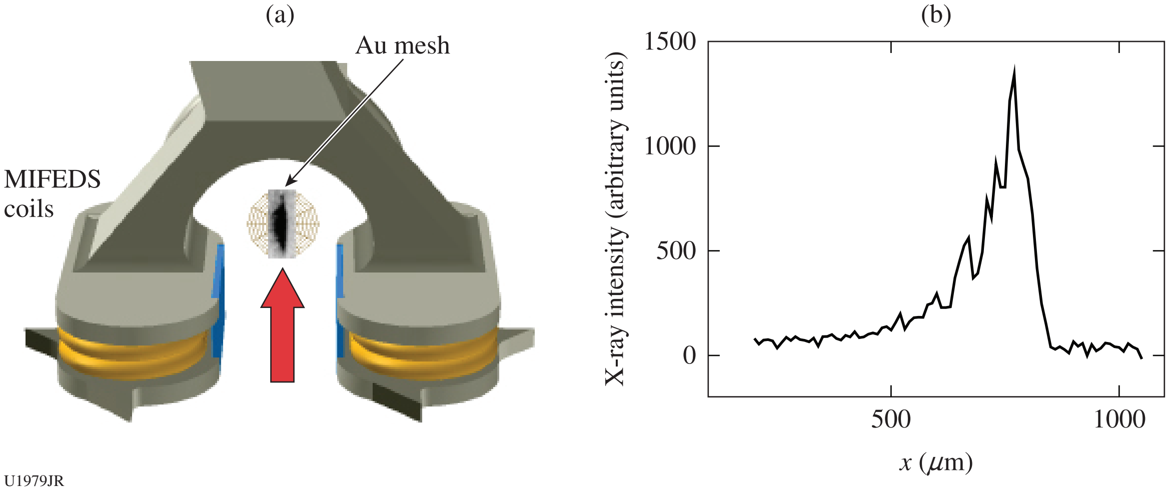

Figure 144.78
(a) A schematic of the experiment showing the MIFEDS coils and an Au mesh intercepting energetic electrons. The direction of the electron flow toward the mesh is indicated by an arrow. The mesh was placed 1 cm from the coil. When the electrons strike the mesh, they generate x rays that are imaged by an x-ray framing camera. One of the x-ray images is overimposed on the mesh to visualize the directionality of the electron beam. (b) Spatial profile of the x-ray footprint shown in (a).

siderably larger than the predictions of rigorous 3N calculations based on realistic nucleon–nucleon (NN) interactions. Initial OMEGA experiments examined the neutron-induced breakup reaction of deuterium. The targets used for this experiment were 1050-μm-diam, 2.5-m-thick SiO_2 shells filled with an equimolar concentration of deuterium–tritium (DT). Neutron yields of up to 6×10^{13} are produced with 30-kJ, 1-ns square laser pulses. High-resolution nTOF spectroscopy is used on OMEGA to study the deuterium breakup reaction signal from a nuclear interaction vessel (NIV) filled with either D_2O or H_2O located close to the implosion target—the source of the primary 14.1-MeV DT fusion neutrons. A highly collimated nTOF detector positioned 13.4 m from the target chamber center is used to record the signal from the interaction of the primary neutrons with the D_2O or H_2O. The vessel is constructed from thin-walled (2-mm) aluminum to minimize neutron scattering. Modeling the experimental setup using a neutron transport code [Monte Carlo N-Particle (MCNP)] indicated that a measurable signal from the breakup process would be present in the nTOF detector. Two DT implosions with similar primary D–T yields are shown in Fig. 144.79, confirming the MCNP signal-level predictions. The spectral differences prior to 500 ns are caused by the deuterium in the NIV. The two spectra are normalized to the D–T fusion yield. The scattered protons were measured using a charged-particle spectrometer. Preliminary analysis shows moderate agreement of the measured cross section compared with experimental data[35] performed on an accelerator and a theoretical calculation (Fig. 144.80).

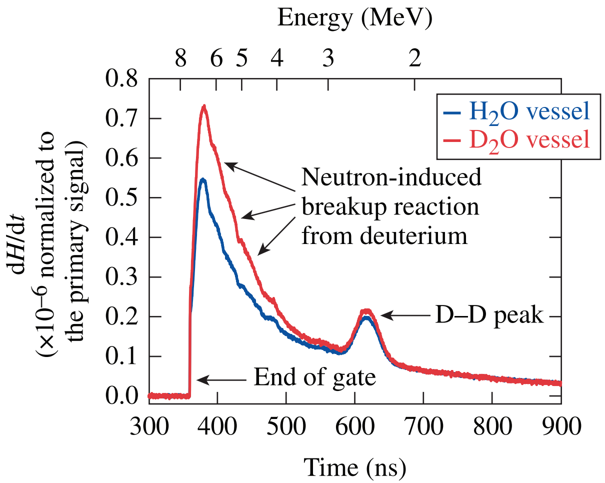

Figure 144.79
Time-of-flight spectra from ambient D–T implosions with an H_2O and D_2O-filled nuclear interaction vessel (NIV). There is a clear indication of an enhanced signal from the neutron-induced breakup reaction prior to the D–D monoenergetic peak at 2.45 MeV. A fast-gating photomultiplier tube is turned on to exclude the D–T monoenergetic peak at 14.1 MeV and is turned off to record the scintillation output just below 6 MeV.

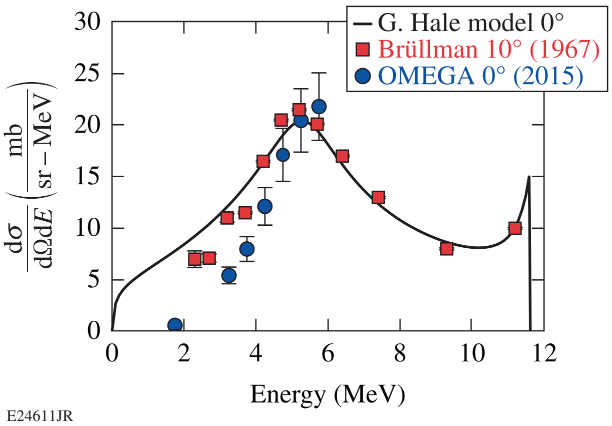

Figure 144.80
Two separate experiments measured the neutron-induced cross sections as a function of energy. A theoretical calculation (black line) shows good agreement with the experimental data measured by Brullman[36] (red squares). The experiment on OMEGA (blue circles) shows partial agreement with the calculated spectrum but begins to deviate toward lower energy.

Exploring the Earth's Lower Mantle

Principal Investigator: D. Fratanduono (LLNL)
Co-investigators: R. G. Kraus, D. K. Spaulding, D. G. Braun, and P. M. Celliers (LLNL)

This campaign was motivated by a recent study[37] of $MgSiO_3$ using decaying shocks, which provided evidence for a liquid–liquid phase transition near 300 GPa. The primary objectives were to measure the adiabatic sound speed (c_s) and the Grüneisen coefficient (Γ) of single-crystal $MgSiO_3$ along the principal Hugoniot from 200 GPa to pressures in excess of 800 GPa, including the proposed two-phase region, to further understand this transition. A secondary goal of these experiments was to accurately measure the principal Hugoniot of $MgSiO_3$ from 200 to 800 GPa by impedance matching with quartz. Using the streaked optical pyrometer, we measured the temperature of $MgSiO_3$, which will provide a fully defined principal Hugoniot. These Hugoniot measurements near the proposed liquid–liquid phase transition will constrain the density discontinuity and overlap with separate gas-gun experiments since no measurements exist from 200 to 400 GPa. Measurements in this pressure range are of interest since recent density functional theory calculations show no presence of a liquid–liquid phase transition.[38] Two separate half-days of experiments were used to study this transition in detail. The primary goals of the campaign were met in the first half-day. These experimental results drew into question, however, the previous findings of

Spaulding *et al.*[37] As a result, during the second half-day of experiments, we repeated the decaying shock experiment of Spaulding *et al.*; however, these experiments were unable to reproduce the previous experimental findings.[37] The analysis is ongoing to better understand the differences between these two experiments and the proposed liquid–liquid phase transition.

Eagle Pillar Formation on OMEGA EP
Principal Investigator: D. Martinez (LLNL)
Co-investigators: C. Huntington, J. Emig, J. Kane, and R. Heeter (LLNL); B. Villette and A. Casner (CEA); and R. Mancini (University of Nevada, Reno)

The LBS Eagle Pillar experiments investigated the early stages of formation of an astrophysical pillar. A copper four-hohlraum array produces a 40-ns x-ray source, which ablates a solid-density CH target with a Cu nugget acting as a plasma source. Pillar formation was investigated using OMEGA EP's 4ω shadowgraphy diagnostic, and the hohlraum drive was measured using CEA's ten-inch–manipulator (TIM)-based mini DMX detector [Fig. 144.81(b)]. The shot day consisted of seven shots varying the standoff distance of the target and looking at various times of the pillar evolution. The blowoff plasma from the hohlraum prevented very late time measurements of the pillar's evolution; however, excellent images were taken of the initial blowoff of the foil (Fig. 144.82). Figure 144.82(a) shows the initial shadowgraph with an initial standoff distance of 2 mm. The distance was incrementally increased to avoid the blowoff plasma from the hohlraum. Figure 144.82(b) shows the plasma blowoff from the ablating Eagle target at 20 ns with

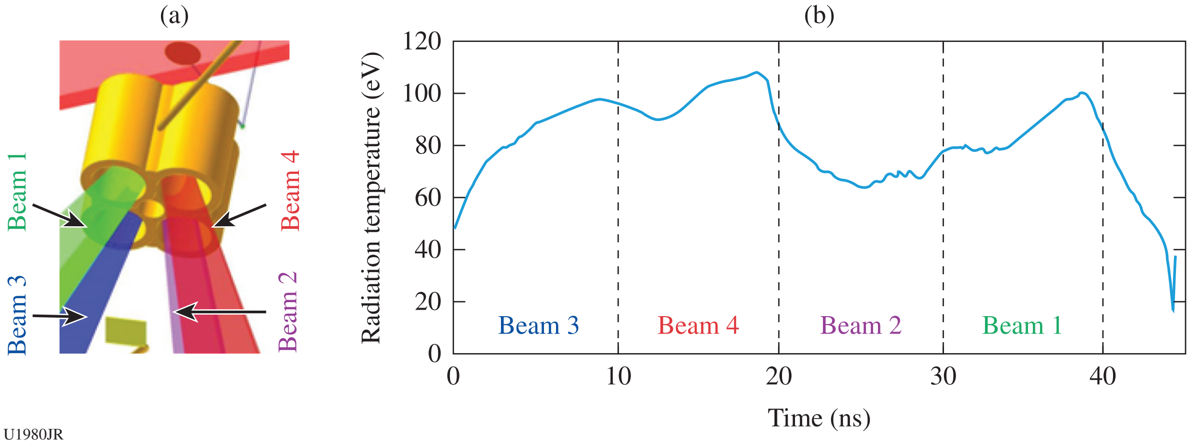

U1980JR

Figure 144.81
(a) Layout of the target showing the hohlraum array with four OMEGA EP UV beams and a photoionization target on the drive side and the Eagle target behind the hohlraum. (b) Results from mini DMX for a single shot with 40-ns drive. (Signal level varies in part because of changes in the beam incident angle.)

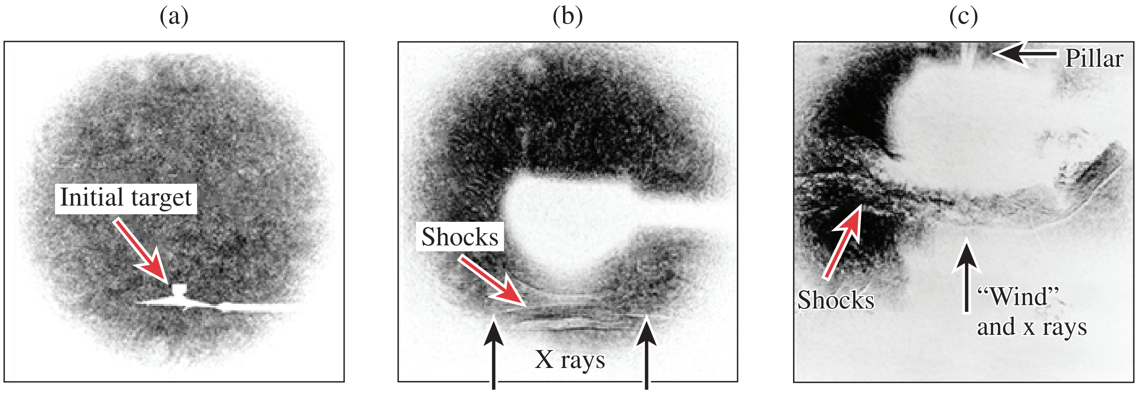

U1981JR

Figure 144.82
(a) Initial target with a 2-mm standoff distance from the hohlraum. (b) Evolution at 20 ns with 3-mm standoff distance. (c) Evolution at 30 ns with 4-mm standoff distance and increased drive. Evidence of initial pillar formation is seen behind the target.

a 3-mm standoff distance. Plasma from the hohlraum is seen interacting with the ablation from the Eagle target, creating shocks between the hohlraum and the target. For the 30-ns image, the standoff distance was increased to 4 mm; however, the increase in distance required an increase in x-ray drive, so two hohlraums were driven simultaneously to double the x-ray flux via a 20-ns rather than a 40-ns drive. At this time the ablation plasma from the Eagle target was being pushed behind the target and collecting in a converging conical flow behind the target, thereby creating the initial pillar formation. As seen at the top of Fig. 144.82(c), this experiment provided the first evidence of pillar formation in the laboratory.

Phase Separation of Hydrocarbons at High Pressure

Principal Investigator: A. Pak (LLNL)
Co-investigators: D. Kraus, T. Ma, T. Doeppner, J. A. Hawreliak, R. W. Falcone, S. Hamel, D. O. Gericke, and D. Chapman (LLNL); and T. R. Boehly (LLE)

We have begun to explore the predicted phase separation of hydrocarbons at densities of ~2 g/cm^3, temperatures of ~0.5 to 1 eV, and pressures of ~1 to 2 Mbar. The relative phase between carbon and hydrogen atoms at such conditions is of interest since they are near to the predicted conditions within the interior of some carbon-rich planets. The degree to which the atoms mix with each other impacts macroscopic quantities such as thermal and electrical conduction, which in turn affect the global planetary properties. In this work, spectrally resolved x-ray scattering was used to probe a hydrocarbon sample to infer the degree of phase separation. The experimental setup is shown in Fig. 144.83(a). Figure 144.83(b) shows an example x-ray scattering spectrum. The compressed matter was probed at a central wave number of 3.8 Å^{-1}. The scattered spectrum is comprised of x rays that scatter both elastically, at the incident x-ray energy, and inelastically, at lower x-ray energies. At the wave number at which the material was probed, density functional theory calculations predict that the amplitude of the elastically scattered x rays will decrease as the amount of mixing increases between the hydrogen and carbon. These calculations indicate that the amount of mixing is sensitive to the temperature of the compressed material. Using the pulse-shaping capabilities of the OMEGA EP laser, the hydrocarbon sample was compressed using two drive conditions. The first drive attempted to reach a 2× compression at relatively low temperatures with a 20-ns pulse shape that, according to calculations, quasi-adiabatically compresses the polystyrene (CH) target to about 2 g/cm^3 and 0.5 eV. To increase the temperature and the amount of mixing, a second drive of 10-ns duration was designed to shock compress the CH target to a higher average temperature of ~1.5 eV at a similar compression. The OMEGA EP laser was also used to create a zinc He$_\alpha$ x-ray line source at ~9 keV, which, after scattering, was spectrally and temporally resolved using the ZSPEC crystal spectrometer onto framing camera #5. As shown in Fig. 144.83(b), in contrast to theoretical predictions, we observe that the amplitude of the elastically scattered x-ray component increases as we attempt to increase the amount of mixing using the 10-ns drive. We are investigating whether geometrical and attenuation effects, in addition to timing jitter between the framing camera and the x-ray source, could explain the unexpected elastic-scattering

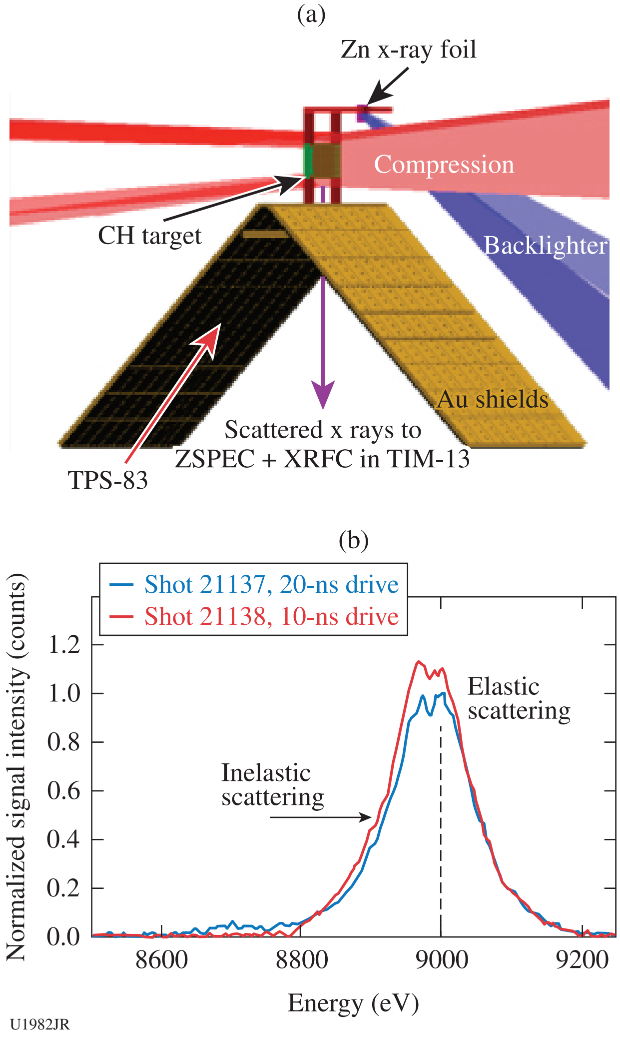

Figure 144.83
(a) Experimental setup. Two drive bundles compress the CH foil, while a probe bundle creates a burst of Zn He$_\alpha$ x rays that scatter through the target. Scattered x rays are collected via ZSPEC onto a framing-camera detector in TIM-3. (b) The spectrally resolved scattered x-ray signal. Signal amplitude has been normalized using the signal from a time-integrated zinc Von Hamos spectrometer. The vertical dashed line indicates the central energy of the incident x rays.

amplitude. Future work will focus on better characterizing the source to quantify the interplay between the elastic and inelastic scattering, better quantifying the drive material conditions for the two drive pulses with VISAR, and potentially taking the measurements at lower scattering wave numbers, where the effect on the amplitude is expected to increase.

Astrophysical Collisionless Shock Experiments with Lasers (ACSEL) on OMEGA EP

Principal Investigator: H.-S. Park (LLNL)
Shot Principal Investigator: C. Huntington (LLNL)

The Astrophysical Collisionless Shock Experiments with Lasers (ACSEL) Campaign has been exploring the physics of interpenetrating plasma flows, which are effectively collisionless, but nonetheless interact strongly with each other, largely via self-generated magnetic fields. The flows are generated by laser ablation of opposing disks with up to 4.5 kJ of laser energy. Previous work,[39,40] along with the references therein, has measured the plasma properties of the resulting flow with Thomson scattering (TS), and proton radiography has revealed strong filamentation structures in the interaction region between the foils.[18] Beginning from this well-characterized platform, FY15 ACSEL experiments modified the system to better understand the dependencies and process of magnetic-field generation.

Previous electromagnetic (EM)-field imaging, using protons generated from D^3He fusion in a capsule implosion, was performed perpendicular to the flows.[18] When the foils were tilted so that the protons probed a vector nearly along the flow direction, however, the small-scale filaments were measured closer to "end on." Shown in Fig. 144.84, these measurements improve our understanding of the scale lengths present in the system, which are difficult to infer from a straight side-on measurement. Additionally, the spacing between the foils was also varied to investigate the effects of plasma density and velocity distribution on the magnetic-field generation. At present, the proton radiography data are awaiting processing, but in conjunction with the high-quality TS data obtained for each shot, this new data will further the understanding of the hydrodynamic dependencies of the Weibel and related filamentation instabilities. Important insights for astrophysically relevant collisionless plasma physics will be gained from these two FY15 OMEGA campaigns.

*Structure of Solid and Superionic Water at Uranus's and Neptune's Core Conditions**

Principal Investigator: J. R. Rygg (LLNL)
Shot Principal Investigators: F. Coppari and M. Millot (LLNL)
*Report on an experiment carried over from the FY14 allocation.

This half-day on OMEGA completed the investigation started in FY14 of the structure and equation of state of solid and superionic warm dense water at Uranus's and Neptune's core conditions, with new laser dynamic compression techniques, optical diagnostics, and x-ray diffraction on OMEGA.

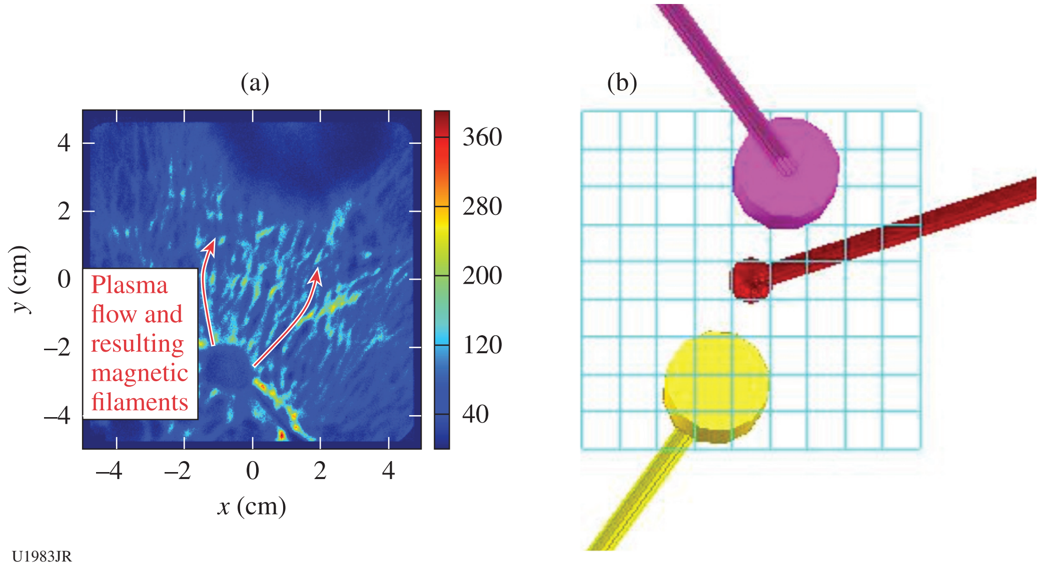

Figure 144.84
(a) A 14.3-MeV proton image showing filamentation along the flow direction (indicated by the red arrows). (b) Orientation of the two laser-irradiated targets (pink and yellow), with the D^3He capsule (red); the approximate field is indicated by the grid.

Water has a complex phase diagram, characterized by different solid structures, including superionic phases. Superionic water ice is characterized by fluid-like diffusing protons within a solid lattice of oxygen ions. Its existence in the deep interiors of icy giant planets would have a dramatic impact on their internal structure and evolution.

Multishock compression of water allowed us to compress initially liquid water into solid and superionic ices up to 5 Mbar while keeping the temperature below 0.5 eV. Streaked optical reflectivity, pyrometry, and interferometric Doppler velocimetry (VISAR) as well as x-ray diffraction provided an unprecedented insight on the equation of state and structure of solid and superionic megabar water ices (Fig. 144.85). This is the first time that diffraction data of such a low-*Z* material have been collected to these extreme conditions.

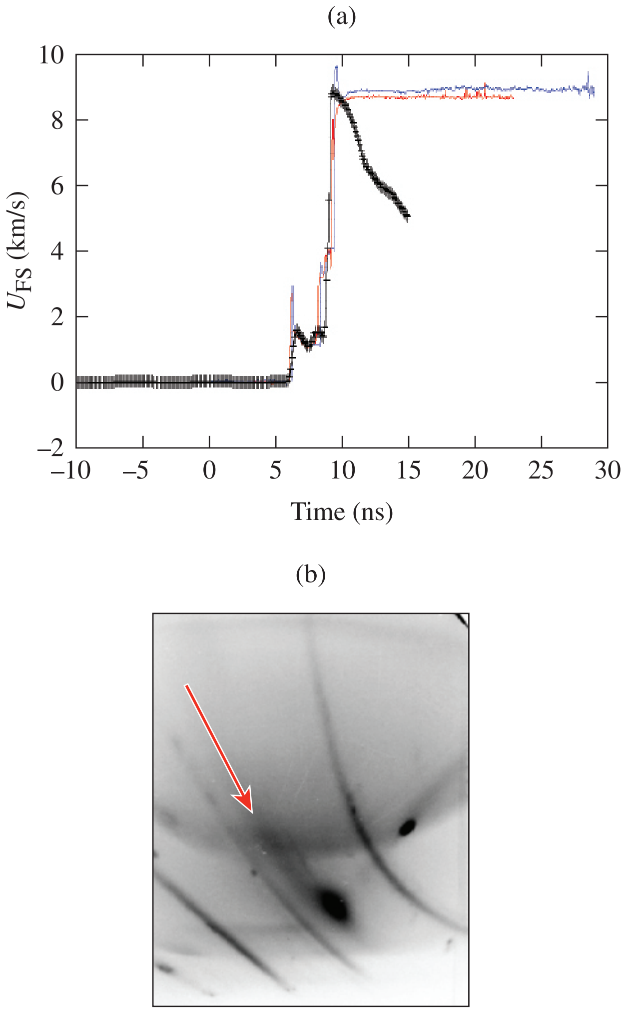

Figure 144.85
(a) VISAR traces (red and blue) together with hydrodynamic simulations (black) matching the experimental records; (b) diffraction data showing lines from the Ta reference, the diamond window, and solid water (red arrow).

Crystal Structure of Shock-Compressed Magnesium Oxide

Principal Investigator: R. Smith (LLNL)

Two half-days on OMEGA and one full day on OMEGA EP were dedicated to experiments to shock compress MgO samples to sample pressures from 200 to 800 GPa and measure the crystal structure of the shock-compressed MgO using recently developed nanosecond x-ray diffraction techniques.[41] The pressure–temperature phase map for MgO is shown in Fig. 144.86 along with the predicted shock-compression path (Hugoniot). A predicted B1–B2 phase transformation is expected to occur between ~350 to 450 GPa. The target design shown in Fig. 144.87

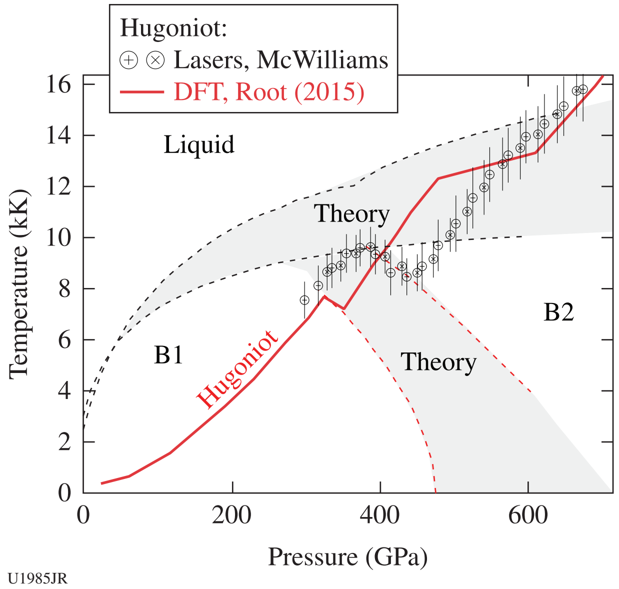

Figure 144.86
Pressure–temperature phase map of MgO.

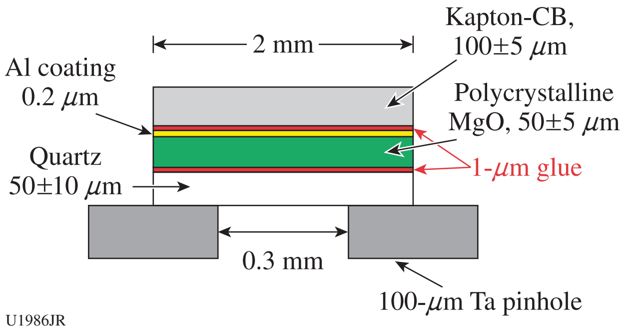

Figure 144.87
Target design for MgODiff-15A, -15D, and MagODiff-EP-15A campaigns.

consists of a 100-μm CH ablator, 50 μm of MgO, and 50 μm of quartz. A steady shock was ablatively driven into the sample by using the sg3702 OMEGA pulse shape or the ERM99V012 OMEGA EP pulse shape,. Once the shock compressed the MgO sample, a second set of laser beams was used to generate a nanosecond source of He$_\alpha$ quasi-monochromatic line radiation (8.3 keV). The x rays scattered off the compressed MgO and the resultant diffraction pattern was recorded on the PXRDIP image plates. A stereographic projection of a typical x-ray diffraction pattern is shown in Fig. 144.88. This information was then used to constrain the MgO crystal structure at pressure. Pressure in the MgO sample during the x-ray probe time was determined by the VISAR diagnostic. The VISAR records the reflecting shock velocity in the quartz window. Hydrocode simulations matched to this shock velocity was then used to determine the pressure in the MgO sample at the x-ray probe time.

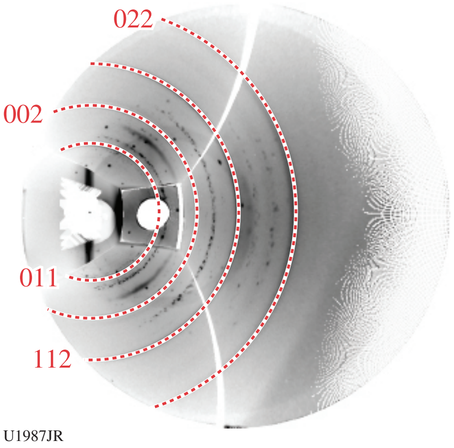

Figure 144.88
Stereographic projection of the OMEGA PXRDIP diagnostic[40] x-ray diffraction image-plate data.

Spectroscopy of Neutrons Generated Through Nuclear Reactions with Light Ions in Short-Pulse Laser-Interaction Experiments

Principal Investigators: C. Stoeckl, U. Schroeder, T. C. Sangster, and C. J. Forrest (LLE)

The experimental objective of this project is to study nuclear reactions in light ions generated in short-pulse laser-interaction experiments. Planar deuterated plastic (CD) targets were irradiated with one short-pulse (10-ps) beam focused at the front surface of the target. A second low-energy (100-J), long-pulse (100-ps) UV beam was fired 0.5 ns ahead of the short-pulse beam to suppress proton acceleration on the front surface of the target. Charged particles, protons, and deuterons from the back side of the target create neutrons and charged particles through nuclear reactions in a second converter target placed closely behind the primary interaction target. The spectrum of the neutrons generated in the converter target is measured using a three-channel scintillator/photomultiplier–based nTOF detector system. Charged-particle detectors are used to measure the spectra of the primary particles.

The previous experiments in FY14 with CD primary and CD or Be/CD secondary targets resulted in neutron spectra showing D–D fusion neutrons for the CD secondary targets and neutrons from $Be^9(d,n)B^{10}$ reactions.

One shot day was allocated for these experiments in FY15. To maximize the probability to see D–T fusion neutrons from the tritium produced in the $Be^9(d,t)Be^8$ neutron pickup reaction, layered targets were used with up to ten alternating layers of 25-μm-thick CD and 25-μm-thick Be foils.

Figure 144.89 shows the neutron energy spectrum from a CD/Be-layered secondary target irradiated with protons and deuterons from a CD primary target at 1.25-kJ laser energy.

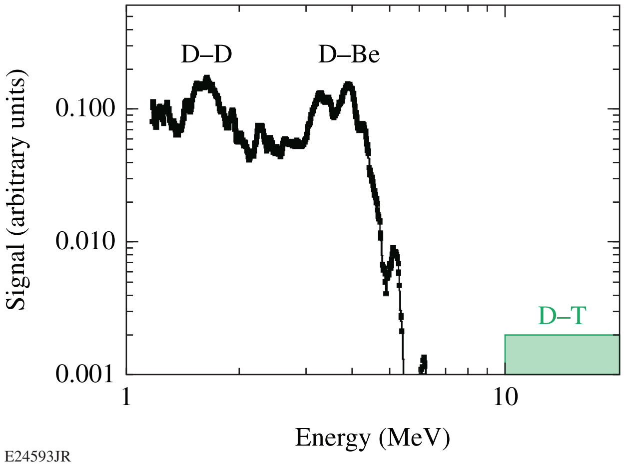

Figure 144.89
Neutron energy spectrum from a CD/Be-layered secondary target recorded at ~150° from the laser's forward direction. Neutrons from D–D fusion and $Be^9(d,n)B^{10}$ reactions are seen, but no D–T fusion neutrons are recorded. The shaded area indicates where the D–T would be recorded.

The neutron energy spectrum shows clear evidence of both D–D fusion neutrons and neutrons from the $Be^9(d,n)B^{10}$ nuclear reaction. A deuteron energy of ~2 to 4 MeV can be inferred from the kinematic shift of the D–D fusion neutrons. The kinematic shift of the $Be^9(d,n)B^{10}$ neutrons is consistent with a lower deuteron energy of 1 to 2 MeV. The difference in the energy of the deuterons is consistent with energy loss of deuterons in the first 25-μm-thick CD layer, which they must traverse before interacting with the first Be layer. No secondary D–T fusion neutrons are observed from any tritium that would be generated in Be^9(d,t)Be^8 neutron pickup reactions, which indicates that the cross section of this reaction is smaller than the calculated values. This discrepancy will be studied further in FY16.

Integrated Channeling for Fast Ignition
Principal Investigator: W. Theobald (LLE)
Co-investigators: S. Ivancic, C. Stoeckl, and D. H. Froula (LLE); K. A. Tanaka, H. Habara, and T. Iwawaki (Osaka University); and P. A. Norreys and L. A. Ceurvors (University of Oxford)

The goal of this LBS project was to perform an integrated fast-ignition channeling experiment on OMEGA and to study the physics of laser channeling through the corona of an imploded shell.

Figure 144.90 displays a schematic of the experimental setup of the joint OMEGA/OMEGA EP experiment. A plastic shell is imploded by the 60 UV beams to create a high-density plasma with an extended corona. A 100-ps ("channeling") IR pulse is injected into the plasma, forming a channel followed by a high-intensity, 10-ps ("heating") pulse generating fast electrons at the channel wall. The shell consists of a 17-μm outer CH layer and a 23-μm inner deuterated plastic layer that is doped with 1% atomic density of Cu. The Cu doping provides K$_\alpha$ fluorescence x-ray emission at 8.048 keV when excited by fast electrons, which is imaged by a spherical crystal imager (SCI). This technique visualizes the fast-electron energy deposition in the compressed shell. The 17-μm-thick CH ablator reduces the excitation of K$_\alpha$ fluorescence from direct interaction of the driver beams and eliminates the neutron background from the hot corona. Our experiments showed, however, that even with the undoped CH ablator, there is still some K$_\alpha$ radiation generated by the implosion. Other diagnostics include two electron spectrometers, an x-ray spectrometer, and neutron time-of-flight detectors to measure the thermonuclear fusion neutron yield from D–D reactions. The temporal evolution of the areal density was calculated with a 1-D simulation with the radiation–hydrodynamic code *LILAC* including cross-beam energy transfer (CBET) and nonlocal electron transport.

Peak compression is predicted at 4.3 ns, where time zero is defined by the start of the drive pulse. The short pulses were injected at four different times between the end of the drive laser pulse (3 ns) and peak compression ($\rho R \approx 400$ mg/cm^2). Figure 144.91(a) shows the SCI image from an implosion without the injection of short pulses. Hot electrons generated by the drive laser in the energy range of several tens of keV's penetrate the outer CH ablation layer and excite K$_\alpha$ emission in the deeper Cu-doped layer. The Cu K-shell ionization cross section peaks at an electron energy of ~30 keV causing

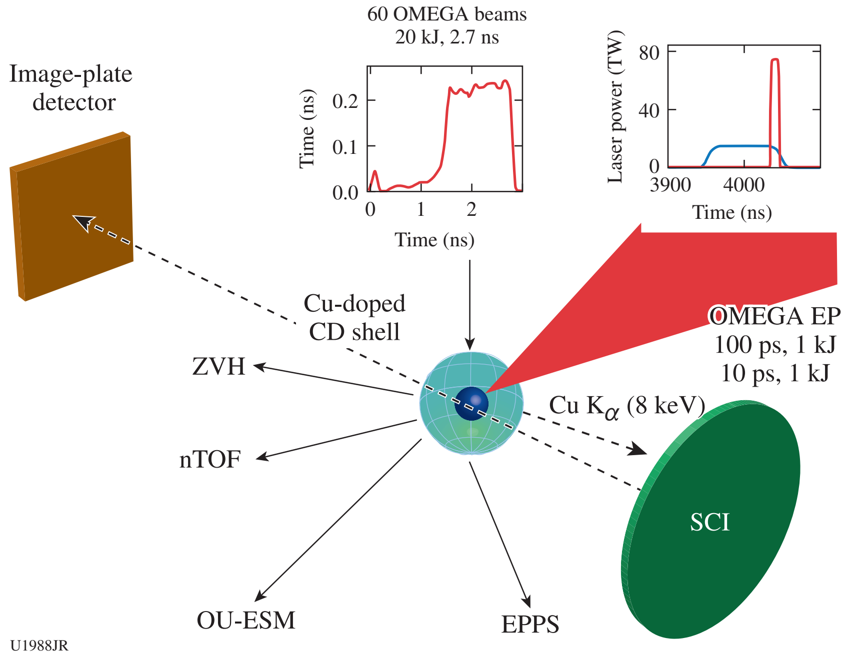

Figure 144.90
Setup of the integrated channeling experiment. ZVH: zinc von Hamos spectrometer; nTOF: neutron time-of-flight; OU-ESM: Osaka University electron spectrometer; EPPS: electron–positron–proton spectrometer; SCI: spherical crystal imager.

these hot electrons to very efficiently produce K_α emission. In addition, x rays from the plasma corona can contribute to the K_α production in the shell. The thickness of the K_α ring is roughly given by $\left[v(t_2)t_2 - v(t_1)t_1\right]$, where v is the implosion velocity of the shell and t_1,t_2 are the times when the K_α emission started and stopped, respectively. Some K_α emission is also produced in the center of the shell from the compressed core at peak compression. Cu-doped plastic material is ablated from the inner wall of the evacuated shell and forms hot dense plasma in the center. The SCI uses a time-integrating image-plate detector so that K_α features that are separated in time all appear on the detector. Figure 144.91(b) renders a view of the SCI diagnostic on the target. Figure 144.91(c) depicts the image when the 100-ps channeling pulses and the 10-ps heating pulses were injected shortly after the drive laser ceased (3.04 ns). The injection time is given by the time of the peak of the 100-ps channeling pulse with respect to the start of the drive laser. The 10-ps heating pulse is injected at the falling edge of the channeling pulse (~50 ps after the peak of the 100-ps pulse). The high-intensity short pulses channel through the plasma corona and produce MeV electrons that excite K_α emission in the shell, now at a position where the shell has moved farther inward, thereby producing the second inner ring. Figure 144.91(d) shows an image when only the 10-ps heating pulse was injected into the imploded plasma at peak compression. A clear enhanced emission in the center of the shell is observed, indicating the coupling of MeV electrons into the compressed core.

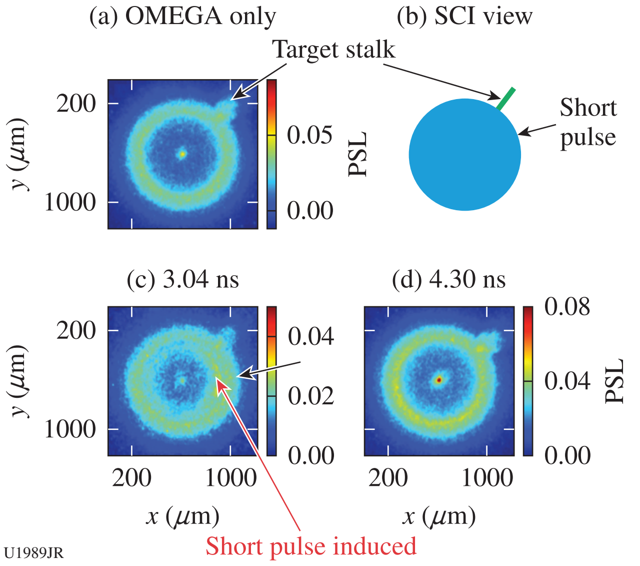

Figure 144.91
Spherical crystal imager (SCI) images from the integrated channeling experiment.

The electron spectrometers captured a very interesting trend in the spectrum of the escaped fast electrons for the different injection times. For an early injection of both pulses, copious amounts of MeV electrons were generated with a clear trend of decreasing fast-electron production for later injection times. At peak compression very few fast electrons were produced. This effect did not occur when only the 10-ps pulse was injected into the plasma at peak compression, producing significant numbers of fast electrons similar to the case when both short pulses were injected at 3.04 ns.

The observed behavior of the channeling beam in the integrated experiment is in sharp contrast to the observations in the OMEGA EP experiment with planar targets,[42] demonstrating better channeling with the 100-ps pulses compared to the 10-ps pulses. It turns out that the plasma conditions were significantly different in both experiments. The implosion produced a long coasting phase with a significant time delay (~1.5 ns) between the termination of the drive laser pulse and the occurrence of peak compression. The coupling of fast electrons into the high-density plasma is optimum at peak compression because at that point the areal density equals the stopping range of MeV electrons. However, the plasma corona significantly cooled during this time period to temperatures that were more than one order of magnitude lower than in the planar target experiment on OMEGA EP. As a consequence, the 100-ps-long pulse probably experienced filamentation, which prevented efficient channeling at peak compression, in contrast to the 10-ps pulse.

Measurements of the Shear Strain of Vanadium Under Shock Compression

Principal Investigator: C. Wehrenberg (LLNL)

This campaign was the first to use *in-situ* diffraction to study shock-compressed vanadium. Multiscale models of vanadium predict high strengths for high-rate loading caused by the increased phonon drag resulting from the high temperatures associated with shock loading. This campaign used three UV beams to drive a zinc backlighter and the fourth UV beam to drive a shock into the vanadium foil. The goal of this campaign was to measure the shear strain in the shock-compressed sample by measuring a difference in strain for different loading directions (corresponding to different diffraction lines). Seven shots were performed and high-quality data were recorded on several shots, with shock loading in the 0.5- to 1.7-Mbar range. Figure 144.92 compares the (a) static (undriven) data and (b) data from a 0.5-Mbar shot. The driven data have a high signal-to-noise ratio and should make it possible to acquire a good measurement of *in-situ* shear strain.

(a) Static shot 20705

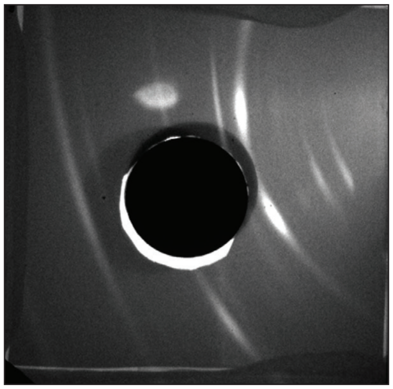

(b) Shot 20703–0.5 Mbar

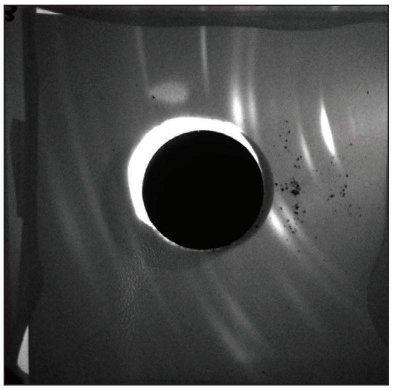

Figure 144.92
(a) Diffraction from static vanadium. (b) Diffraction from vanadium that has been shock compressed to 0.5 Mbar. Strain differences are revealed as changes in the pattern of x-ray diffraction features.

FY15 LLNL OMEGA Experimental Programs

Principal Investigators: R. F. Heeter, K. L. Baker, M. A. Barrios Garcia, M. A. Beckwith, D. T. Casey, P. M. Celliers, H. Chen, F. Coppari, K. B. Fournier, D. E. Fratanduono, C. M. Huntington, A. E. Jenei, R. G. Kraus, D. A. Martinez, J. M. McNaney, M. A. Millot, A. E. Pak, H.-S. Park, Y. Ping, B. B. Pollock, R. F. Smith, C. E. Wehrenberg, K. Widmann, G. W. Collins, O. L. Landen, A. Wan, and W. Hsing (LLNL); and J. Frenje (MIT)

In FY15, LLNL's High-Energy-Density (HED) Physics and Indirect-Drive Inertial Confinement Fusion (ICF-ID) Programs conducted several campaigns on the OMEGA and OMEGA EP Laser Systems, as well as campaigns that used the OMEGA and OMEGA EP beams jointly. Overall, these LLNL programs led 468 target shots in FY15, with 315 shots using only the OMEGA Laser System, 145 shots using only the OMEGA EP Laser System, and eight shots using OMEGA and OMEGA EP jointly. Approximately 25% of the total number of shots (56 OMEGA shots and 67 OMEGA EP shots, including the eight joint shots) supported the ICF-ID Campaign. The remaining 75% (267 OMEGA shots and 86 OMEGA EP shots) were dedicated to experiments for HED physics. Highlights of the various HED and ICF Campaigns are summarized in this section.

In addition to these experiments, LLNL Principal Investigators (PI's) led a variety of Laboratory Basic Science Campaigns using OMEGA and OMEGA EP, including 90 target shots using only OMEGA and 61 shots using only OMEGA EP.

LLNL led a total of 619 shots at LLE in FY15. LLNL PI's also supported 39 NLUF shots on OMEGA and 35 NLUF shots on OMEGA EP in collaboration with the academic community.

Indirect-Drive Inertial Confinement Fusion Experiments

Diamond Sound-Speed Measurements Along the Principal Hugoniot

Principal Investigator: D. E. Fratanduono

Sound-speed measurements along the principal Hugoniot of ablator materials are an important constraint in inertial confinement fusion (ICF) experiments since the sound speed in the ablator influences the instability growth rate. Accurate sound-speed measurements of diamond in this regime would further develop this ablator material and aid our understanding of the ICF instability growth rates. In this campaign, the diamond sound speed was measured using a recently developed perturbation analysis.[43] Specially designed pulse shapes were used on two half-days of OMEGA shots to create a rippled ablation drive. For a monolithic target, the correlation between ripples in the drive and at the shock front can be used to determine the sample sound speed. For the first half-day of experiments, diamond blanking was an issue and no usable data were obtained. For the second half-day, two target designs were fielded. A new design with a preheat shield was used, but the delivered laser energy was too low to produce a reflective shock in diamond. The second target design utilized a two-section target in which perturbations were tracked in both the diamond sample and a quartz witness. By correlating the perturbations in each material and with the assumption that the quartz equation of state (EOS) is known, the diamond sound speed was determined. This alternative design produced excellent experimental data. It was found that these measurements are in good agreement with the preferred EOS table (LEOS 9061) used in ICF simulations (Fig. 144.93).

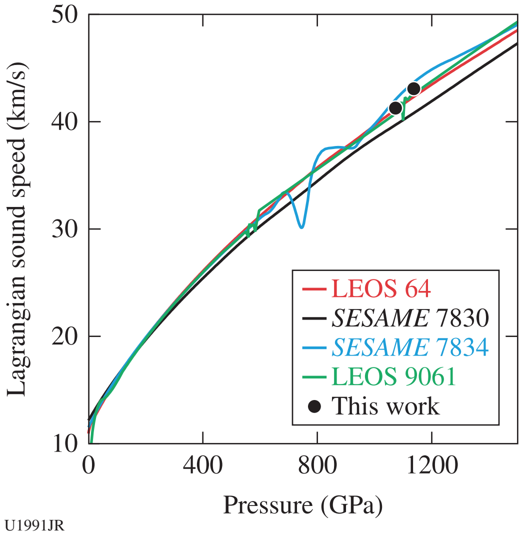

U1991JR

Figure 144.93
Diamond sound-speed measurements compared with equation-of-state (EOS) models.

Mix Effects in Tungsten-Doped Be Capsules Probed with OMEGA EP Short-Pulse Radiography

Principal Investigator: D. Casey

An OMEGA/OMEGA EP joint shot day was dedicated to following up on FY13 results from ablator physics measurements using beryllium capsules. The prior campaign was useful in assessing the performance of Be as an ablator for indirect-drive–ignition experiments on the NIF and also proved to be an interesting mix experiment.[44] The second round of experiments in FY15 used Be capsules driven by gold hohlraums (1.6 mm in diameter by 2.1 mm long by 50 μm thick) that were irradiated by 40 OMEGA laser beams. The shots were diagnosed with the OMEGA neutronics suite as well as radiography using OMEGA EP-driven copper K_α backlighting observed with the spherical crystal imager. The spherical crystal imager gave high-quality radiographs that were both time gated and time integrated. The time-gated images were taken to remove capsule self-emission, but they had reduced photon statistics compared to the time-integrated image plates.

The capsules were 40-μm-thick, 610-μm-diam Be shells with an inner 14 μm of Be also doped with 4% Cu. They were filled with deuterium gas. Several targets also included thin 0.5-μm tungsten (W) layers, either on the inner capsule surface or recessed 5 μm to provide radiographic contrast to test mix models. Figure 144.94 shows the radiograph geometry, a sample OMEGA EP backlit radiograph with the spherical crystal imager, and a time-integrated self-emission image. The x-ray self-emission images show unexpected strong 3-D asymmetry.

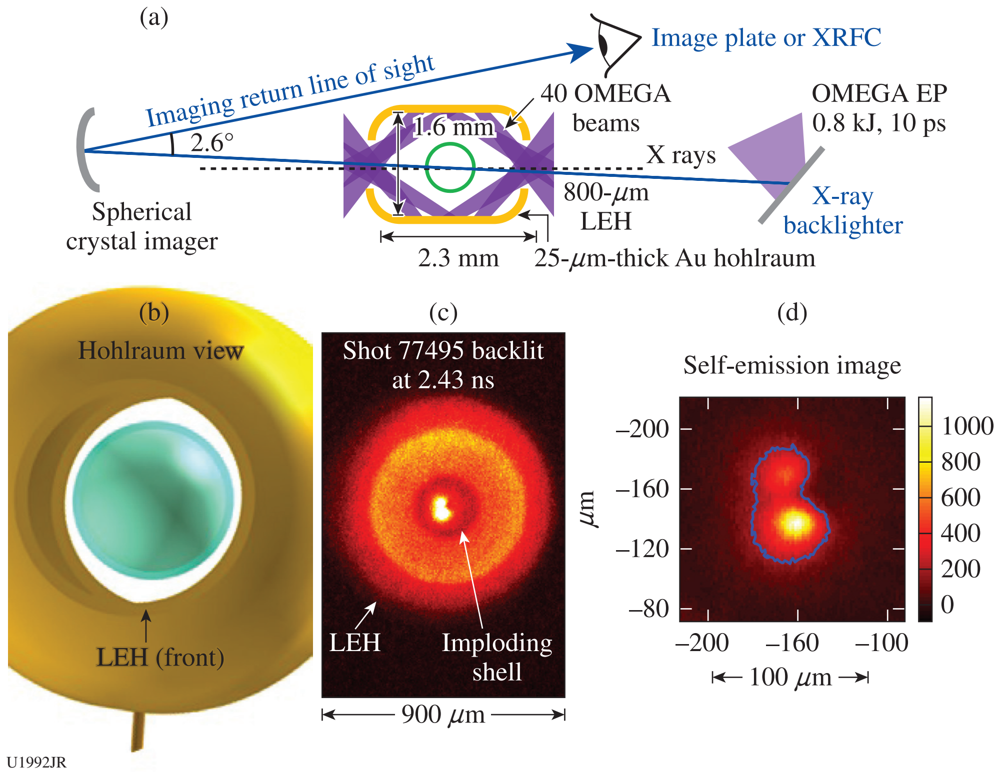

U1992JR

Figure 144.94
(a) Experimental schematic showing the OMEGA EP backlighting geometry using the spherical crystal imager; (b) rendering of the spherical crystal imager's view down the hohlraum axis; (c) backlit image of the shell in flight at 2.43 ns; (d) time-integrated self-emission image of the hot spot, showing strong asymmetry. XRFC: x-ray framing camera; LEH: laser entrance hole.

Three types of capsules were shot, as shown schematically in Fig. 144.95. Figure 144.95 also summarizes the yield and T_i observed with the neutronics suite. The yield behavior is interesting, showing larger variability than observed in FY13, both with and without tungsten. Surprisingly, the buried-tungsten data have lower yields than tungsten at the gas/shell interface. Detailed comparisons with simulations are now underway.

Hohlraum Drive Measurements Using a Shock Witness Plate

Principal Investigator: K. L Baker
Designers: S. MacLaren and R. Olson

The purpose of this OMEGA half-day campaign was to measure the temporal and spatial profiles of the drive in a hohlraum using a VISAR package on the side of the hohlraum and then to assess whether this technique could be used to directly detect laser beams irradiating the wall of the hohlraum. Such a method can be used to evaluate cross-beam energy transfer. As shown in Fig. 144.96, these experiments used a two-shock laser pulse, SS1503vA01, hitting a vacuum gold hohlraum oriented along the P6/P7 axis with a gold M-band block/ablator material placed on a quartz window in one part of the hohlraum wall. This campaign set the stage for subsequent similar NIF VISAR shots, which have shown that the gold M-band block can itself result in multiple shocks not predicted in simulations, perhaps caused by the gold/quartz rarefaction wave interacting with the ablation front, so a future campaign would preferably use an aluminum ablator. On these OMEGA shots, a 2.5-mm VISAR cone partly protected the window from unconverted light; however, because of the potentially large light level entering the chamber (up to 4%), a much longer VISAR cone (>8 mm) would be recommended on future campaigns.

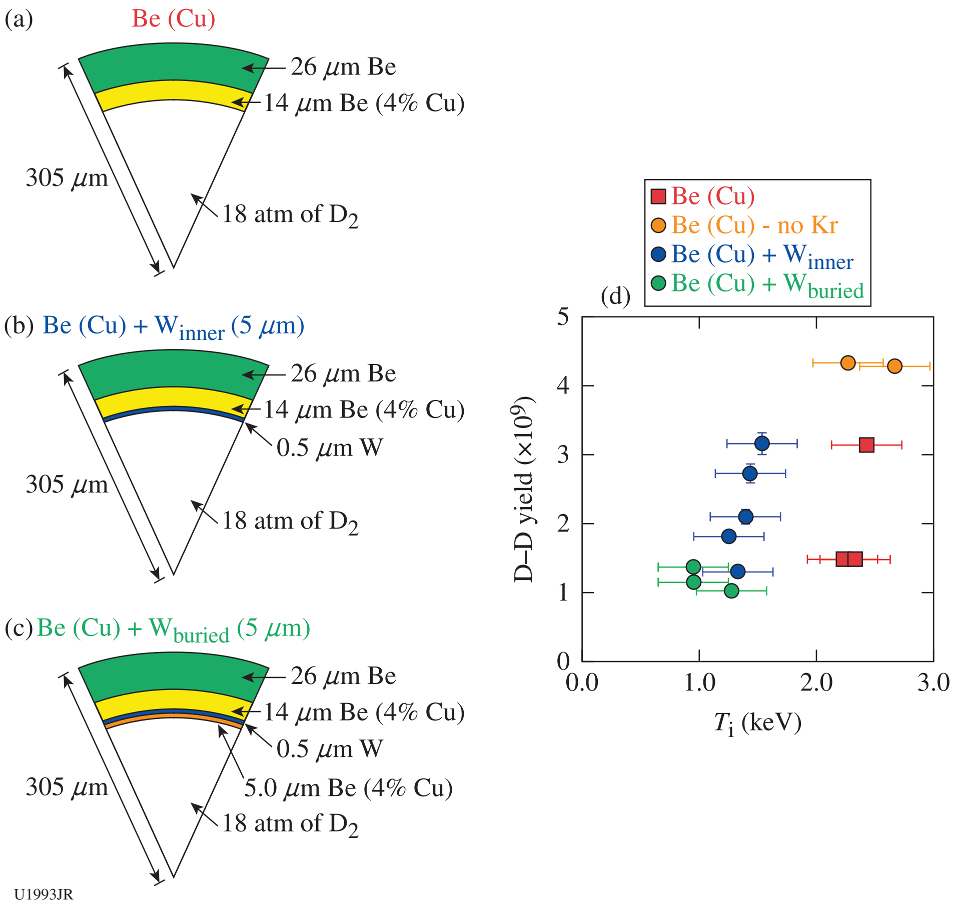

Figure 144.95
(a) Cu-doped Be capsule schematic; (b) Cu-doped Be capsule schematic with a 0.5-μm W layer at the gas/shell interface; (c) Cu-doped Be capsule schematic with a 0.5-μm W layer recessed 5 μm from the gas/shell interface; (d) summary of the D–D neutron yield and measured T_i for each configuration. W: tungsten.

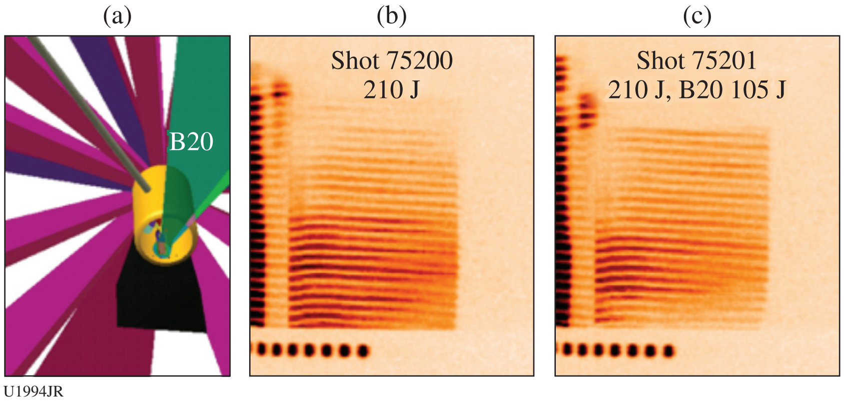

Figure 144.96
(a) VisRad image of the hohlraum with Beam 20 directly hitting the ablator located on the VISAR window; (b) VISAR measurement of the drive with Beam 20 not hitting the VISAR window; (c) VISAR measurement of the drive with Beam 20 hitting the VISAR window.

Fast X-Ray Imaging Using Optical Interferometry

Principal Investigator: K. L. Baker
Co-investigators: P. Celliers and M. Tabak

The purpose of this campaign was to demonstrate high spatial and temporal resolution x-ray imaging using the optical VISAR and OHRV diagnostics. This approach used a semiconductor, with the side facing the backlighter capsule coated with a thin aluminum reflecting layer. X rays pass through the metal layer and get absorbed in the semiconductor, changing its index of refraction. The other side of the semiconductor was antireflective (AR) coated to allow the VISAR or OHRV probe beam to probe the phase of the semiconductor as the x rays were absorbed in the semiconductor. This technique is capable of acquiring subpicosecond 2-D or 1-D x-ray images with detector spatial resolution of better than 10 μm and offers the ability to operate in the high neutron flux environment expected on ignition shots with burning plasmas. This experiment used 39 beams of the OMEGA laser to implode an 890-μm-diam, 9-μm-thick backlighter capsule with a 1-ns pulse length. The x-ray emission was then imaged onto a diamond or quartz semiconductor, using a miniature x-ray snout as shown in Fig. 144.97(a). As displayed in Fig. 144.97(b), the VISAR then probed the semiconductor from the back and measured the induced phase change inside the semiconductor caused by the impinging x rays. A lineout of the semiconductor phase change measured by the VISAR is then compared to channel 11 of the (slower) Dante x-ray diode array in Fig. 144.97(c).

Rayleigh–Taylor Growth Measurements on Aluminum Ablators

Principal Investigator: D. Casey

Aluminum has attractive properties as a potential ICF ablator, including the ability to shield Au hohlraum M-band emission without dopants because of its mid-Z opacity (it is a single

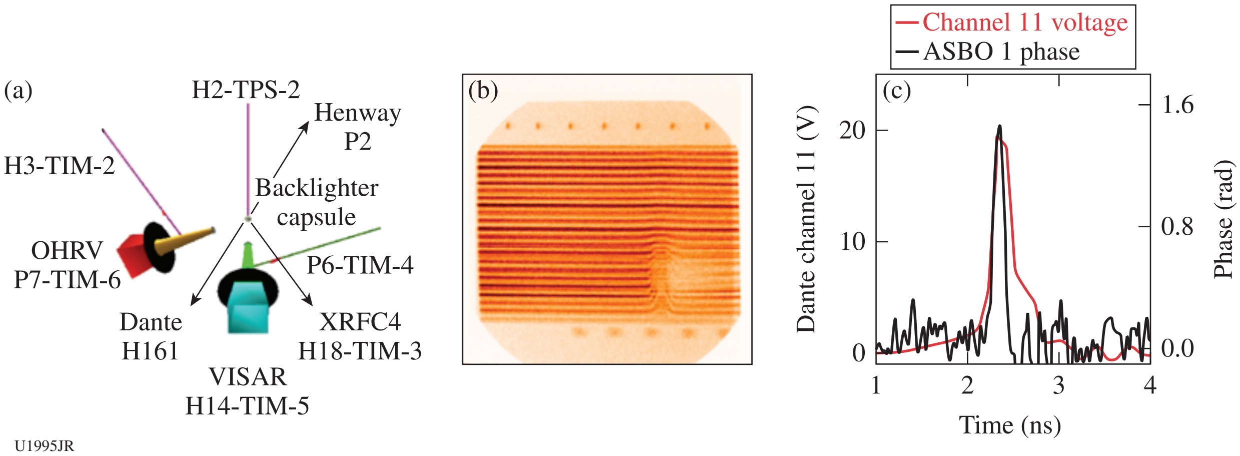

Figure 144.97
(a) VisRad image of the experimental setup to image the backlighter capsule onto a semiconductor; (b) VISAR measurement of the x-ray–induced phase change in the semiconductor; (c) lineout comparison of the Dante channel 11 trace (red) with the VISAR trace (black).

species material and has a well-understood equation of state). On the other hand, the presumptive low ablation velocity and high opacity may make it more unstable to the Rayleigh–Taylor (RT) instability compared to other ablators such as Be, high-density carbon (HDC), and CH. Some predictions suggest, however, a double ablation front may form (thermal and M band), which may decrease RT growth by increasing the ablative stabilization through a larger effective density scale length. This joint shot day sought to measure RT growth rates in Al using face-on radiography and to develop a platform for testing the possible impact of a double ablation-front feature. This work complemented a LANL experiment conducted the same week to measure the mass ablation rate of Al. The aluminum RT growth data that were obtained will be compared to calculations. Progress was slowed by an anomalously early Au-halfraum closure obscuring the backlighter, which limited the number of drives that could be tested, but enough data were obtained to do initial comparisons to simulation. Figure 144.98 shows the sidelighter/halfraum configuration used to constrain the trajectory of the Al package. Figure 144.99 shows the face-on RT data obtained at 3.7 ns.

Hohlraum Magnetization Using Laser-Driven Currents

Principal Investigator: B. Pollock

Co-investigators: J. Moody, J. S. Ross, D. Turnbull, C. Goyon, A. Hazi, G. Swadling and W. Farmer

In FY15 during the two days allocated on OMEGA EP, the Hohlraum Faraday Rotation Campaigns continued to investigate the feasibility of self-magnetizing hohlraum targets for ICF applications. The basic target design consists of a half-loop

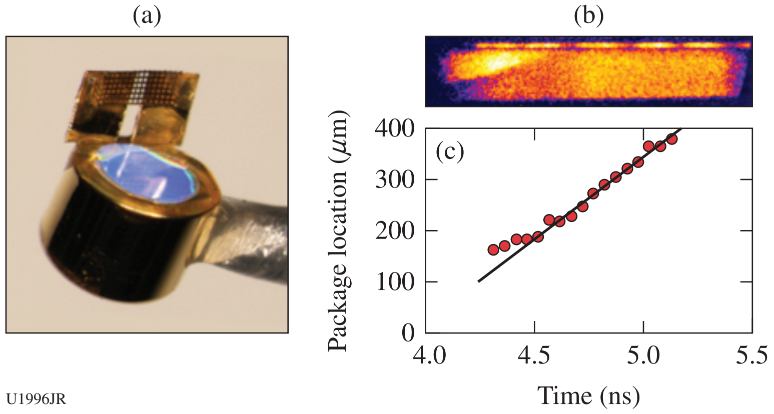

Figure 144.98
(a) Sidelighter/halfraum used to measure trajectory of the Al package; (b) raw streak camera radiograph of sidelit Al package; (c) measured Al package trajectory, which will provide a good constraint on Al ablation properties and hohlraum drive.

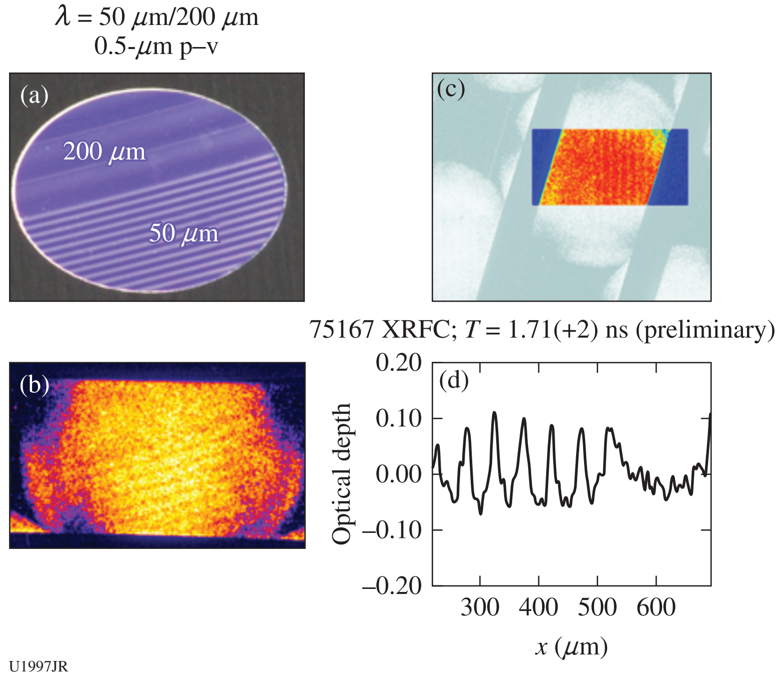

Figure 144.99
(a) An aluminum RT package with 200-μm and 50-μm sinusoidal modulations; (b) raw x-ray framing-camera radiograph of an aluminum RT package at 3.7 ns; (c) orientation of lineout to analyze the optical depth; (d) optical-depth lineout from region shown in (c), showing good observed modulation growth. p–v: peak-to-valley.

formed by folding a thin gold sheet around a 500-μm-diam fused-silica rod. On the open side of the loop are parallel plates; holes were placed into one of the plates so that the OMEGA EP long-pulse beams could shine through to produce a plasma at the surface of the second plate, as shown in Fig. 144.100. Hot electrons formed at this plasma collect around the holes in the first plate, essentially charging up a parallel-plate capacitor. The half-loop connects the plates, allowing current to flow and produce a magnetic field on the loop axis. The first FY15 campaign studied variations on this approach by changing the longitudinal structure of the loop portion of the target and expanding the loop diameter. The OMEGA EP 4ω probe capability was employed to directly measure the magnetic field inside the loop via Faraday rotation along the hohlraum axis. Fields up to 4.6 T were measured at the time of the probe beam. On the second shot day, the short-pulse backlighter beam was used to drive a proton source for proton deflectometry measurements of the fringing magnetic fields around the target (Fig. 144.101). This campaign allowed us to conduct additional parameter scans and extended the previous data set. This shot day included collaborators from ILE (Osaka University) whose initial analysis on the proton data indicates that magnetic fields of ~70 T can be produced in the standard target geometry. The analysis of this recent experiment is ongoing and will be used as a guide for the FY16 continuation of this effort.

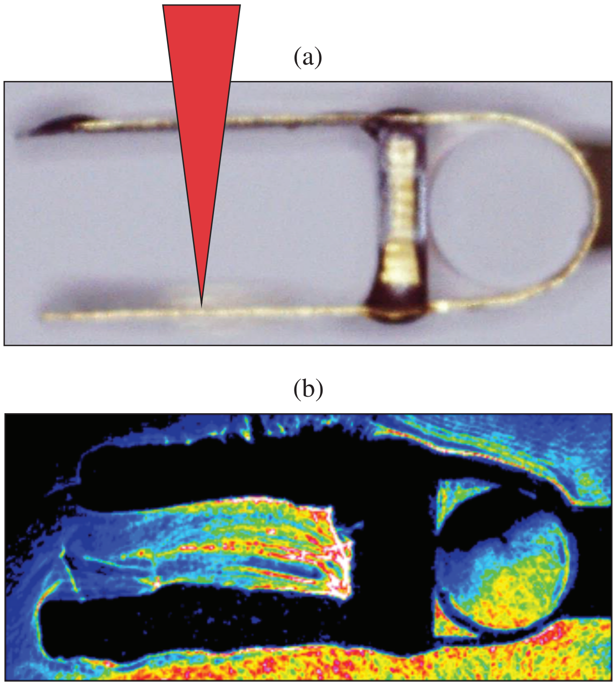

Figure 144.100
(a) Geometry for hohlraum (end view) self-magnetization on OMEGA EP with the beam path shown schematically in red; (b) a sample of 4ω probe data used to infer Faraday rotation.

Hohlraum-Free Platform for X-Ray–Driven Equation-of-State Measurements

Principal Investigator: P. M. Celliers

Co-investigators: D. E. Fratanduono (LLNL); and M. Karasik, S. Obenschain, and A. Schmitt (NRL)

During FY15 the Hohlraum-Free Campaign was carried out over two shot days on OMEGA EP. This campaign performed experimental tests of a hybrid platform for driving planar steady shocks into equation-of-state (EOS) target packages. The

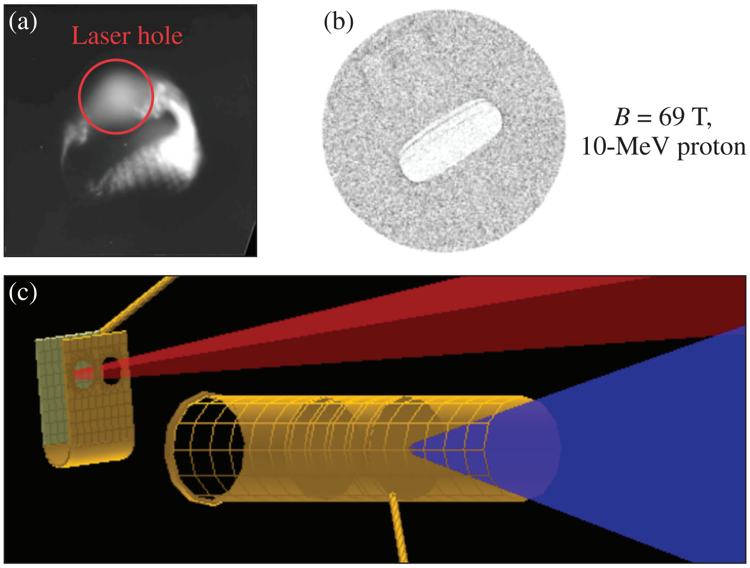

Figure 144.101
(a) Analysis of the proton evacuated region; the inferred field along the axis of the loop interior is 69 T. (b) Sample of proton data corresponding to (a); (c) geometry for proton deflectometry on OMEGA EP with the proton detector 15 cm behind the B-field target.

platform concept combines features of both direct and indirect drive by using a high-Z layer to convert the laser drive into a soft x-ray source in proximity to a low-Z ablator. The ideas behind this concept were proposed by the experimental team based at NRL (Karasik, Obenschain, and Schmitt). The high-Z layer is typically of submicron thickness—for example, a few hundred nanometers of Au or Pt, followed by a conventional low-Z ablator material (polystyrene or kapton). This drive assembly is then mounted onto an EOS package consisting of a reference standard and sample materials. The shot campaigns were aimed at examining the pressure scaling, shock quality, and other performance details of this platform for drive intensities up to 5×10^{14} W/cm^2. For our tests we used a radiation-blocking layer of several microns of Cu or Au followed by thick quartz witness samples. The shock transmitted into the quartz was diagnosed with VISAR to determine the drive pressure.

The first experimental campaign encountered significant issues with blanking of the VISAR signals for drive intensities exceeding 2×10^{14} W/cm^2. Analysis of the signals suggested that the blanking was caused by hot electrons circulating around the target package from the ablation plasma. These electrons might deposit enough energy on the rear surface of the quartz witness to render the quartz opaque. The targets were all assembled with 5-mm-diam shield washers—a size that was requested by the facility to minimize debris loading in the target chamber. The facility subsequently investigated the blanking issue by testing various sizes of shield washers and found that 10-mm washers should be adequate for most experiments.

The second campaign repeated the scaling experiments using packages fitted with 10-mm washers and also made adjustments to the laser pulse shape. A complete dataset was obtained with enough information to construct a drive scaling curve that will be beneficial to the design of future tests of this platform, on both OMEGA EP and the NIF.

Broadband Proton Radiography of Shock Fronts in Gases

Principal Investigator: Y. Ping
Co-investigators: H. Sio (MIT); G. W. Collins (LLNL); and R. Hua, C. McGuffey, and F. Beg (University of California, San Diego)

Two days were dedicated to developing a new experimental platform on OMEGA EP to study shock-front structure and field effects in low-density systems. The broadband proton backlighter was generated by high-intensity, short-pulse interaction with metal foils through the well-known TNSA (target normal sheath acceleration) process. The shock was driven into a gas cell or freestanding foams by three UV long-pulse beams. Both shot days provided excellent proton radiographs of shock propagation in gases and foams. Figure 144.102(a) shows a radiograph from the first shot day, using 5-MeV protons to probe a shock driven by 1.5 kJ of UV energy in 1 ns. A ring structure is clearly observed, indicating the accumulation of protons at the shock front, consistent with the existence of an electric field. For the second shot day, the intensity and energy of the proton beam were substantially enhanced by an improved target design and higher short-pulse energy. Using a stronger long-pulse drive (6.2 kJ total), a double-shell structure,

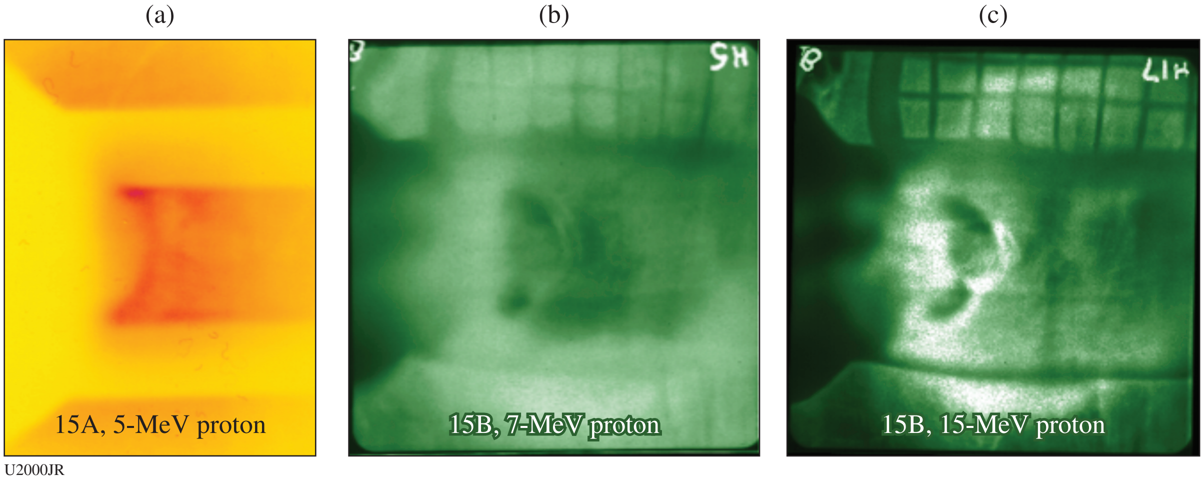

Figure 144.102
(a) A 5-MeV proton radiograph of a gas cell from 15A shots. (b) 7-MeV and (c) 15-MeV proton radiographs from 15B shots, showing the double-shell structure together with a separate spatial fiducial grid.

which is proton-energy dependent, was observed, as shown in Figs. 144.102(b) and 144.102(c). A paper on this new platform is being prepared and further analysis of the radiographs is in progress.

High-Energy-Density Experiments

1. Material Equation of State Using Diffraction Techniques

Shock Melt and Ramp Recrystallization of Tin

Principal Investigator: R. G. Kraus
Co-investigator: F. Coppari

The ultrahigh-pressure melt curve (e.g., >3 Mbar) is a difficult region of phase space to access experimentally. The combined high pressures and temperatures are often out of reach of standard diamond anvil cell techniques. Shock compression to such high pressures generates significantly higher temperatures than are necessary to melt the material. Consequently, this campaign utilizes a recently developed technique to shock the material of interest into the fluid phase and subsequently compress it back into the solid phase, using *in-situ* x-ray diffraction to confirm the existence of a periodic crystal structure.

One shot day on OMEGA EP was used to shock tin to pressures ranging from 65 to 75 GPa (all fully molten initially) and then used a second shock to compress the high-pressure liquid tin back into the solid stability field at pressures ranging from 130 to 170 GPa. Pressure-induced crystallization from a liquid state was observed on four of the experiments, starting at shock pressures of 65 and 75 GPa. Figure 144.103 presents a preliminary summary of the shock–melt–resolidification data in a pressure-entropy phase diagram for tin (based on Carl Greef's *SESAME* 2161 EOS). The pressure-entropy space is a useful phase space in which to interpret these experiments since nearly all the entropy is generated from the first shock to the principal Hugoniot and the subsequent second-shock compression is nearly isentropic. Figure 144.103 also includes data on shock melting of tin from the previous FY14 campaign.

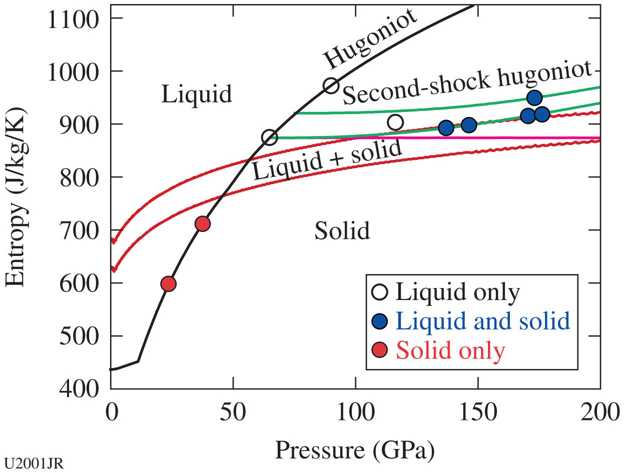

Figure 144.103
Diffraction data for shock-induced melting and resolidification presented in the pressure-entropy phase diagram for tin. Entropy states are determined from Carl Greef's *SESAME* 2161 EOS for tin. Shock compression to the Hugoniot state (black line) increases the entropy and melts tin for shock pressures greater than ~55 GPa. Resolidification data are plotted along the double-shock Hugoniots (green lines), which deviate minimally from the isentropic path (horizontal magenta line).

High-Pressure Melting of Tantalum as Determined by In-Situ X-Ray Diffraction

Principal Investigator: R. G. Kraus
Co-investigators: F. Coppari and D. Fratanduono

The high-pressure melting curve of tantalum has generated significant interest in the high-pressure community because of the large discrepancy between the static diamond anvil cell experiments and the gas-gun shock-wave experiments (as diagnosed by sound-speed measurements). This OMEGA half-day campaign investigated the high-pressure phase diagram and also a potential issue with the shock-wave experiments: the time dependence of the melting transition in tantalum.

This campaign used the PXRDIP diagnostic to perform *in-situ* x-ray diffraction measurements of the shocked state of tantalum. *In-situ* x-ray diffraction is an excellent diagnostic for determining the melting transition since one can observe the existence of the liquid phase as a diffuse scattering feature, as well as the loss of solid diffraction.

Pressure in the FY15 experiments ranged from 200 to 340 GPa in the tantalum. Figure 144.104 shows select lineouts from the diffraction data, where one can observe with an increasing pressure the loss of solid diffraction lines and the increase in the diffuse scattering feature around the (110) line of bcc tantalum with increasing pressure. It is found that incipient melting occurs between ~240 and ~270 GPa and that complete melting occurs between ~300 and ~315 GPa, which is completely consistent with the gas-gun data, suggesting that the time scale for shock-induced melting is much faster than our nanosecond experiments.

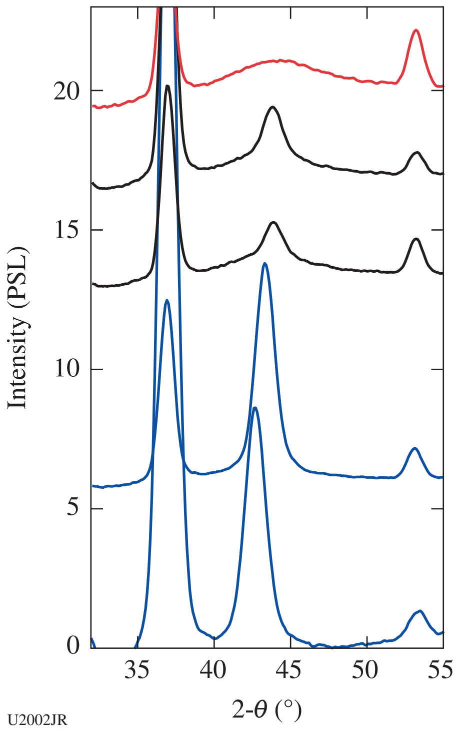

Figure 144.104
Lineouts from *in-situ* x-ray diffraction experiments on shocked tantalum. Lines are offset for clarity, where in order from bottom to top the shock pressures were 202(8), 250(15), 290(14), 307(10), and 354(18) GPa. Blue lines represent completely solid-state tantalum, black lines represent solid + liquid states, and the red line represents only a liquid state.

Understanding Strength and Structure of Shock-Compressed Diamond

Principal Investigator: F. Coppari
Co-investigators: C. Wehrenberg and J. Eggert

Single-crystal diamonds are currently used as ablator and window materials in powder diffraction experiments performed on both OMEGA and the NIF. Understanding diamond's behavior under dynamic ramp compression and how strength affects its properties are crucial to the design of the diffraction experiments and the interpretation of the results.

Models predict that below the Hugoniot elastic limit (HEL), diamond is elastically deformed and assumes a strained cubic structure. Above the HEL, plastic deformation should bring diamond back to the cubic structure. What happens to diamond under ramp compression is currently unknown.

The goal of this first half-day experiment was to demonstrate that Laue diffraction data could be obtained from such a low-Z material under shock compression. Laue diffraction experiments of diamond, shock compressed below and above the HEL, were performed using the BBXRD diagnostic. Very nice data were obtained (Fig. 144.105) showing differences in the Laue patterns for shocks below and above the HEL. Given the good quality of the data, quantitative data analysis will be possible and will provide a suitable starting point for designing future ramp-compression experiments.

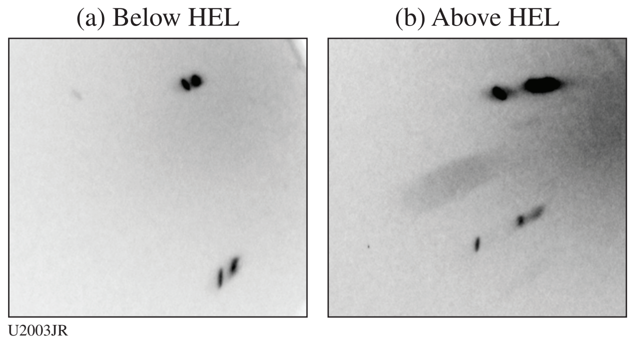

Figure 144.105
Laue diffraction patterns for diamond shock compressed (a) below and (b) above the Hugoniot elastic limit (HEL).

Development of Germanium X-Ray Backlighters for Diffraction Experiments

Principal Investigator: F. Coppari
Co-investigators: J. Eggert and R. Smith

In high-pressure dynamic diffraction experiments, the signal/background deteriorates as the pressure increases above ~7 Mbar because of the increase in the background caused by the laser ablation. To shield this background, metallic filters are used to cover the image-plate detectors, whose material (usually) matches the x-ray source. On OMEGA, Fe (6.7-keV) and Cu (8.2-keV) x-ray sources were previously developed for diffraction experiments, but these are not optimized for shots in the TPa regime since the ablation x-ray background enters the backlighter energy range and can no longer be filtered. This campaign developed a higher-energy x-ray source (Ge He_{α} at 10.2 keV) to improve the signal/background in high-pressure shots by enabling more-effective shielding of the background x rays.

This half-day campaign varied the laser intensity used to drive the Ge backlighter to find the maximum conversion efficiency. Maximum x-ray emission was obtained using a double-sided illumination of the Ge foil at an intensity of 9×10^{14} W/cm^2. Figure 144.106 shows a typical Ge spectrum. These shots also ramp compressed Fe up to 7 Mbar to see how the diffraction data improved in high-pressure shots. Figure 144.107 compares two different shots at similar peak pressures, using the old (Cu) and new (Ge) x-ray sources. Measurement quality was improved with the Ge backlighter, where the diffraction lines spanned the entire image plate and were not suppressed by the high background.

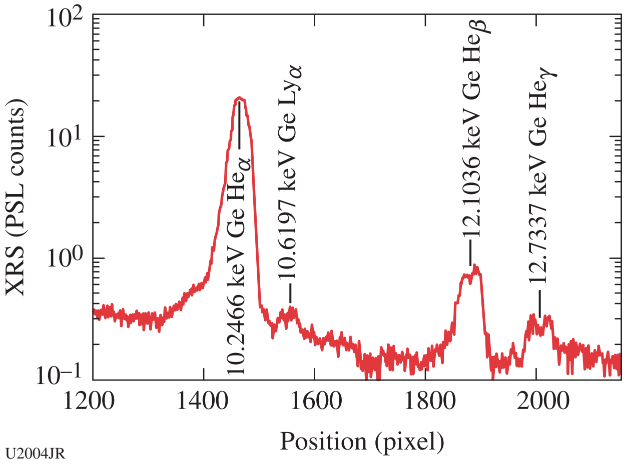

Figure 144.106
Typical spectrum emitted by the Ge backlighter, as recorded by the XRS Rowland spectrometer on OMEGA.

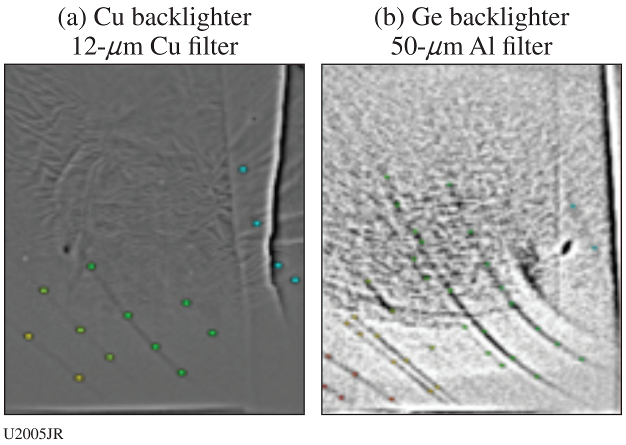

Figure 144.107
Comparison of the diffraction signals obtained with (a) Cu and (b) Ge x-ray sources for a similar drive.

Shock-Melting Transition in Iron as Determined by In-Situ *X-Ray Diffraction*

Principal Investigator: R. G. Kraus
Co-investigators: F. Coppari and D. Fratanduono

The high-pressure melting curve of iron is critical to our understanding of the earth since it provides a reference point for the temperature deep within the core. This half-day OMEGA campaign investigated the high-pressure phase diagram of iron, particularly the pressure for incipient melting. It also explored a potential issue with the shock-wave experiments: the time dependence of the melting transition in iron. The PXRDIP diagnostic was used to perform *in-situ* x-ray diffraction measurements of the shocked state of iron. *In-situ* x-ray diffraction is an excellent diagnostic for determining the melting transition since one can observe the existence of the liquid phase, as a diffuse scattering feature, as well as the loss of solid diffraction. Pressure in these experiments ranged from 200 to 300 GPa in the iron. This campaign significantly improved the accuracy of the shock-state determination through improved pulse shaping. It was found that incipient melting occurs between ~205 and ~220 GPa and complete melting occurs by ~300 GPa. This is consistent with earlier gas-gun data, suggesting that the time scale for shock-induced melting is much faster than these nanosecond time scale experiments.

Understanding Diffraction Signals from Single-Crystal Diamond Windows

Principal Investigator: F. Coppari
Co-investigator: J. Eggert

Single-crystal diamonds are currently used as ablator and window materials in powder diffraction experiments on OMEGA, OMEGA EP, and the NIF. Understanding diamond's behavior under ramp compression, along with its diffraction signal, is critical to correctly interpret diffraction data for other materials since the measurement includes diffraction from the diamond ablator and window as well as the chosen sample material.

In Bragg diffraction experiments (using a monochromatic x-ray source), one does not expect to record signals from single-crystal materials unless the Bragg condition is satisfied for a particular reflection at that wavelength. The resulting diffraction signal is then a localized spot. The OMEGA and NIF data most often show a very bright, highly textured spot with noticeable broadening in the Bragg angle. This feature could be consistent with Bragg diffraction initially from single-crystal diamonds, whose symmetry gets partially destroyed by the ramp compression. Another interpretation could be that this is the diffraction of a highly textured sample material, rather than the diamond window.

To unambiguously assign the observed feature to either diamond or sample, our experiments, performed over one day on OMEGA EP, reproduced the compression used in past shots, but here the target did not have any sample material—just a bare diamond. Figure 144.108 shows a representative result. The extended lines are from the Ta pinhole (reference material); the diamond signal is highlighted by the red oval and detailed in the inset. The signal is characterized by a localized spot corresponding to diffraction from ambient pressure diamond, in addition to a broad, textured peak at a higher angle corresponding to compressed diamond. This feature is indicative of the pressure gradient existing in diamond when the x-ray source is turned on.

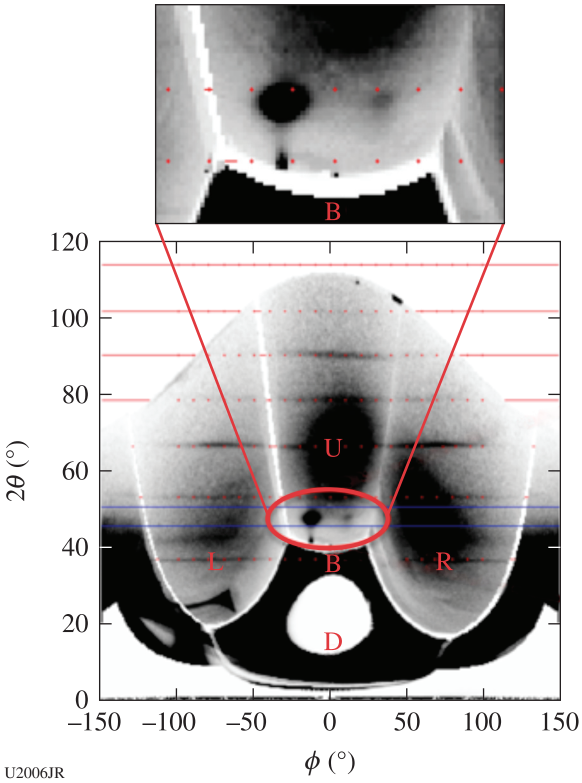

Figure 144.108
Representative diffraction pattern of ramp-compressed diamond. The straight lines are from ambient-pressure Ta used as reference material. The inset highlights the characteristic signal from the diamonds.

Development of a Novel X-Ray Diffraction Platform for Constraining the High-Pressure Melt Curve

Principal Investigator: R. G. Kraus
Co-investigator: F. Coppari

The high-pressure melt curve is tremendously useful for equation-of-state (EOS) modeling since it provides a reference line on the EOS surface where the free energy of the liquid equals that of the solid. The melt curve is also critical to hydrodynamic modeling since it defines the boundary between a material with strength and one without. Because of its importance, our team has been developing *in-situ* x-ray diffraction techniques to determine the high-pressure melt curve, including the results from x-ray diffraction of shock-induced melting in tantalum and iron and shock-ramp resolidification techniques for tin. The campaign described here used one day on OMEGA EP to develop a novel technique to constrain both the equilibrium high-pressure melt curve and the kinetics of resolidification. In this platform, a sample is shocked to high pressures, released into the liquid phase, and then recompressed back into the solid stability field. This campaign also tested a new ablator material for reducing the ablation plasma background. With this novel shock–release–resolidification platform, lead (Pb) was shocked to approximately 50 GPa, released into the liquid phase at ~20 to 30 GPa, and then recompressed back into the solid stability field at ~50 GPa. Figure 144.109 presents data from two image plates

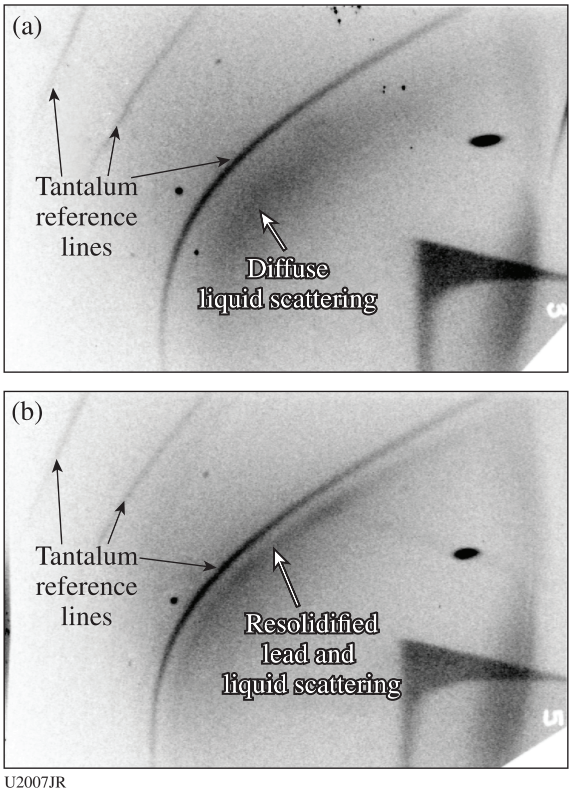

Figure 144.109
Image plates showing x-ray diffraction from the tantalum pinhole plate (used to reference the image plate's location) and from the lead sample. (a) X-ray diffraction was timed just after the lead sample was shocked to 50 GPa and released to 15 GPa. (b) X-ray diffraction was timed when the sample was shocked to 50 GPa, released to 15 GPa, and then recompressed back to 50 GPa. Note: All data and interpretations are preliminary.

showing *in-situ* x-ray diffraction data from (a) shock–released liquid lead and (b) shock–released–resolidified lead. Based on these preliminary but exciting results, this technique will be useful for constraining the time dependence of pressure-driven solidification and the high-pressure equilibrium phase diagram.

2. Material Equation of State Using Other Techniques

Measurements of the Lithium Hydride and Cubic Boron Nitride Equations of State

Principal Investigator: A. E. Lazicki
Co-investigators: F. Coppari, R. London, D. Erskine, D. Fratanduono, D. Swift, P. Celliers, J. Eggert, G. Collins, H. Whitley, J. Castor, J. Nilsen, and I. Otero

This campaign performed measurements extending the principal Hugoniot of LiF and cubic BN up to the 30-Mbar pressure range, more than doubling the previous high-pressure limit for experiments on these materials. LiF is a common window material in dynamic measurements and potentially useful as an impedance-matching standard; cubic BN is an ultrahigh hardness diamond analog material with important technological applications.

High pressures were exerted using direct (first shot day) and indirect (second shot day) drive of layered planar targets. Measurements were made using the active shock breakout (ASBO) diagnostic to track *in-situ* shock velocities and the streaked optical pyrometer (SOP) diagnostic to collect thermal self-emission. Pressure and density were determined using impedance matching to quartz;[45] thermal emission from quartz was also used as the standard for determining temperature.[46,47] LiF Hugoniot data for one of the shots are shown in Fig. 144.110. Analysis is in progress.

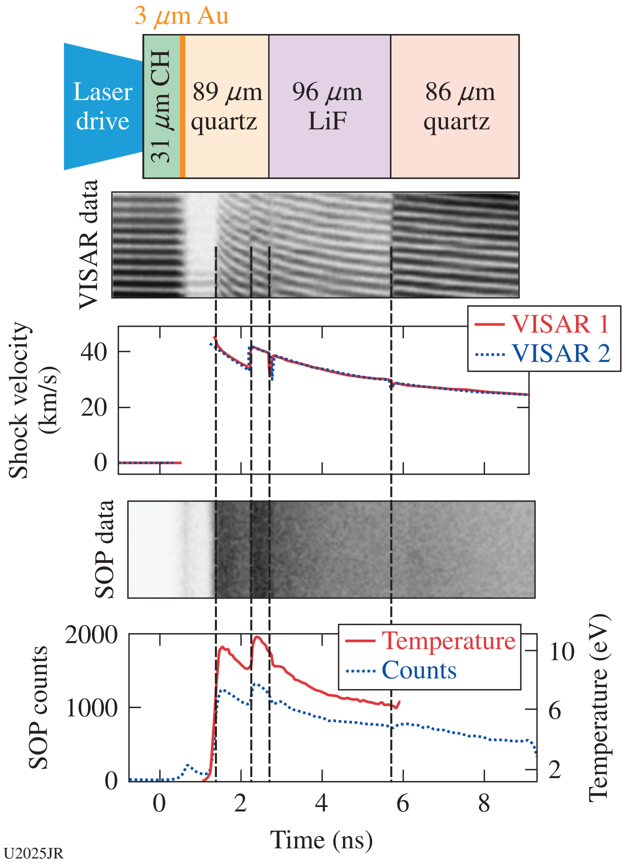

Figure 144.110
Experimental configuration, raw data, and extracted shock velocities and temperature from shot 75261.

Copper and Aluminum Ramp-Compression Experiments

Principal Investigator: D. E. Fratanduono

In support of ramp-compression experiments at the National Ignition Facility (NIF), ramp-compression experiments of monolithic aluminum and copper were performed on OMEGA. The goal of these experiments was to test alternate ablators that can be used for the experiments on the NIF. Over two half-days, both copper and aluminum targets were examined. The target design consisted of a vacuum halfraum with a monolithic stepped target (either copper or aluminum) attached to one end of the halfraum. Pulse shapes were designed to produce quasi-isentropic loading of the samples to ~3 Mbar. For the aluminum targets, pulse-shaping limitations precluded ramp compression to such pressures, but copper was ramp compressed to 3 Mbar. The experimental results are in good agreement with both ramp-compression measurements performed on the Z Machine at Sandia and the NIF. The data were used in the HED materials ramp-compression working group to help guide future NIF ramp-compression experiments.

Ramp Compression of Single-Crystal Diamond

Principal Investigator: D. E. Fratanduono
Co-investigators: D. Braun, R. Smith, and D. Swift

A half-day of single-crystal diamond ramp-compression experiments were conducted on OMEGA in FY15. Excellent data were obtained on all shots, which have already influenced the design of future TARDIS (target diffraction *in-situ*) experiments on the NIF. Experiments were conducted as a result of the 2013 High-*Z* Review. Committee members questioned whether the stress-density response of chemical-vapor–deposited (CVD) diamond (polycrystalline) measured by Bradley in 2008 on OMEGA and Smith in 2012 on the NIF were adequate for

TARDIS experiments that use single-crystal diamond. These OMEGA experiments were designed to measure the stress-density response of two-diamond crystal orientations ($\langle 100 \rangle$ and $\langle 110 \rangle$). Comparisons (A to B) were performed with three different pulse shapes, the goals of which were: first, to ramp compress through the Hugoniot elastic limit (HEL); second, to shock through the HEL; and third, to test the influence of a gold preheat shield on the ramp profile. Stress-density response was measured in all experiments. Preliminary results suggest that the $\langle 110 \rangle$ response is consistent with the CVD results of Bradley. Further, results indicate that the "pullback" features observed in NIF experiments are significantly reduced in the $\langle 110 \rangle$ orientation when compared to $\langle 100 \rangle$. *LASNEX* has better predictive capability with the $\langle 110 \rangle$ orientation versus $\langle 100 \rangle$, but the EOS at high pressure (>100 GPa) must be improved. The $\langle 110 \rangle$ orientation may obey a simple elastic perfectly plastic strength model; this is currently being investigated. Experiments (A to B) of $\langle 110 \rangle$ versus $\langle 100 \rangle$ orientation will greatly assist in our development of a diamond-strength model. As a result of these experiments, the $\langle 110 \rangle$ single-crystal diamond will be used in all future TARDIS experiments since the pullback features are greatly reduced.

Spherically Convergent Indirect-Drive Equation-of-State Measurements

Principal Investigator: A. E. Lazicki

Co-investigators: D. Swift, J. Hawreliak, F. Coppari, R. London, D. Erskine, D. Fratanduono, P. Celliers, J. Eggert, G. Collins, H. Whitley, J. Castor, J. Nilsen, and I. Otero

This FY15 campaign was designed to continue development of the spherically convergent drive platform on OMEGA using radiography to track the shock front in a spherical target. The eventual goal of this platform is to measure shock equation of state to the 100-Mbar range and to establish the Omega Laser Facility as a testing ground for platform concepts to be transferred to the NIF, where Gbar pressures are attainable. EOS is determined from radiographs that are recorded (1) on a framing camera to capture 2-D images from which density and sphericity of the converging shock can be measured; and (2) on a streak camera to capture the time-resolved shock trajectory from which shock velocity can be determined (Fig. 144.111). In this campaign the converging shock wave was launched using indirect drive in gas-filled hohlraums into solid balls of CH. He$_\alpha$ emission from V foils backlit the imploding CH spheres for both cameras. Both diagnostics returned data, and analysis is in progress to refine the design for a second development campaign, which will focus on optimizing radiographic contrast and collecting data over a longer duration.

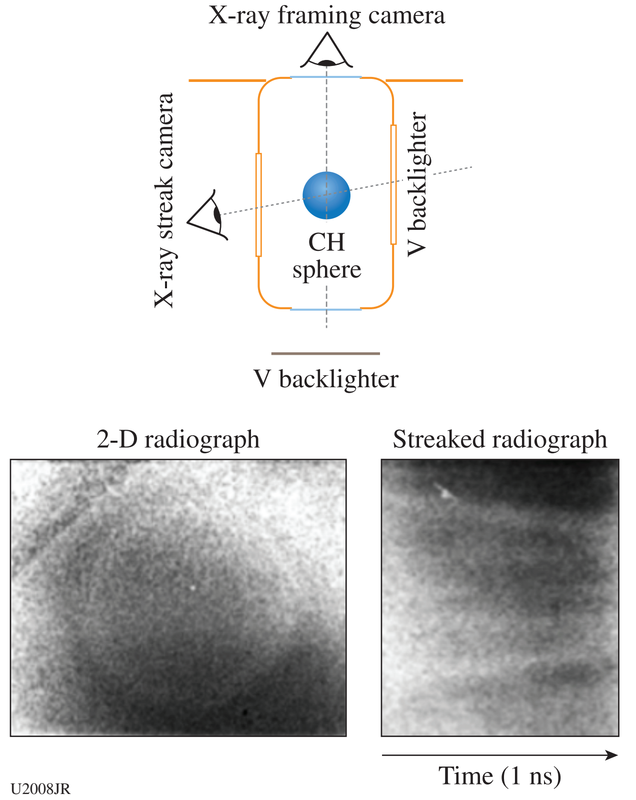

Figure 144.111
Experimental configuration and raw data from the two primary diagnostics (shot 78284).

Development of a Platform for Equation-of-State Measurements Using Flyer Plate Impact

Principal Investigator: F. Coppari

Co-investigators: D. Fratanduono, A. Lazicki, P. Celliers, and J. Eggert

The goal of this campaign was to develop a platform to accelerate diamond flyer plates to hyper-velocity for EOS measurements. The conceptual design was to ramp compress diamond through direct laser ablation and thereby accelerate the diamond into vacuum. After propagating a known distance, the diamond flyer would impact a transparent diamond window. By measuring the velocity of the diamond flyer plate prior to impact and the resulting shock velocity in the diamond witness, the principal Hugoniot of diamond can be determined *absolutely* (e.g., without needing a known pressure reference), enabling one to develop diamond as an EOS standard.

This campaign aimed to demonstrate this technique and provide EOS measurements in the 10- to 20-Mbar regimes. In addition, it tested the concept of applying a metal overcoat to the diamond flyer plate. The purpose of this design was to enable one to determine the metal Hugoniot once the diamond had been calibrated.

VISAR measurements made it possible to track the flyer velocity until the impact (occurring at ~11 ns in Fig. 144.112) and the shock velocity into the diamond window until breakout into the vacuum (~12 ns).

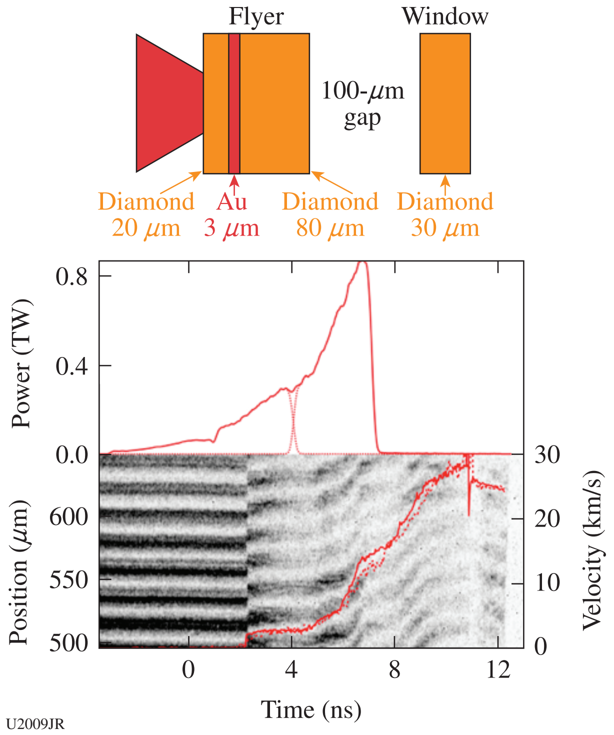

Figure 144.112
Schematic representation of the target assembly for these shots. The diamond flyer includes an Au layer as a preheat shield. The experiment used a composite pulse shape (stack of three laser pulses) with power increasing over 10 ns to gently accelerate the flyer. A typical VISAR trace and velocity profile are shown.

This campaign succeeded in accelerating the diamond samples through ramp compression (with and without the metal overcoat) to velocities in excess of 30 km/s. The shock velocities measured in the diamond window are consistent with previous datasets and correspond to pressures ~15 Mbar.

Development of a Platform for Extended X-Ray Absorption Fine Structure Measurements at the L3 Edge of High-Z Materials

Principal Investigator: F. Coppari
Co-investigator: Y. Ping

Extended x-ray absorption fine structure (EXAFS) measurements under dynamic ramp compression have been proven to be a valuable way of determining the temperature of ramp-compressed matter.[48] For high-*Z* materials, the absorption measurements must be performed using the L edge because the K edge would be at too high an energy. L-edge EXAFS measurements are challenging, however, because the cross section for the absorption event is lower than the K edge. To obtain good-quality data given current backlighter capabilities, multiple spectra must be averaged to improve the signal-to-noise ratio. In FY14, prior experiments deployed a multichannel crystal spectrometer for Ta L3-edge (10-keV) EXAFS that enabled us to simultaneously collect five EXAFS spectra in a single shot.[49] The FY15 campaign extended this technique to measure the EXAFS of Mo at the L3 edge (2.5 keV) to take advantage of the higher number of photons emitted by the capsule implosion backlighter at the lower photon energy. A new multichannel crystal spectrometer (Fig. 144.113) enabled us to simultaneously collect four spectra per shot and delivered high-quality EXAFS data of undriven Mo in two shots. Figure 144.114 shows the average over eight

Figure 144.113
Photograph showing the specifically designed multichannel crystal for the XRS Rowland spectrometer on OMEGA.

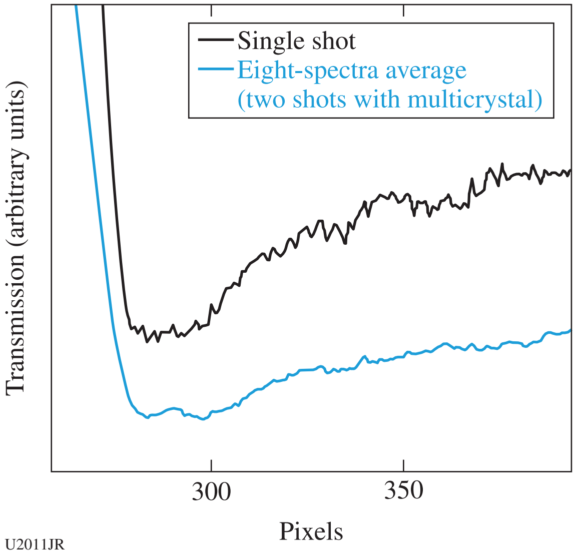

Figure 144.114
EXAFS spectra of undriven Mo: single shot (black line) and average over eight spectra (blue line) obtained in two shots using the multichannel crystal.

spectra. Data analysis will develop a framework for determining the material temperature from L3-edge EXAFS data.

3. Hydrodynamics

Mix-Width Measurements of Rayleigh–Taylor Bubbles in Opaque Foams

Principal Investigator: C. M. Huntington

A new (FY15) OMEGA campaign—foam bubbles—aims ultimately to measure the full interpenetration distance ("mix width") of bubbles and spikes in a Rayleigh–Taylor (RT) unstable system. A technique developed over many previous planar RT experiments is the use of a high-opacity tracer strip, often iodinated plastic, which is located in the center of the physics package and is density matched to the material around it. When imaged with transmission x-ray radiography, the tracer strip serves to highlight the central features, minimizing the effects of the walls that inevitably exist in shock-tube experiments. The tracer strip technique is excellent for providing contrast at the end of the RT spikes, where high-opacity plastic is surrounded by low-opacity foam, but it largely obscures the shape and extent of the low-density bubbles, which become mixed with and obscured by the doped tracer material. In contrast, the Foam Bubbles Campaign is developing an opaque *foam*, to be paired with a transparent plastic to highlight the extent of bubble penetration across the unstable interface. Ideally, one could use the contrast provided by the doped materials—plastic in one region and foam in another—to measure both bubble and spike length at a single interface, ensuring that the entire system experiences the same acceleration. This is done using the target shown in Fig. 144.115(a), which led to the radiograph seen in Fig. 144.115(b) for the case without an artificially perturbed interface. The image was generated using tilted, tapered point-projection x-ray imaging and clearly shows the layers on each side of the split target. The extent of bubble penetration in an RT-unstable system is a fundamental quantity, and this measurement furthers our understanding of hydrodynamic systems from ICF implosions to supernovae.

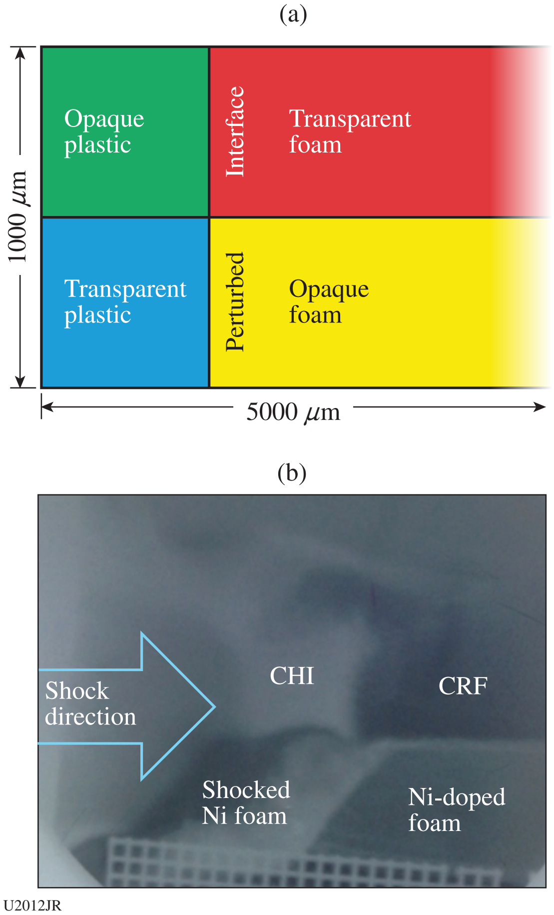

Figure 144.115
(a) Schematic of the target, showing the four regions of heavy/light and opaque/transparent materials. The system is driven from the left. (b) An example radiograph showing the four layers. The shock appears flat in the CHI and CRF but is distorted in the Ni-doped foam section.

Radiographic Techniques for Drive Symmetry

Principal Investigator: D. Martinez

Two half-days of hohlraum-driven radiography experiments were performed on the OMEGA Laser System in FY15. The primary objective was to investigate the evolution of a driven interface using point-projection x-ray radiography. For this campaign, the point backlighter was generated through a 20-μm pinhole along the "cranked" TIM-6 axis and recorded with a single-strip x-ray framing camera. The experiments were performed over two half-day campaigns to qualify the hohlraum drive, using VISAR for hohlraums on the H7 axis and using Dante for hohlraums on the H10 hohlraum axis. The FY15 experiments were successful, with 12 shots consisting of four VISAR shots, two Dante shots, and six radiography shots. Excellent data were recorded on all diagnostics and the experiments met the goals of the HED program.

4. Plasma Properties

Thermal-Conductivity Measurements of CH/Be by Refraction-Enhanced X-Ray Radiography

Principal Investigator: Y. Ping

Co-investigators: A. Fernandez, O. Landen, and G. W. Collins

This campaign employs differential heating[50] to generate a temperature gradient, and thermal conduction along that gradient is followed using the technique of time-resolved, refraction-enhanced x-ray radiography previously developed on OMEGA. The FY15 shot day obtained a total of 15 shots. The CH/Be target was heated from both sides by two groups of beams, reaching a temperature of ~10 eV, about twice as high as in previous campaigns. High-quality x-ray radiographs have been obtained (Fig. 144.116). Attention was also paid to measuring the background and flat field, which are both critical to normalizing the radiographs. It was found that the heating beams produced non-negligible background in the framing camera, even though they were fired outside the gate window and produced x rays at different energies from the backlighter. This provided an important correction in the refractive fringe contrast. The data will be used to benchmark thermal-conductivity models in the warm-dense-matter regime.

X-Ray Spectroscopy of Fully Characterized Non-LTE Gold Plasmas

Principal Investigator: R. F. Heeter
Co-investigators: G. V. Brown, J. A. Emig, M. E. Foord, D. Liedahl, C. A. Mauche, J. S. Ross, M. B. Schneider, A. Steele, and K. Widmann (LLNL); and D. H. Froula and J. Katz (LLE)

A more-precise understanding of the radiative properties of non-LTE gold is required to improve the fidelity of hohlraum x-ray drive simulations for NIF experiments for both ICF and HED applications. Expanding on prior work,[51] the FY15 Non-LTE Campaign studied x-ray emission from laser-heated, beryllium-tamped, gold–iron–vanadium foils. The campaign acquired data for four target types: (a) a "thicker" mixture of Au, Fe, and V; (b) a "thinner" mixture of Au, Fe, and V; (c) a mixture of Fe and V without Au; and (d) a "null" target with only the 10-μm Be tamper. Data obtained on 12 shots included simultaneous measurements of (1) time-resolved gold M-band spectra from 2 to 5.5 keV; (2) the plasma electron temperature via K-shell emission from helium-like V and Fe ions; and (3) the plasma density from time-resolved face-on and edge-on imaging of the sample's expansion from its initial size. For a few targets, an independent measurement of the electron temperature, using Thomson scattering in a transmission geometry, was obtained starting 0.3 ns after the spectroscopic data. Preliminary analysis indicates electron temperatures of 1200 eV were obtained in the FY15 shots, as on the FY14 series (Fig. 144.117). Ongoing detailed analysis is expected to lead to improved validation benchmarks for non-LTE models.

Magnetized Collisionless Shocks for Weapons Effects

Principal Investigator: B. B. Pollock
Co-investigators: H.-S. Park, J. S. Ross, C. Huntington, and G. Swadling

In FY15 this new campaign on OMEGA began an investigation of interpenetrating plasma flows in the presence of background magnetic fields. The first shot day employed the MIFEDS pulsed-power magnetic-field system to provide a background field along the direction of a low-density plasma plume produced inside the MIFEDS structure, into which a separate, orthogonal, high-density plume was driven after a variable delay. Figure 144.118 illustrates the experimental setup. The plasma interaction region was probed with both second-harmonic optical Thomson scattering and D–^{3}He proton deflectometry to measure the plasma density, temperature, flow

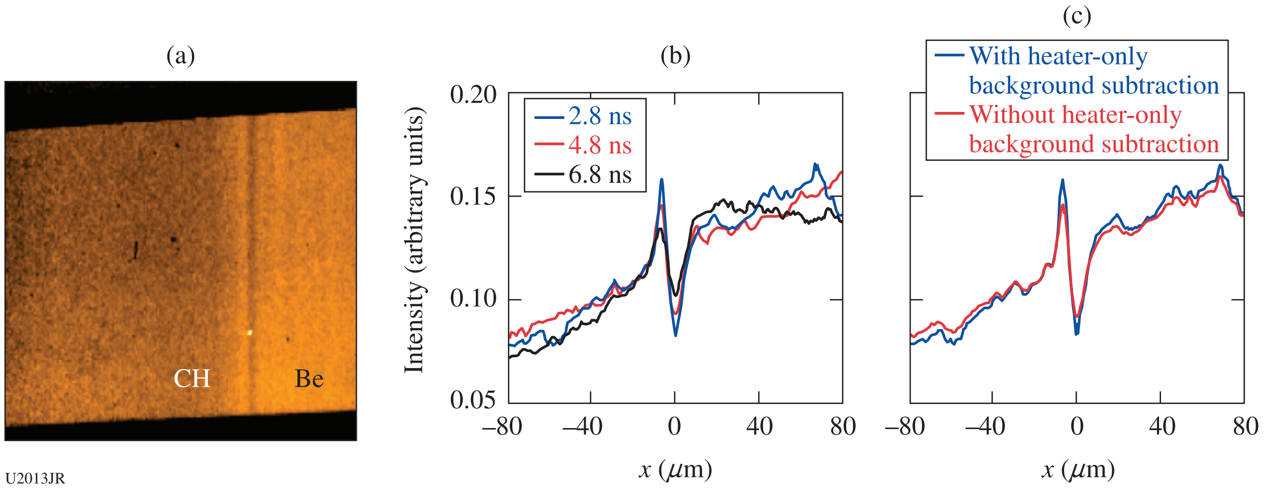

Figure 144.116
(a) X-ray radiograph of the CH/Be interface. The waves propagating away from the interface are also visible. (b) Lineouts of the x-ray radiographs at three delays. (c) Correction of the refractive fringe profile caused by background induced by the heating beams.

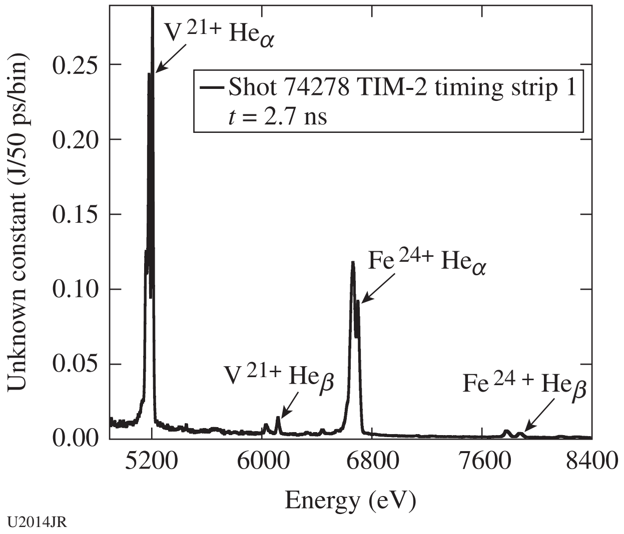

Figure 144.117
Spectrum measured by the MSPEC spectrometer of the x-ray emission from K-shell transitions in highly charged vanadium and iron. An electron temperature of 1200 eV is inferred from the various line ratios. Multiple shots in 2014 and 2015 delivered nearly identical data.

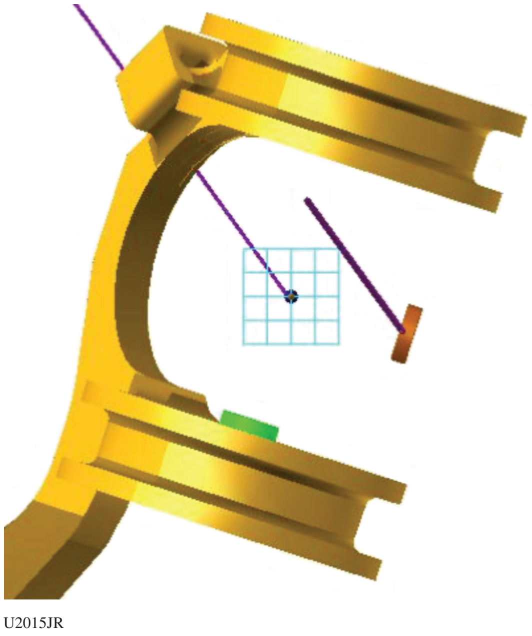

Figure 144.118
The MIFEDS used in this campaign. The green disk on the lower surface is illuminated by two to eight beams, producing one of the plasmas along the MIFEDS axis. The gold-colored disk on the right provides the orthogonal plasma plume. The Thomson-scattering volume is at the intersection of the surface normal for these disks. The blue grid shows the field of view for proton backlighting, using protons produced by imploding the D–^{3}He capsule positioned behind the grid.

velocity, and field structure. The second shot day increased the density and temperature of the plasma along the MIFEDS axis by incorporating additional drive laser beams; it also looked at head-on collisions from opposing flows along the MIFEDS axis (in addition to or separately from the orthogonal plume). The analysis of this recent experiment is ongoing and will inform the FY16 continuation of this effort.

Fusion Product Stopping-Power Measurements in Plasmas

Principal Investigator: J. Frenje (LLNL/MIT Collaboration)

The motivations for the one-day FY15 Plasma-Stopping Power Campaign on OMEGA were, first, to measure plasma-stopping power around the Bragg peak to validate different theories for varying plasma conditions (for the first time) and, second, to measure ion–electron (i–e) equilibration rates to experimentally validate the Coulomb logarithm for various plasma conditions (also for the first time in this regime). Observations and conclusions from these 12 shots are as follows: Charged-particle data obtained with the CPS1, CPS2, and WRF spectrometers clearly indicate that the plasma-stopping power around the Bragg peak varies with plasma conditions (Fig. 144.119). The data are well modeled by the Brown–Preston–Singleton (BPS) stopping-power formalism. X-ray streak camera and gated x-ray imaging data were also obtained, from which $n_e(t)$, $T_e(t)$ and $n_e(r,t)$, and $T_e(r,t)$ data will be inferred—essential for constraining plasma-stopping–power

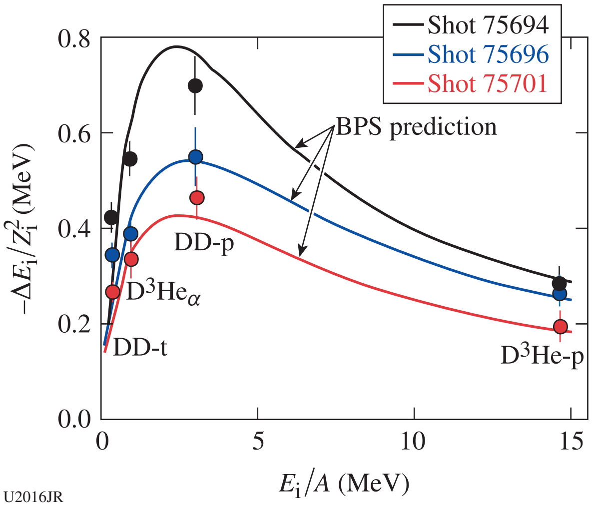

Figure 144.119
Plasma-stopping power around the Bragg peak for three different plasma conditions (three shots). The data are well modeled by the BPS plasma-stopping–power formalism.

modeling. A second framing camera imaged the shell location versus time; the 3MLARD neutron detector provided clean measurements of the secondary-neutron yield (hard x-ray levels insignificant as designed), which provide fuel ρR data also used to constrain the plasma-stopping–power modeling. The data quality should be good enough to validate the stopping power around the Bragg peak. The observations and conclusions resulted in an invitation to present these results at the 2015 APS–DPP Meeting. Figure 144.119 shows the stopping power for three different plasma conditions.

5. Material Dynamics and Strength

Copper Rayleigh–Taylor Growth

Principal Investigator: J. M. McNaney
Co-investigators: S. Prisbrey, H.-S. Park, C. M. Huntington, and C. E. Wehrenberg

The Copper Rayleigh–Taylor (CuRT) Campaign is part of the material strength effort aimed at assessing the strength of various metals at high pressure and high strain rate. The goal of the CuRT platform is to measure the Rayleigh–Taylor (RT) growth of samples that behave "classically," which is to say they can be fully modeled using a fluid description. In this series of experiments the intent is to measure RT growth in liquid copper at high pressure. An additional goal is to demonstrate the dynamic range of the technique by measuring RT growth in solid copper.

Without the stabilization of strength, classical RT growth is characterized by a growth rate $\gamma = \sqrt{kg\,\mathrm{A}_n}$, where k is the wavelength of the unstable mode, g is the acceleration, and the Atwood number A_n quantifies the density jump at the interface. Acceleration of the sample in the experiment is provided by the stagnation of a releasing shocked plastic "reservoir," which is directly driven by 1 to 2 kJ of laser energy, depending on the desired material condition. The growth of preimposed ripples is recorded using transmission x-ray radiography from a copper He_α slit source, where the opacity of the sample is calibrated to the ripple amplitude. The pre-shot metrology and measured ρr of the driven sample together yield the growth factor, which is compared to models of RT growth. Diagnostic features allow for same-shot, *in-situ* measurements of the modulation transfer function (gold knife edge on sample) and the opacity look-up table (copper step filters on the imager), resulting in error bars of roughly ±10%.

Three shot days on OMEGA EP were fielded in FY15, first to develop the drive conditions necessary to produce both liquid and solid copper and then to produce two sets of RT measurements. In the first set of RT measurements, post-shot simulations indicated that the copper sample was in a mixed solid–liquid state. Initial data for solid copper were obtained in a second set of RT measurements. Analysis of these Q4 shots has just begun, but an example of the experimental data is shown in Fig. 144.120. There is contrast from both the driven (center) and undriven (edges) regions.

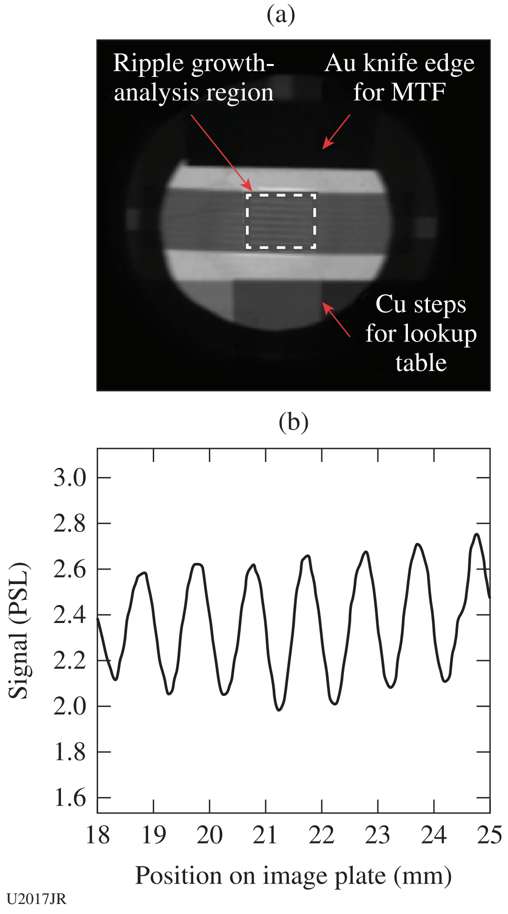

Figure 144.120
(a) The radiograph from OMEGA EP shot 21025 and (b) a plot of a lineout taken from the middle of the white box.

Measurements of **In-Situ** *Strain in Shock-Compressed Single-Crystal Tantalum*

Principal Investigator: C. E. Wehrenberg

The primary goal of this OMEGA EP campaign was to record a time series of diffraction patterns for single-crystal Ta, shock compressed along the [001] direction at 0.5 Mbar. One UV beam drove a CH/Ta/MgO crystal package with a

3-ns pulse and a 2-mm phase plate, while a 100-ps IR pulse was used to drive the Zn backlighter. Driven diffraction signals were successfully recorded for three different backlighter delays, spaced 0.4 ns apart. In addition two drive shots were performed to confirm the repeatability of the 0.5-Mbar drive. One secondary goal for this shot day was to develop transmission Bragg diffraction on OMEGA EP. To this end, two shots were performed—a background shot and a transmission shot—using OMEGA EP's other two beams, and these will be used as a guide in the design of future transmission Bragg experiments. Figure 144.121 presents lineouts from the diffraction data, showing a consistent strain measurement for different timings of 0.5-Mbar shock-loading experiments.

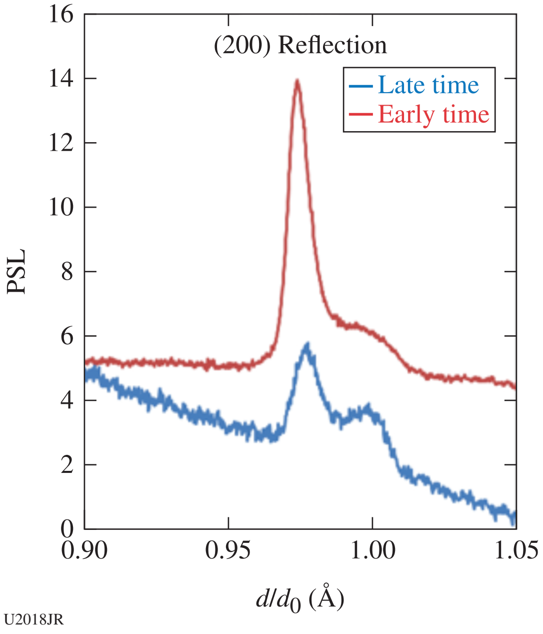

Figure 144.121
Lineouts from reflection diffraction data plotted as a ratio of driven d spacing over ambient d spacing d/d_0 for two 0.5-Mbar experiments.

Understanding the Basic Plasticity Mechanism in Shock-Compressed Tantalum
Principal Investigator: C. E. Wehrenberg

One OMEGA EP shot day was dedicated to the first campaign seeking to detect plasticity via twinning in shock-compressed Ta. Since twinning produces a reorientation of the lattice in a known manner, twinning would produce a change in texture spots on the diffraction ring. This study used vapor-deposited Ta samples with a sharp (110) fiber texture, so that any change in texture would produce a marked contrast in diffraction patterns. To observe this change in texture, the TwinDiff Campaign used high-energy powder diffraction (16-keV Zr backlighter) to successfully record the entire Debye ring. A new target mounting system was developed and successfully tested in which samples can be mounted at a 30° angle while performing simultaneous VISAR measurements using a folding mirror. A total of ten shots were performed with shock pressures in the 0.5- to 2.0-Mbar range. While the lower conversion efficiency of the high-energy backlighter limited the signal-to-noise ratio of the driven signal, it is now possible to track the pattern of the texture spots on the Debye ring to specific texture orientations—in this case (110) fiber texture (Fig. 144.122).

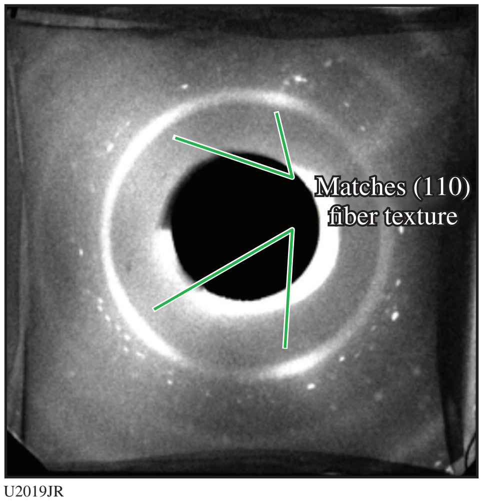

Figure 144.122
Diffraction pattern from (110) fiber-textured Ta during 0.5-Mbar shock compression.

6. X-Ray Source Development and Application

Optimizing X-Ray Emission from Nanostructured Copper Foams
Principal Investigator: K. B. Fournier

The FY15 nanostructure shot day was the culmination of a series of experiments with ultralow-density foams that had increasing concentrations of metal dopants. The FY15 shots fielded, for the first time, a pure-metal foam that had a density low enough to allow supersonic laser propagation, which resulted in heating nearly the entire target volume to high temperatures (Fig. 144.123). The purpose of the ongoing nanostructure campaigns is to maximize the yield and tune the x-ray output from high-temperature plasmas using different metallic emitter ions. Maximization of the x-ray yield is

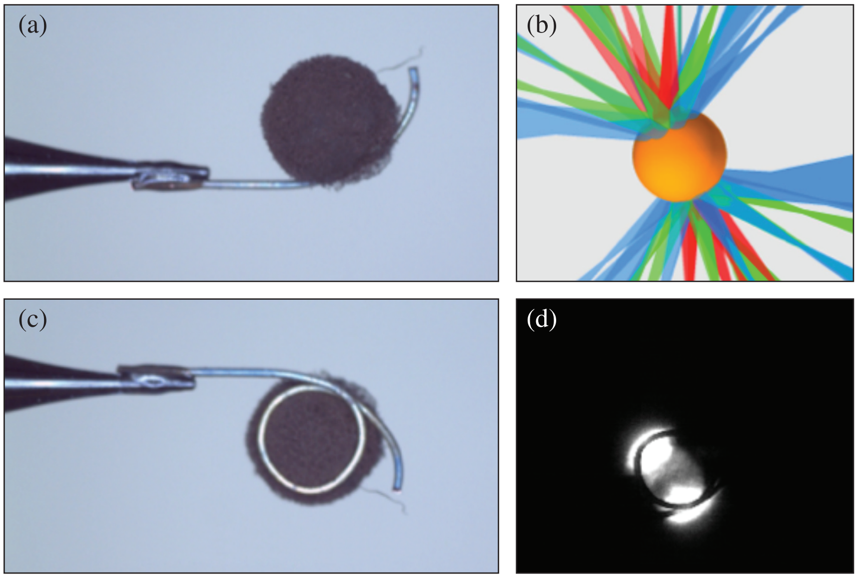

Figure 144.123
[(a) and (c)] Photographs of a 14-mg/cm^3 copper foam target mounted for OMEGA shots. (b) Nominal OMEGA laser beam pointing at the opposing hemispheres of the foam targets. (d) An x-ray pinhole camera in the light of Cu K-shell x-ray emission showing the two heated faces of the target, and the shadow of the mounting wire used to produce the target.

achieved by suspending the emitting ions in an ultralow-density foam matrix, made of either silica aerogel or carbon nanotubes. When the electron density in the aggregate foam material is in the range of 10% to 20% of the critical electron density for the laser light ($n_c \sim 10^{22}$ cm^{-3} in the case of 351-nm laser light), the entire volume of the target is heated supersonically to multi-keV temperatures. The resulting volume of high-temperature plasma emits K-shell x rays from mid-Z dopant ions (Ti, V, Fe, Ni, Cu, Ge). The foam targets developed in the past have had target densities in the range of 3 to 10 mg/cm^3 and metallic ion concentrations in the range of 3% to 20% (Refs. 52–56). For the FY15 shots, however, targets became available that were 100% Cu (Z = 29) with densities in the range of 14 to 25 mg/cm^3. While these densities were somewhat too high to have strongly supersonic laser propagation, they were still low enough to achieve nearly full-volume heating of the target. The resulting laser-to-x-ray conversion efficiency in the range of the K-shell x rays from Cu^{27+} and Cu^{28+} (8 to 10 keV) is ~2%, which is a significant enhancement compared to 0.8% for emission in the same x-ray energy range from a solid copper disk under the same laser-drive conditions. The next steps in this campaign are to achieve even lower foam densities, for better laser coupling and more-efficient x-ray production, and to fabricate foams for NIF-scale experiments.

X-Ray Source Fluence as a Function of Viewing Angle

Principal Investigator: M. A. Barrios

The National Security View (NSView) OMEGA Campaigns study target fluence as a function of viewing angle for x-ray source applications. Our goal is to improve the current understanding of the fluence delivered to material samples and other test objects using these or similar targets as x-ray sources. A previous campaign in FY14 measured the x-ray emission of stainless-steel (SS)–lined cavities using three different beam axes (H5–H16, P2–P11, and H7–H14) resulting in view angles of 0°, 42°, and 79° for Dante and 5°, 46°, and 75° for DMX spectrometers. The two FY15 campaigns continued this work, using the same beam axes to study the x-ray fluence of Fe-aerogel targets having different heat-propagation properties than SS-lined cavities. In the second campaign, both SS and Fe-aerogel targets were also studied at intermediate angles (37° and 71° for Dante and 37° and 66° for DMX) by using P5–P8 and H6–H15 beam axes.

Figure 144.124 shows representative time-integrated spectra for (a) SS-lined cavities and (b) Fe-aerogel targets. Data from the FY15 campaigns are consistent with findings from FY14, showing little variation in the observed x-ray emission from Fe K shell, consistent with a volumetric emitter that is optically thin and independent of viewing angle. A larger variation in the Fe K shell is observed for the aerogel targets compared to the SS targets, likely a result of small variations in foam density and microstructure. Larger variations in the x-ray fluence as a function of view angle are observed for sub-2-keV x rays. Figures 144.125 and 144.126 show target total x-ray yield as a function of view angle, compiling data from all campaigns to date, for SS-lined cavities and Fe-aerogel targets, respectively. As shown in Fig. 144.124, the total x-ray yield is dominated by sub-2-keV emission corresponding to the Fe L shell; therefore, the measured total yield is a good indicator of the sub-2-keV target behavior. The SS cavity data

(Fig. 144.125) shows a sharp decrease in measured yield below ~30°, not observed in the aerogel targets (Fig. 144.126). The behavior of the Fe-aerogel targets is consistent with a volumetric emitter, once geometric and optical-depth corrections are considered. Such is not the case for the SS-lined cavities, which are best described by a surface emitter, with the emission originating from the cavity inner walls and laser entrance hole. A spectral reconstruction model was developed to match observations for the SS-lined cavities (shown in Fig. 144.125 as the dashed purple and dotted blue lines). For comparison we show a model fit that accounts for only geometric corrections (shown as the black solid curve). Future work will focus on further development of models to best describe the measured behavior for both types of targets.

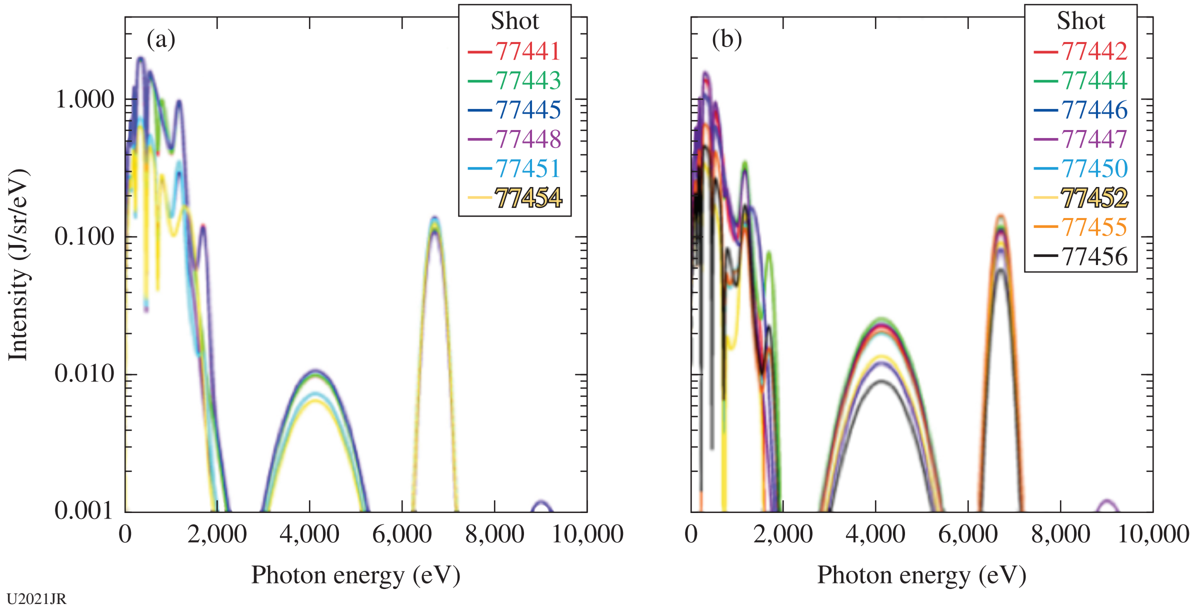

Figure 144.124
Measured Dante time-integrated spectra for (a) stainless-steel–lined targets and (b) Fe-aerogel targets from the second FY15 campaign.

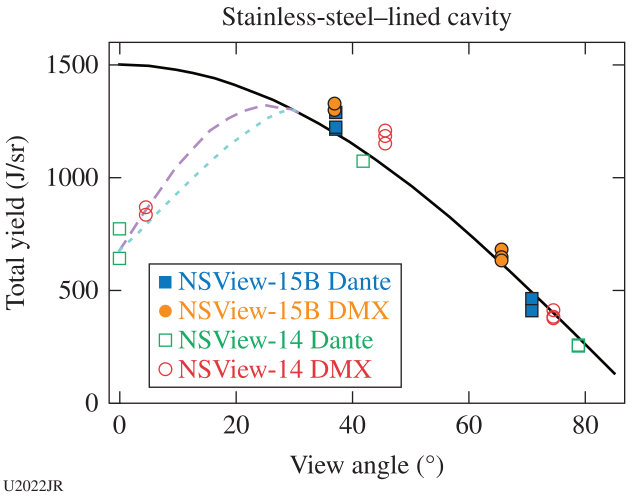

Figure 144.125
Total x-ray yield for stainless-steel–lined cavity targets as measured using Dante and DMX spectrometers.

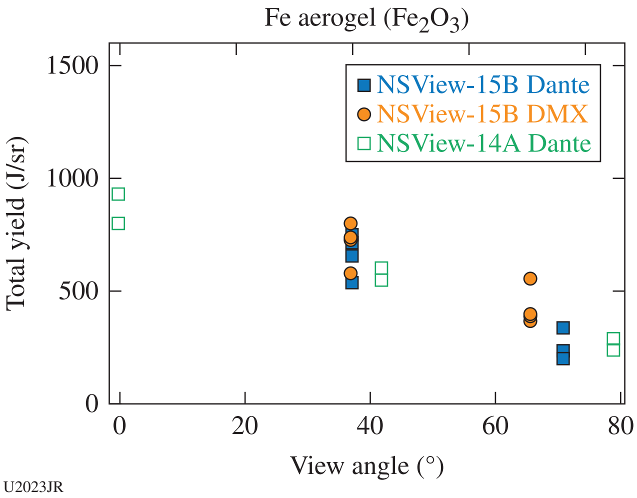

Figure 144.126
Total x-ray yield for Fe-aerogel targets as measured using Dante and DMX spectrometers.

Solar-Cell Electrostatic Discharge Experiments

Principal Investigator: K. Widmann

The overall goal of the SolarCellESD Campaign is the development of a large-area, solar-cell–array, cold x-ray exposure test platform that can be used to test the response of in-flight solar cells to a simulated nuclear weapons threat environment. In the two SolarCellESD Campaigns in FY15, a new x-ray source was developed and tested. The x-ray source was a high-temperature gold halfraum, 600 μm in length and 600 μm in diameter, which included a small pinhole in the closed end of the halfraum to limit the total flux emitted by the source without altering the spectral content. Figure 144.127 shows a sketch of the halfraum target with the view angles for Dante, which was used to characterize the obtained x-ray radiant power and spectral intensity emitted by the halfraum target, and for one of the two x-ray Langmuir probe detectors (XLPD's) specifically designed for the SolarCellESD effort. The XLPD's contain four Langmuir probes and an array of two solar cells. The first XLPD had a view of the pinhole and, therefore, was exposed to the cold x rays, while the second XLPD had a view of the hohlraum wall and was illuminated mainly by hard x rays. Initial results from both the Langmuir probes and the solar cells on both XLPD's revealed that sustained arcing was observed and, moreover, that for the low-flux conditions, the discharge was quenched within a few microseconds of the onset of the discharge.

ACKNOWLEDGMENT

This work was performed under the auspices of the U.S. Department of Energy by Lawrence Livermore National Laboratory under Contract DE-AC52-07NA27344.

FY15 LANL Experimental Campaigns at the Omega Laser Facility

Los Alamos National Laboratory (LANL) conducted a total of 258 target shots on the OMEGA Facility in FY15 (58 for ICF and 200 for the HED programs). A summary of these experiments is contained in this section.

Shear

The LANL Shear Campaign is examining instability growth and its transition to turbulence relevant to mix in inertial confinement fusion (ICF) capsules using experimental platforms with antisymmetric flows about a shear interface to examine Kelvin–Helmholtz (KH) instability growth. The platform consists of a directly driven shock-tube target with an internal physics package consisting of two hemi-cylindrical foams separated by a layer of tracer material (Fig. 144.128). Gold plugs are situated on opposing ends of the foams to limit shock propagation from the direct drive to only one end of the foam; this sets up a pair of pressure-balanced counter-propagating shocks about the tracer layer. Measurements of the tracer-layer (shear interface) mixing dynamics are used to benchmark the LANL Besnard–Harlow–Rauenzhan (BHR) turbulence model. The mixing dynamics are characterized by measuring the

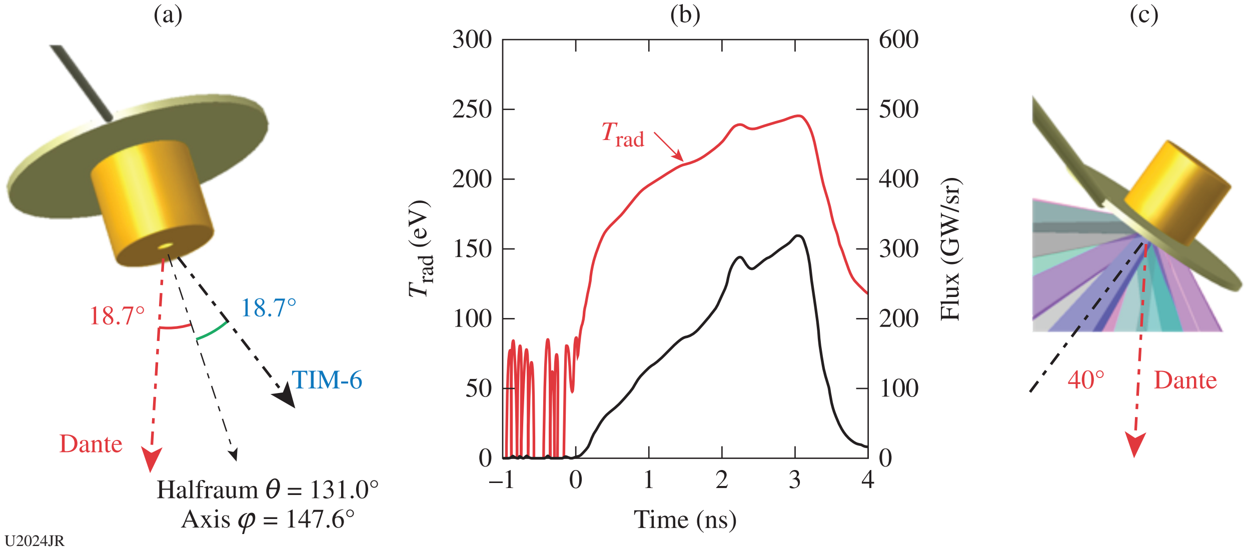

Figure 144.127
(a) Sketch of the gold halfraum target with the view angles for Dante and TIM-6 used for one of the x-ray Langmuir probe detectors. (b) Dante measurements from a halfraum target that was positioned such that Dante had a view of the "open" side of the halfraum. (c) The 1-ns beams were stacked in time to provide x-ray emission with ~3-ns duration.

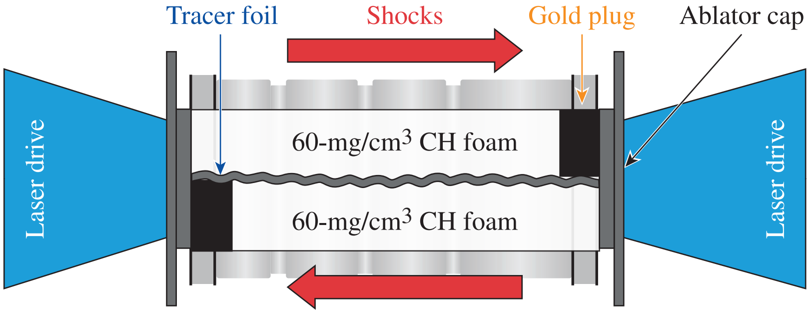

Figure 144.128
Illustration of the Shear experimental platform on OMEGA.

mix width of the layer as well as examining multidimensional structure growth along the layer surface.

The FY15 Shear Campaign continued an effort to examine the model's initial condition parameter space by varying the characteristics of the target's tracer layer. In December 2014 the Shear Campaign completed a set of experiments varying the tracer-layer surface roughness as an avenue for varying the instability seed scale lengths in the system. Increased surface roughness was shown to effectively advance the mixing evolution of the experiment for Al tracer layers. In June 2015 the Shear Campaign began an instability mode-growth study using sinusoidal tracer layers (Fig. 144.128) of various wavelengths, as opposed to the nominally flat foils used to seed multimode instability growth in all previous Shear experiments. Experiments with 50-μm- and 100-μm-wavelength foils already show significant qualitative differences in structure formation as the system evolves. Mode-growth studies are to be completed in FY16.

Marble

In MARBLE-15B, capsules filled with nominally 40 or 70 mg/cm^3 of partially deuterated foam ($CD_{0.5}H_{0.5}$) and 5 or 10 atm of tritium (T_2) were imploded to measure the scaling of neutron yield with these two parameters. Improvements in target fabrication resulted in 19 capsules, formed from two joined hemispheres, that held gas versus only one for MARBLE-15A. Some capsules did show thickness nonuniformity, and it is believed this is what caused a displacement of the center of the imploded core image relative to that of the ablation surface. Using data from the capsules with low displacement, DT yield was found to scale as predicted, and yields were about 30% of 1-D simulations (see Fig. 144.129). As expected, neutron yield was seen to increase with lower foam density and higher tritium fill.

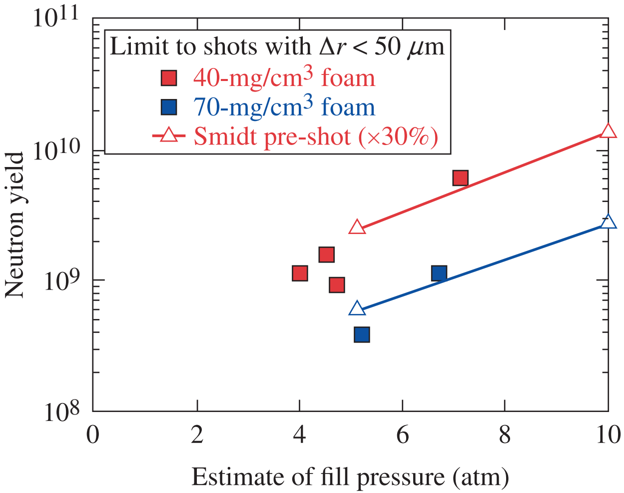

Figure 144.129
DT neutron yield from General Atomics MARBLE-15B capsules, limited to implosions showing low displacement (Δr) of the imploded core relative to that of the ablation surface. This limited dataset shows the expected trend with fill pressure and foam density, and yields are ~30% of that expected from simulations.

In the August Marble experiment (15C), to provide premixed C, D, and T atoms, the Y_{DD}:Y_{DT} ratio was obtained for capsules filled with CD_4 and T_2 gases. The simplest comparison of the experimental ratios to expectation follows from the assumption of a single ion temperature. The relative error of the data with respect to this theory is plotted in Fig. 144.130. The data obtained in August are plotted with blue circles. A few preliminary data points obtained in March (red ×'s) and ratios from 1-D simulation (green asterisks) are also included in the plot. In contrast to simulation and a large fraction of March data, all the August data fall below the predicted values. Because the constituent fills at shot time directly influence the yield ratio (and there is significant CD_4 leakage during T_2 filling), the few unused August targets are now being analyzed by LLE to determine remaining CD_4. These composition determinations will provide a direct comparison to the estimates based on the half-life measurements.

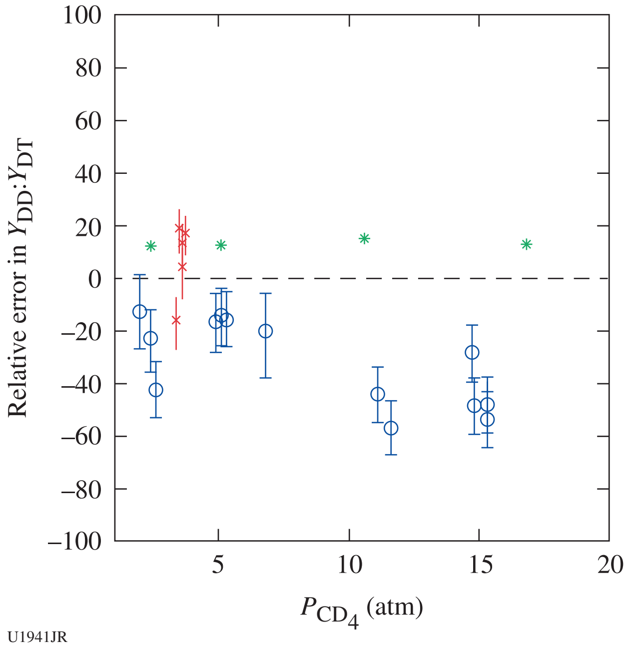

Figure 144.130
Relative error in the measured Y_{DD}:Y_{DT} ratio from the calculated ratio under the assumption of single ion temperature. Data obtained in August are plotted with blue circles. Also included in the plot are the few preliminary data points obtained in March (red ×'s) and ratios from 1-D simulation (green asterisks).

MixEOS

In FY15, the LANL MixEOS Campaign fielded its first shot day on OMEGA EP to develop a new platform for examining the equation-of-state (EOS) characteristics of mixed materials under high-energy-density (HED) conditions. The platform is intended to provide measurements against which to compare the accuracy of several different EOS table mixture rules, such as Dalton and Amagat. Benchmarking these mixture rules provides information on the accuracy of simulations of multicomponent regions present in HED and ICF systems. Highly accurate experimental data exist for some gas mixtures up to a few Mbar (Ref. 57), but experimental data are sparse for higher-pressure systems with initially solid metal mixtures, where the various mixture rule predictions show increasingly larger disagreement.

The MixEOS experiments featured two target types for comparison using an initially solid NiAl alloy for a test mixed material, as well as Al and quartz witness materials. The first target type used a thin CH-ablator (30-μm) design with a thick layer (~100 to 200 μm) of test material. The thick material was theorized to have the advantage of increasing measurement accuracy by increasing the amount of material through which the shock propagates before measurement, but instead it introduced significant oscillations in the system's post-shock pressure. A second target type used a thick CH ablator (250 μm) with a thin test-material layer (50 μm). The thick ablator layer was designed to increase the measurement accuracy by eliminating pressure oscillations but required a thinner corresponding test-material layer to reach the desired pressures with the same available laser energy. The steady-shock target also has the advantage of simplifying the corresponding model. A first look at the VISAR measurements of the steady-shock (thick-ablator) targets shows that the experiment was able to capture not only the breakout times for the test materials, but it also showed little fringe movement (change in shock velocity) from the shock propagation in the quartz. This suggests that the shocks are steady over the course of the experiment. Target improvements already underway for FY16 will increase the measurement accuracy by increasing the signal from the quartz witness as well as mitigating the shock-front curvature in the diagnostic field of view.

IonSepMMI

The scientific objective of IonSepMMI-15A is to obtain the first direct measurement of interspecies ion separation (a yield-degradation mechanism) in a collisional, compression-yield–dominated ICF implosion (60-beam, symmetric direct drive). Detailed post-shot analysis has just begun, but if successful, these measurements would complement and augment the yield-based inferences of interspecies ion separation by R. D. Petrasso's group at MIT and H. Herrmann *et al.* at LANL. With guidance from the first-principles theory, the targets for IonSepMMI-15A were designed to maximize interspecies diffusion by (1) reaching a high ion temperature (which enhances temperature-gradient–driven thermo-diffusion) and (2) using two ion species, D and Ar, of large mass difference (which enhances the thermo-diffusion coefficients). In addition, our data will be used to help validate a new multi-ion-species plasma-transport and viscosity model that has been implemented into LANL's *xRAGE* code. Conversely, *xRAGE* was used for pre-shot simulations and is being used for post-shot analysis and data interpretation (in addition to *HYDRA*, which does not have a multi-ion-species transport model).

Measurements for IonSepMMI-15A focused on x-ray spectroscopy (XRS and SSCA) and spectrally resolved x-ray images (MMI). We will perform advanced analysis of this dataset (building on methods pioneered by R. Mancini's group at the University of Nevada, Reno) to infer the spatial profiles of the argon/deuterium concentration. If the latter quantity develops a nonuniform spatial profile or a different value than the initial argon concentration during the implosion, either of these results would constitute smoking-gun proof of interspecies ion diffusion. The primary shot-day objectives of obtaining analyzable x-ray spectroscopy data showing both H-like and He-like argon emission in different target types were achieved. Preliminary examples of partially processed SSCA and MMI data are shown in Figs. 144.131 and 144.132, respectively, for a target with a 13-μm CH shell, 5-atm of D_2 fill, 1% Ar by atom fraction, and 21.2-kJ laser energy. Final scientific conclusions await ongoing analysis. The results will also provide valuable feedback for potential follow-on IonSepMMI Campaigns resuming in FY17.

Coax

Understanding how ionizing x-ray radiation interacts with an underdense medium is critical to our overall understanding of radiation transport. As radiation flows through a medium, the intensity of the radiation is modified in the medium through absorption, scattering, and emission as described by the radiative-transfer equation.[58] Applications of the radiative transfer equation are commonly found in laboratory-based high-energy-density-physics experiments[59–68] as well as many astrophysics phenomena such as supernova explosions.[69,70] In the laboratory, radiation transport relevant to astrophysics and inertial confinement fusion can be studied using high-powered laser facilities. In laser-driven radiation-transport experiments, a high-*Z* foil (typically gold) is irradiated to convert UV laser light into x rays that drive the transport experiment. The x-ray converter is typically fielded as a planar foil or a cylindrical can that is irradiated on its interior (a hohlraum[71]). In these experiments a low-density foam target is used as the medium for the transport. These types of transport experiments are integrated experiments that combine the fundamental physics of radiation transport (and, subsequently, material opacity[72,73] and equation of state) with a complex x-ray source.

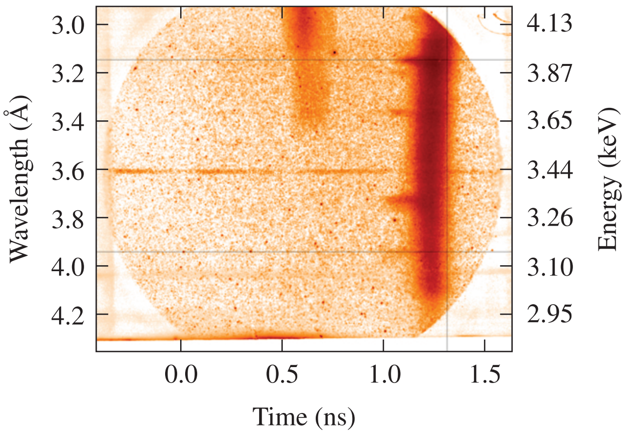

U1942JR

Figure 144.131
SSCA data (TIM-1, shot 78197) showing multiple Ar emission lines. Note that the time axis needs further analysis; absolute time values as shown here should not be trusted to better than ~150 ps. Data were processed by S. Hsu.

High-quality measurements in these types of experiments are essential for understanding radiation transport. The National Ignition Facility (NIF) provides an opportunity to push from transport-dominated to diffusion regimes for radiation-transport experiments. Previous work has demonstrated the technique of diagnosing self-emission of the ionization front in experiments that use the high x-ray fluxes available at the NIF. This previous work has shown discrepancies between simulation predictions and experimental results.[74,75] This report focuses on extending the aforementioned absorption spectroscopy techniques to conditions relevant to the NIF[74] by using methodologies developed on the OMEGA[76] laser. Previous experiments used absorption spectroscopy in which chlorinated doped foams measured the heat wave in the

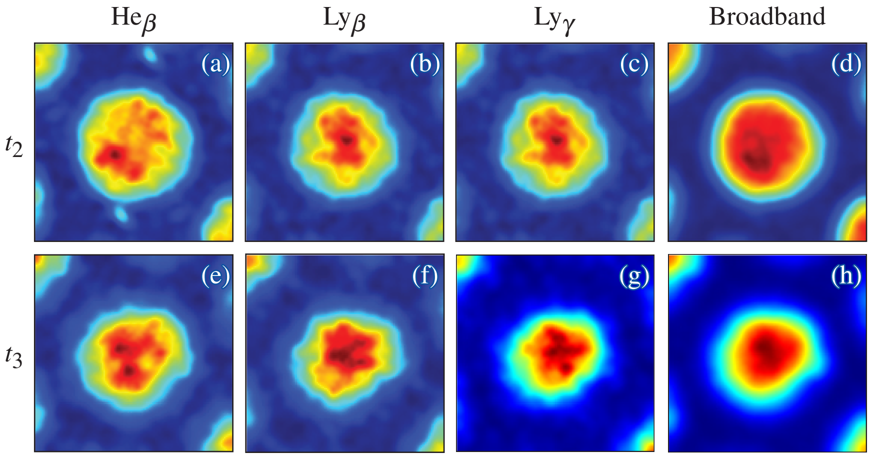

U1943JR

Figure 144.132
Multiple-monochromatic-imager (MMI) data (XRFC1, TIM-3, shot 78197) showing Ar He_β (column 1), Ly_β (column 2), Ly_γ (column 3), and broadband (column 4) images for $t_2 \approx 1.18$ ns (row 1) and $t_3 \approx 1.32$ ns (row 2). Data were processed by P. Hakel.

supersonic regime.[67,68,77,78] However, the sensitivity of the absorption-spectroscopy measurement depends on the relationship between the ionization of the tracer and the tracer's temperature. Figure 144.133 shows the mean charge of the Cl tracer used in the 50-mg/cm^3 $C_9H_3O_2Cl_5$ foams used by Hoarty *et al*.[68] (blue) and the Ti tracer used in the 80-mg/cm^3 $TiSi_5O_{12}$ foams (red) that will be discussed here as simulated by the atomic physics code *PrismSpect*.[79] The gradient of these plots is directly related to the sensitivity of the temperature measurement. For the Cl simulation, the mean charge shows a steep inflection at a material temperature of 125 eV, indicating that absorption spectroscopy of the Cl tracer would drop significantly in its sensitivity at temperatures greater than 125 eV. These temperatures are well below those expected in radiation-transport experiments on the NIF. The Ti simulation shows an inflection around 300 eV, indicating that switching to a Ti tracer would allow one to measure absorption spectroscopy up to 300 eV.

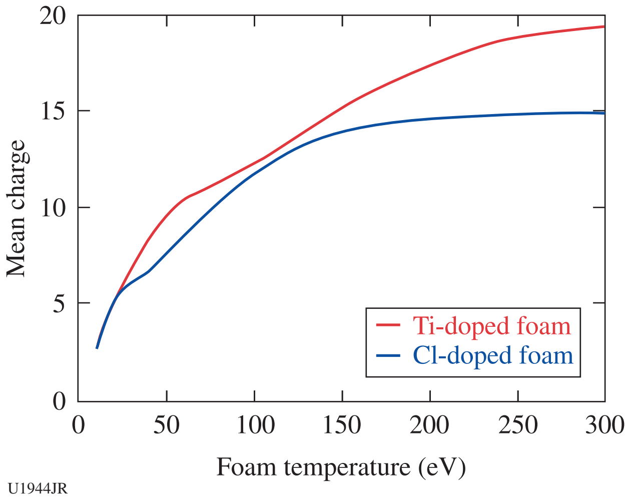

Figure 144.133
PrismSPECT[78] simulations showing the mean charge of the Cl (blue) and Ti (red) tracers plotted against the temperature of the foam in which they are embedded. The Cl simulation uses a 50-mg/cm^3 $C_9H_3O_2Cl_5$ foam, while the Ti uses an 80-mg/cm^3 $TiSi_5O_{12}$ foam. The inflection of the Cl data at 125 eV indicates that the sensitivity of the tracer as an absorption-spectroscopy dopant will drop significantly for temperatures greater than 125 eV. Similarly, the Ti trend shows this transition occurring at around 300 eV, making it a more suitable tracer for the material temperatures anticipated on the NIF.

One of the key advancements that makes this work possible is the improvement that has occurred in target fabrication, characterization, and assembly. Previous experiments used titanium foils as a tracer but, because of the density and absorption of radiation, the tracer was not in pressure balance with the surrounding foam and was likely not in thermodynamic equilibrium. For these experiments, a titanium-doped SiO_2 foam at a ratio of ~1:5 is generated. The foam is machined down to an ~800-μm-diam, 1000-μm-long cylinder. A cylindrical socket is then milled into a pure-SiO_2 foam that is ~1500 μm long × 1600 μm in diameter. The Ti-doped foam is then inserted into the socket. This technique can eventually provide some spatial resolution of the material's temperature. In this case, it allows the Ti-doped region to be at the same temperature to minimize line-of-sight effects. The radiograph of such a target in Fig. 144.134 shows the regions of the Ti-doped SiO_2 and the undoped region around them. The foams are inserted into a beryllium sleeve to support them and then attached to the top of a hohlraum to serve as the x-ray drive for the radiation wave.

The experimental setup provides two independent and complimentary techniques to diagnose the impact of the radiation on the physics package. Figure 144.134 also shows a schematic of the experimental setup. A low-density foam physics package is attached to a half-hohlraum that is driven by 20 beams on the OMEGA laser delivering 10 kJ of UV laser light into the hohlraum with a 1-ns-long square pulse shape. This configuration yields a characteristic peak hohlraum temperature of ~220 eV. The foam package on the end of the hohlraum is orthogonally diagnosed with two point-projection backlighters: one for x-ray radiography and the other for absorption spectroscopy.

The imaging axis uses a 6-μm-thick vanadium backlighter mounted to a 6-mm-sq tantalum substrate with a 20-μm pinhole aligned to the center of the V foil. The V foil is driven by five overlapping UV beams with a 1-mm-diam spot size producing an ~4.95-keV point x-ray source. The pinhole is located 14 mm from the center of the foam physics package. The attenuated x rays are measured directly on D3 x-ray film with 40-mil-thick Be and 0.5-mil-thick Al filters positioned for an ~21× magnification. An additional 1-mil-thick Al filter is mounted to the target along the undriven side of the hohlraum, extending 200 μm above the end of the hohlraum to block thermal radiation from the interior of the hohlraum from reaching the x-ray film. The backlighter foil uses a 1-ns square drive pulse, so the imaging x-ray radiographs are time integrated over the entire length of the pulse. The late-time hydrodynamics of the system evolve slowly enough that the improved photon statistics are preferable to switching to a time-gated x-ray framing camera.

The absorption-spectroscopy axis is nearly orthogonal to the imaging axis (90.3°). It also uses a point-projection x-ray source as the backlighter for the measurement. Unlike the

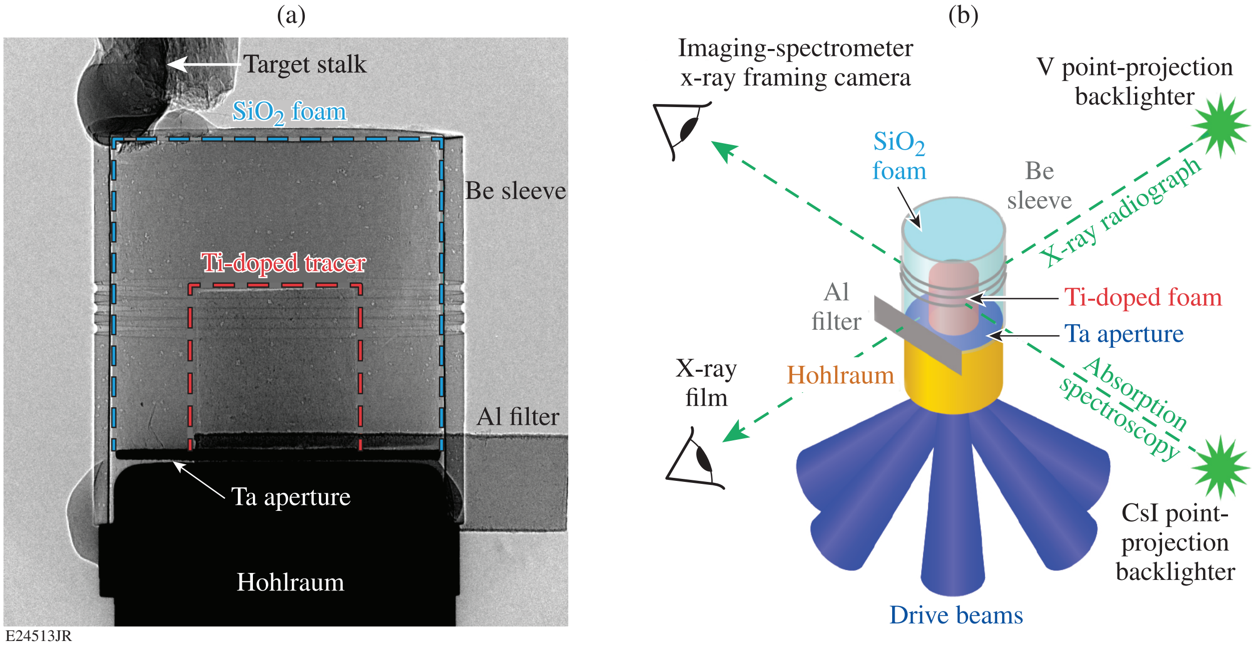

Figure 144.134
(a) A broadband x-ray radiograph of an undriven target. The target consists of a Ti-doped tracer foam coaxially inserted into an SiO_2 foam and mounted to the end of a hohlraum. The physics package is encased in a Be sleeve with three machined fiducial grooves. The Ta aperture, hohlraum, Al filter, and target stalk are also shown. (b) The experimental configuration. A hohlraum is driven from one side with 20 UV laser beams and the x rays leaving the opposite side irradiate the physics package.

quasi-monoenergetic backlighter used for the imaging axis, we required the absorption-spectroscopy backlighter to be as broadband as possible over the spectral regime where we expect absorption features to appear (4.4 to 5.1 keV). CsI has previously been demonstrated as a good candidate because of the large number of transition lines present in this spectral range.[66,80] Unlike the K_α emission of the V backlighter, the CsI emission in the 4.5- to 5.4-keV range does not penetrate the CsI substrate, significantly complicating a backlighter design that uses a foil mounted to a pinhole substrate. Instead, the CsI x-ray point source is generated by driving the end of a 200-μm-diam boron fiber that has been coated with a 12-μm-thick layer of CsI. The tip of the wire is irradiated with four overlapping UV beams focused to a 300-μm-diam spot. The tip of the CsI wire is located 12.5 mm from the center of the foam. The attenuated x-ray spectrum is measured using the NIF-5 spectrometer,[66] a cylindrically curved Ge [111] crystal mounted to the front end of an x-ray framing camera,[81–83] and a time-gated x-ray detector. For this configuration, the target magnification is ~50×. The spectral data are detected on a two-strip microchannel plate using a 500-ps pulse-forming network (PFM) that has an effective temporal integration of ~300 ps for an individual absorption feature. The camera is filtered with 21 mil of Be to protect the crystal from debris.

As discussed above, a titanium tracer is used in the foam to provide spectral-absorption features that determine characteristic material temperatures from 50 to 200 eV—the typical range that we expect in laser-driven radiation-transport experiments on OMEGA. In this range, Ti absorption features for 1*s*–2*p* (4.5 to 4.8 keV) and 1*s*–3*p* (5.0 to 5.4 keV) transitions appear and disappear as the ionization of the Ti dopant changes. Figure 144.135 shows the simulated absorption features that appear in an 85-mg/cm^3 $TiSi_5O_{12}$ heated tracer foam. By spatially and temporally resolving these absorption features, the temperature of the tracer foam can be inferred.

The method for determining temperature from the absorption-spectroscopy features can be seen by the simulated absorption spectrum shown in Fig. 144.130. The temperature of the foam tracer can be inferred to ±10 eV for temperatures in the 90- to 200-eV range simply by measuring the turn-on and turn-off times of the different absorption features. The analysis can be further improved by subtracting a spatially resolved CsI spectrum without absorption features to correct for systematic intensity drops on the microchannel plate (MCP) and the overall spectral response of the diagnostic. This technique will leave some residual high-frequency artifacts that can easily be removed using a low-pass fast Fourier transform (FFT)

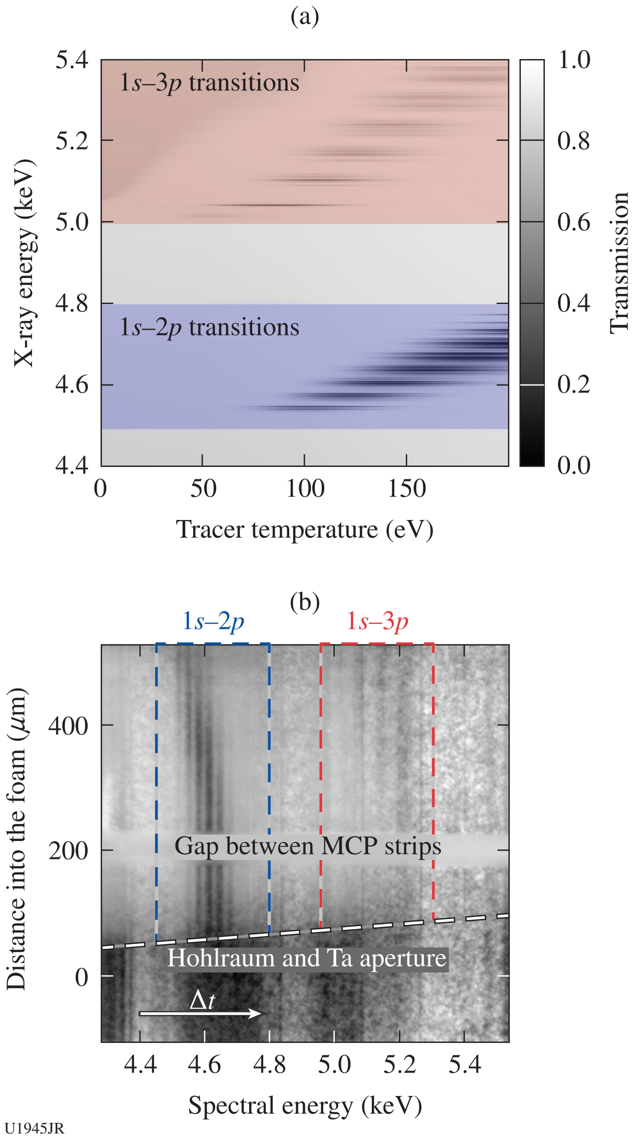

Figure 144.135
(a) Predicted absorption features from *PrismSPECT* for an 85-mg/cm^3 $TiSi_5O_{12}$ foam are shown. The absorption features show 1*s*–2*p* (blue) and 1*s*–3*p* (red) transition-absorption features that have been used to characterize material temperatures from 50 to 200 eV. (b) The measured absorption spectrum from an 85.3-mg/cm^3 $TiSi_5O_{12}$ tracer coaxially inserted into a 74.4-mg/cm^3 SiO_2 foam is shown.

filter. Figure 144.135 shows the post-processed absorption-spectroscopy data for an 86.3±0.6-mg/cm^3 Ti-doped tracer foam coaxially inserted into a 74.4±0.3-mg/cm^3 SiO_2 foam beginning at 1.45 ns after the hohlraum drive begins. The data were taken on a two-strip MCP streaking from left to right spanning 1.45 to 1.7 ns. The bottom of the image is blocked by the hohlraum and Ta aperture, which expands into the foam. The transmission time along the strip of the MCP is 250 ps, so the 2*p* and 3*p* lines are detected at different times. For foam temperatures greater than 90 eV, the 2*p* lines are sufficient to constrain the temperature independent of the significantly dimmer 3*p* lines, so they are used independently to infer the temperature with a significantly reduced temporal integration. In this case the 2*p* lines are detected at 1.51±0.15 ns, where the temporal uncertainty is dominated by the width of the PFM.

Figure 144.136 shows the inferred temperature measurements from the data in Fig. 144.135. To infer the temperature, the absorption-spectroscopy data are cropped into 20-μm spatially integrated lineouts. A 20-μm integration window was chosen based on temperature-gradient predictions from post-shot simulations along with rough estimates from the raw data. The lineouts are then correlated with the simulated lineouts at different material temperatures. The green circles show the temperature inferred by the best fit to the absorption data. The uncertainty on the temperature measurement is dominated by the propagation of the uncertainty in the relative transmission of different absorption features in the processed data. The uncertainty in the transmission depends on the difference in the bulk opacity between the data and the background subtraction and the statistical shot-to-shot variations of the x-ray framing camera. The transmission uncertainty is propagated to a temperature uncertainty by adjusting the relative transmissions of the different valleys in the spectrum by ±10% in a manner that would result in the maximum absolute change in the best-fit

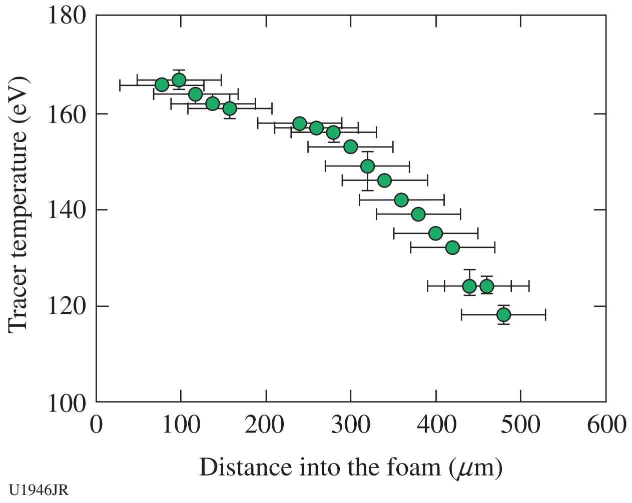

Figure 144.136
The inferred temperature profile from the absorption-spectroscopy data described in Fig. 144.135. The green circles show the temperature inferred by the best fit to the data using the relative transmission of the different absorption features.

temperature (i.e., some peaks would increase in transmission by 10% while others would decrease). Contributions from the uncertainty in the foam density were found to be negligible for these experiments. For temperatures in the 90- to 200-eV range, the error bars typically fall within ±2 eV or better, while for 50 to 90 eV, the uncertainty increases up to ±10 eV largely because of the poor contrast of the 1*s*–3*p* absorption features.

We have shown a novel new technique for orthogonally diagnosing radiation-transport platforms using absorption spectroscopy and x-ray radiography to characterize the transport medium—in this case a low-density SiO_2 foam. A titanium-doped SiO_2 foam was coaxially inserted into the center of an SiO_2 foam to introduce a titanium tracer for producing absorption-spectroscopy features for material temperatures ranging from 50 to 200 eV. This technique was shown to constrain the temperature of the tracer to ±2 eV for temperatures greater than 90 eV. The foam and tracer were orthogonally diagnosed using point-projection x-ray radiography to provide useful information on the total energy deposition into the foam along with verification of the minimal impact of the tracer on the overall radiation hydrodynamics of the experiment. Short-term future experiments will use geometric constraints to modify the anisotropy of the radiation source observed by the foam to provide some insight into the inherent anisotropy of the radiation emitted by the hohlraum. This platform will also be used to investigate the mean effect of radiation transport through an inhomogeneous medium. Long-term plans will bring the platform to the NIF to extend the length of the supersonic transport in the foam to further study potential discrepancies between radiation transport through uniform and inhomogeneous media.

Neutron-Imaging System Multiview

Neutron imaging in 2015 conducted a set of experiments at the Omega Laser Facility to develop techniques for advanced imaging of ICF implosions. Simultaneous neutron and x-ray imaging along the same line of sight enables one to directly compare these images, which provide different information about the plasma characteristics. This technique was first demonstrated at Omega in 2014 and was further explored this year.[84] Generalized expectation-maximization (GEM) algorithms have also been developed to extract 3-D (volumetric) neutron-emission information from a small number of views.[85] Only one neutron-imaging system is currently available for use at each laser facility, so this algorithm was tested using D–D implosions at Omega. The laser-drive symmetry was varied to produce asymmetric implosions, and these sources were imaged using the facility x-ray cameras and then reconstructed, as shown in Fig. 144.137.

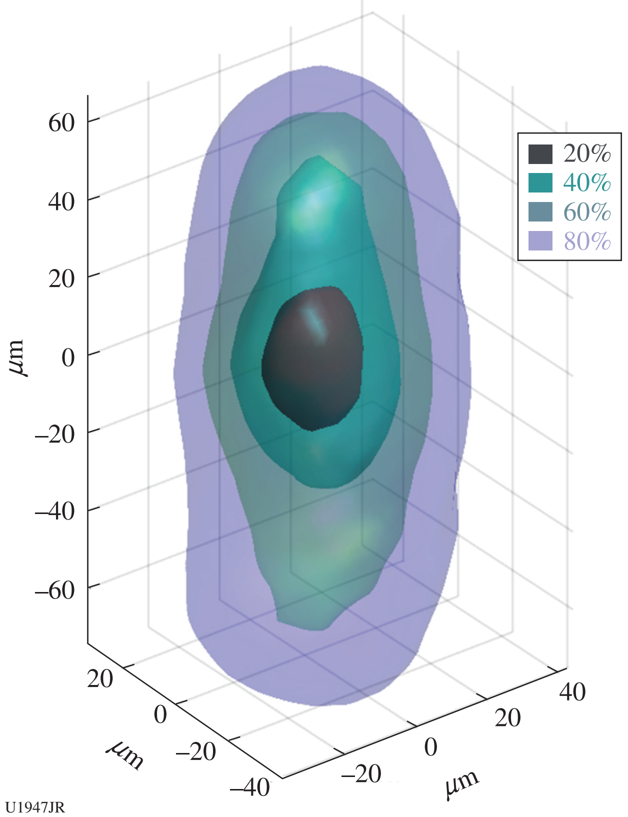

Figure 144.137
Reconstructed 3-D x-ray image from an OMEGA implosion.

HEDMMI

Simulations have predicted that the glue used to mount nominal OMEGA implosions causes a premature blowout of the fuel cavity.[86] The resulting deficiency in the pressure profile could explain a large fraction of yield degradation with respect to idealized (1-D) calculations. Additional simulations have shown that this mounting-induced asymmetry of the fuel cavity can be imaged by using titanium dopant on the inside of the ablator, coupled with narrowband imaging. In FY15 we used the multiple monochromatic imager to spectrally resolve gated images from shell-doped implosions. Based on the modulation in limb emission, our data support the contention that in nominal implosions the mounting creates a preferred axis on which stagnation is perturbed. However, the final emission pattern oriented along this axis varied markedly between the two campaign days. Furthermore, in contrast to expectation from simulations, targets with glue footprints ranging from 40 to 120 μm in diameter showed indistinguishable yield performance.

Figures 144.138(a)–144.138(c) show gated (40-ps) narrowband emission in the titanium He_β line for three different shots; Fig. 144.138(d) provides a summary of integrated signal versus angle for each image. The acquisitions occur during deceleration and are inferred to be prior to peak neutron production. For the experiment corresponding to Fig. 144.138(a), the mounting pointed toward the top of the image. The brightening of the emission from the mount side and the loss of signal opposite are qualitatively in agreement with simulated images. In the mount-inclusive simulations, the brightening of the limb occurs because of the inward collapse of the ablator. On the opposite side of the implosion, a localized pressure increase blows out a section of shell and consequently the emission is reduced. In Fig. 144.138(d), the integrated signal as a function of angle for the image of Fig.144.138(a) is plotted in solid black (0° corresponding to image top, counterclockwise orientation). All shots of that campaign day (February 2015) revealed a similar pattern. Figure 144.138(b) shows a typical image from August 2015 for which the mount again points upward in the view [red dashed line in Fig. 144.138(d)]. During this shot day, signal minimum appeared toward the mount; the signal maximum opposite. On the same August 2015 shot day a target was also inserted from a port 180° opposite. The image acquired from this "flipped" implosion, for which the mounting is oriented toward the bottom of the view, is shown in Fig. 144.138(c) [signal versus angle summary, blue dashed–dotted curve in Fig. 144.138(d)]. All the images show emission maximum or minimum and general outer contour ellipticity oriented along the 0° to 180° axis, coinciding with the mounting. The reversal in mounting direction within the same shot day, however, resulted in a noticeable reduction in modulation and pattern broadening. The imaging data indicate a complex coupling between mounting and other systematic asymmetry. Further considering the yield data and the motivating simulations (which indicated large yield reduction) suggests that, within our range of parameter exploration, these complex interactions result in a saturated but important reduction of nuclear performance.

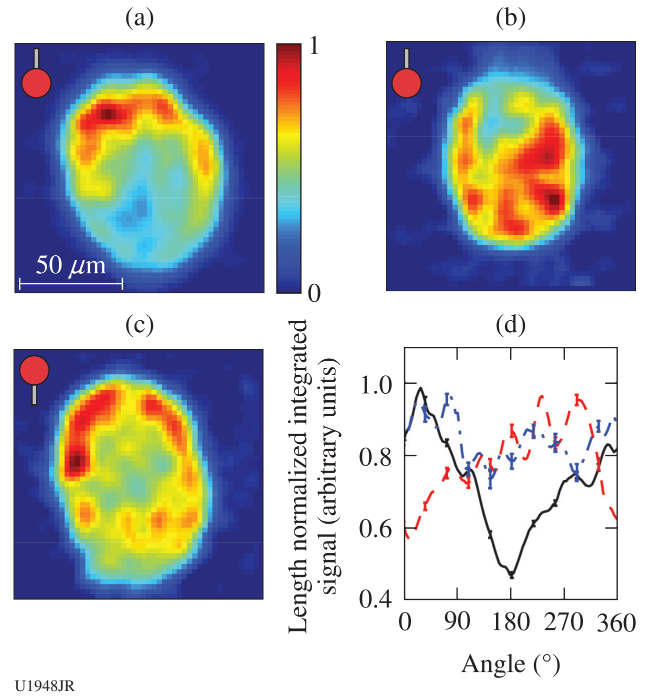

Figure 144.138
Image in He$_\beta$ emission for (a) shot 76266 (February 2015), (b) shot 78497 (August 2015), and (c) shot 78505 (August 2015). The insets indicate mounting orientation. (d) Signal integrated from center to periphery and normalized by length (shot 76266, solid black line; shot 78497, dashed red line; shot 78505, blue dashed–dotted line).

Kinetic Plasma Effects

The goal of KPE-15A was to test a new interspecies ion diffusion theory[87,88] by imploding glass capsules filled with hydro-equivalent mixtures of DT, DT^{3}He, and DTH. The ternary mixtures provide hydro-equivalency in which particle pressure and Atwood number are preserved and also allow one to measure nuclear yield ratio (e.g., D–D over D–T or T–T over D–T yield). In the DT^{3}He capsule, the theory suggests gradient-driven diffusion forces ^{3}He toward the hot core and DT toward the cooler edge. As a result, reduced D–T yield relative to a homogenous mixture is expected, which is consistent with the previous D–T–^{3}He implosions on OMEGA.[89] The primary goal of KPE-15A was to test the hypothesis that the DTH fill would result in an enhanced D–T yield over homogenous predictions as H is driven outward and DT diffuses toward the hot core.

Filling glass capsules with three types of fuel mixtures was challenging. KPE-15A targets were one of the very first capsules that LLNL Target Fabrication delivered to LLE for OMEGA shots. Out of the 12 symmetric direct-drive shots that were completed, 11 shots performed well with less than 25% yield variation from prediction. The observed D–T yield for each capsule was compared with the fusion reaction yield formula

$$Y_{\mathrm{DT}} \sim N_{\mathrm{D}} N_{\mathrm{T}} \left\langle \sigma v \left(T_{\mathrm{i}}\right) \right\rangle \tau \big/ V,$$

where Y_{DT} is the predicted D–T neutron yield, N_{D} is the number of D atoms, N_{T} is the number of T atoms, $\langle \sigma v(T_{\mathrm{i}}) \rangle$ is the averaged reactivity as a function of ion temperature T_{i} [measured by the neutron time-of flight (nTOF) detector], τ is the burn duration (measured by the neutron temporal diagnostic), and V is the burn volume (measured by x-ray images). Figure 144.139 shows observed D–T yield divided by Y_{DT} for each type of capsule. Comparing DT^{3}He and DT capsules, yield reduction of ~0.68× was observed when ^{3}He was added to DT fuel, which confirms the previously reported anomalous yield reduction in D^{3}He (Ref. 90) and DT^{3}He (Ref. 89). In the case of DTH capsules, an ~1.24× increase in D–T yield relative to expectation was observed, consistent with the interspecies ion-diffusion theory.

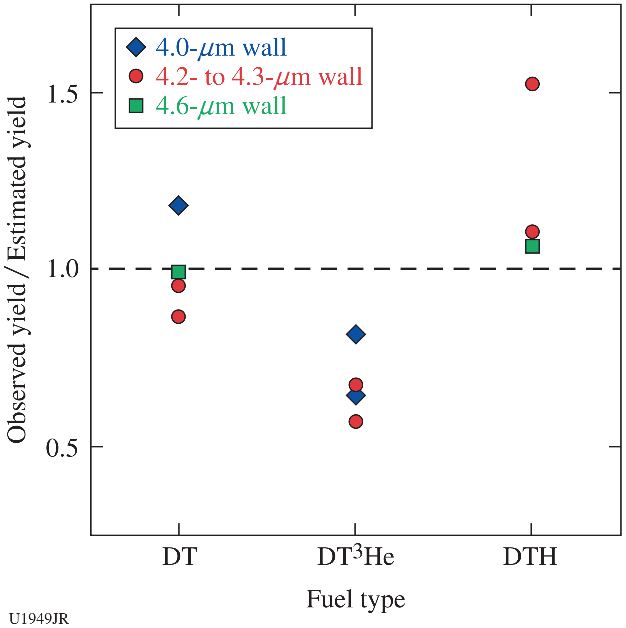

Figure 144.139
Observed D–T yields compared with the estimated yield according to fusion-reaction formula. The result shows yield reduction in DT^{3}He and yield increase in DTH. Both results are consistent with the interspecies ion-diffusion theory.

ObliShock

The mixing of modes between the Rayleigh–Taylor (RT) and Kelvin–Helmholtz (KH) instabilities occurs all across nature, from our terrestrial atmosphere and oceans[91] to astrophysical systems like accretion disks and supernovae.[92] This mixing is the reason for the growth of mushroom-like caps on RT and Richtmeyer–Meshkov (RM) processes[93] and can lead to a quicker onset of turbulence.[94] Rarely is a flow interface purely shear or purely buoyancy driven, or in the case of ICF, driven by passing shocks (RM) or convergence (Bell–Plesset) or shearing shock flows (KH), but a mixture of all. The Oblique Shock Platform developed by LANL in collaboration with the University of Michigan aims to understand the interplay between the various instabilities to determine the growth rates of each of the constituent parts on the whole.

The first campaign used a simple sine wave of 100-μm spacing and a 5-μm amplitude as the seed; a second campaign used a two-mode perturbation following the equation

$$y(\mu\text{m}) = 10(\mu\text{m}) \cdot \cos\left[\frac{2\pi x}{100(\mu\text{m})}\right] - 5(\mu\text{m}) \cdot \cos\left[\frac{2\pi x}{50(\mu\text{m})}\right],$$

$$0 < x < 900\ \mu\text{m},$$

as the seed. Both seeded surfaces were designed to be struck by a shock at a 30° angle with respect to the shock tube [see Fig. 144.140(a)]. As the shock passes the interface between an iodinated CH tracer layer and pushed into a 100-mg/cm^3 foam, it is imaged using the OMEGA EP SCI (see figure caption for details). The tracer layer is subject to several forces: shock acceleration, deceleration in the foam, and shear flow across the layer, which cause a dynamic feedback into the growth of the spikes and bubble seeded into the experiment.

Using LANL's multiphysics *RAGE* code, we have been modeling the data from our two FY15 campaigns. Results

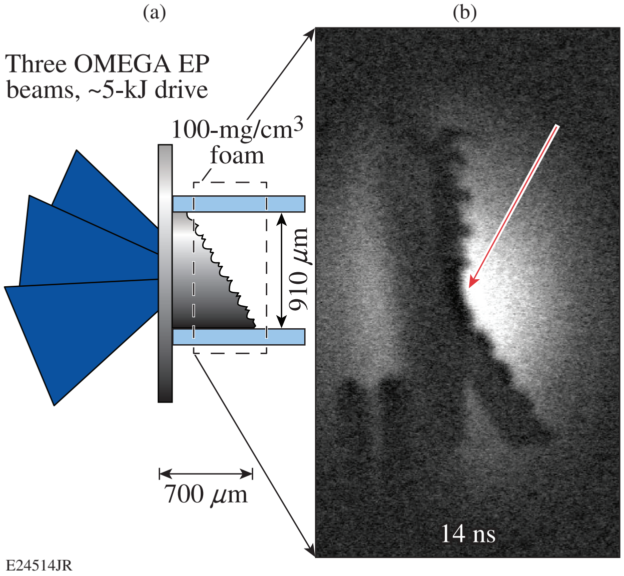

Figure 144.140
Setup of the OMEGA EP experiment. (a) Three long-pulse 3ω beams of ~5 kJ each irradiate the polyimidamide (PIA) ablator and launch a shock into the experiment. A thin (100-μm) layer of density-matched iodinated CH inserted into the PIA is used as a tracer layer for the perturbed interface inside a thin CH tube. The tracer layer expands into a 100-mg/cm^3 foam. (b) The spherical crystal imager (SCI) was used with an 8-keV copper K$_\alpha$ source driven by the fourth beam as a short-pule (10-ps) backlighter to image the layer. The area imaged by the SCI is indicated by the black dashed box [shown in (a)]. The red arrow points to the position of the shock (moving from left to right) at the CHI/foam boundary.

are shown in comparison to the experimental data at 21 ns from the two-mode campaign in Fig. 144.141. The simulation shows similar growth of the layer and the characteristic turnover of the spikes caused by the shear across the layer. *RAGE* [Fig. 144.141(b)] shows significantly more roll-up than the experiment, but the experiment is not well enough resolved to make out such small structures, but clearly exhibits the same roll-up feature, which was expected. *RAGE* also reproduces the complicated chevron-like shock structure behind the tracer layer, a feature that was not expected to be seen in the experiment but was caused by better-than-expected contrast from the instrument. The agreement is surprising considering the code used a simple mass source as a pusher for the hydrodynamics, which is unphysical at late time since the laser turns off at 10 ns and a rarefaction wave starts to enter the experiment, where in the code, the source is on for the full simulation. Work is currently ongoing to assess the growth rate of the spikes and bubbles in comparison with the codes and to add a laser driver to the *RAGE* calculations for a more-realistic shock source.

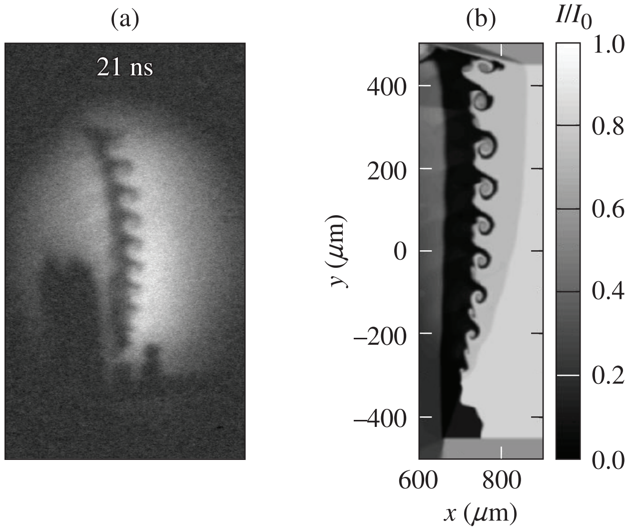

Figure 144.141
Images of (a) the two-mode experiment at 21 ns and (b) a *RAGE* simulation.

ACKNOWLEDGMENT

This work was supported by the LANL ICF Program (S. Batha, Program Manager) and conducted as part of the Kinetic/Plasma Effects (KPE) Project (H. Herrmann, Project Leader).

FY15 SNL Program

Sandia National Laboratories (SNL) conducted 17 target shots on OMEGA EP for the MagLIFEP experiment. SNL also participated in the MagLIF experiment on the OMEGA laser in FY15.

MagLIFEP

The MagLIFEP Campaign in FY15 aimed to characterize the laser heating of underdense, magnetized plasmas (D_2, Ar) at parameters relevant to the MagLIF ICF scheme being pursued at Sandia National Laboratories.[95,96] Simulations indicate that if 6 to 8 kJ of laser energy can be coupled into an ~10-mm-long underdense DT plasma, MagLIF targets at Z may achieve D–T fusion yields of ~100 kJ. This laser energy must be coupled to the gas while minimizing laser–plasma instability growth. By systematically investigating laser and target parameters, the MagLIFEP Campaign aims to determine the parameter space in which laser heating is efficient and predictable. Figure 144.142 shows the MagLIFEP experimental configuration. In each experiment a single long-pulse OMEGA EP beam (4 ns long, 0.35 μm, 3.1 kJ, $I \sim 2.3 \times 10^{14}$ W/cm^2) is fired through a laser entrance hole foil and down the axis of a D_2-gas–filled tube. As the laser heats the gas and propagates down the tube in a "bleaching wave," the plasma emission is observed with an x-ray framing camera (XRFC) that images emission from a 0.3% Ar dopant added to the gas as shown in Fig.144.143. In the experiments the beam parameters were kept constant and the gas density changed so that the electron density (n_e) was 5.5%, 7.7%, and 10% of the critical density (n_c) for the 351-nm beam. A 5-T uniform axial magnetic field was also applied using MIFEDS coils that surround the target, and the impact of this field on the propagation was assessed.

XRFC images from two of the magnetized shots with n_e = 0.077 n_c and 0.1-n_c gas fills are shown in Fig. 144.143. The

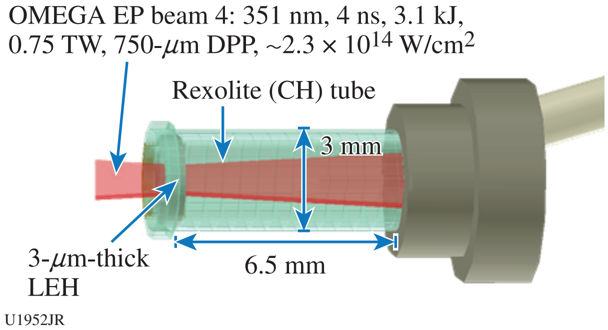

Figure 144.142
Experimental setup for the MagLIFEP Campaign as viewed by the x-ray framing camera (XRFC). MIFEDS coils used to magnetize some of the targets are not shown. DPP: distributed phase plate; LEH: laser entrance hole.

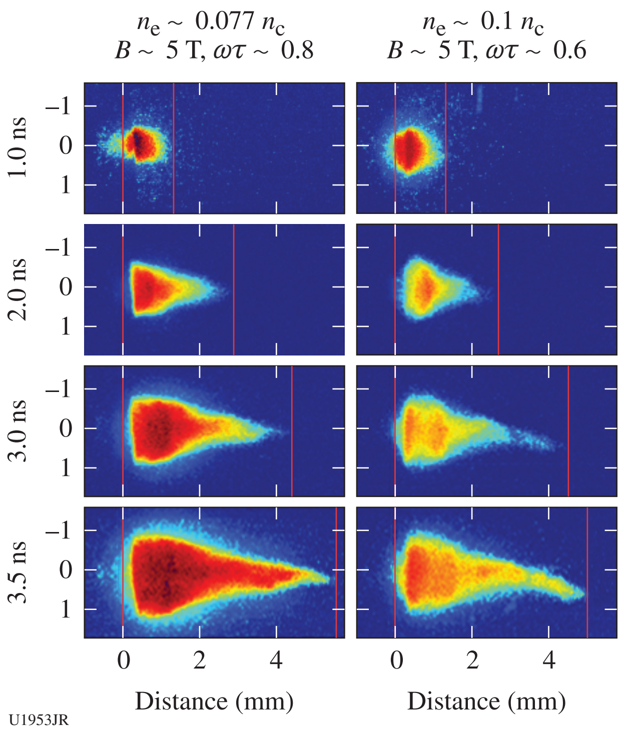

Figure 144.143
XRFC images from magnetized D_2-gas–filled targets with $n_e = 0.077$ and $0.1\ n_c$ taken at the times indicated.

images show the emission from plasma formed as the laser propagates from left to right down the tube. As the density increases from $0.077\ n_c$ to $0.1\ n_c$, more structure appears in the emission at late times and the propagation appears to bend. We are exploring the mechanisms that could result in such behavior including filamentation and whole-beam self-focusing driven by the plasma hydrodynamic response to the laser heating. This is accompanied with an increase in hard x rays for $0.1\ n_c$, which suggests more laser–plasma instability (LPI) is occurring, most likely stimulated Raman scattering (SRS) in the underdense plasma. Given the complicated target geometry and lack of scattered-light diagnostics on OMEGA EP, we cannot quantify the levels of energetic electrons produced in the interaction. This will be a focus of future experiments. The data obtained on OMEGA EP have implications for MagLIF and suggest that to effectively heat and limit LPI in higher-density gas targets, a reduced intensity or increased beam smoothing may be required.

FY15 NRL Program

The Naval Research Laboratory (NRL) conducted seven target shots on OMEGA EP in FY15 on high-Z coatings of targets.

The first experimental campaign on high-Z coatings was successfully carried out on the OMEGA EP laser by NRL scientists in collaboration with LLE. These thin metallic coatings were previously found to suppress laser imprint on the Nike KrF laser. The experiments are designed to test the effectiveness of these coatings on laser imprint with the NIF-like beams of OMEGA EP. Seven shots were taken in one day despite a new and relatively complex setup. Although improvements in imaging diagnostics must be made, the data obtained show significant reduction in long-wavelength (~100-μm) perturbations for targets coated with 800 Å of Au and 1200 Å of Pd. These coatings are approximately twice the thickness of the ones found to be effective on the KrF laser experiments. Figure 144.144 shows examples of measured time evolution of areal mass nonuniformity for the cases of uncoated targets and targets coated with 800 Å of Au. Follow-up experiments on OMEGA EP with improved diagnostics are planned in the coming year.

ACKNOWLEDGMENT

This work was supported by DOE/NNSA Defense Programs.

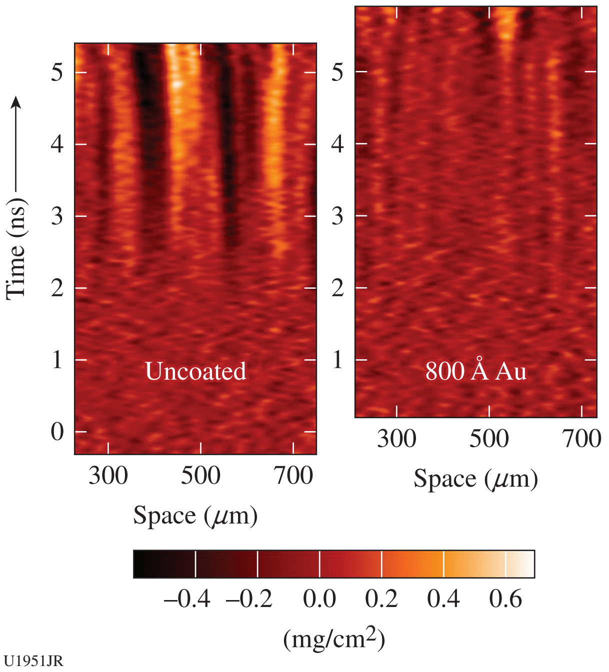

Figure 144.144
Measured time evolution of areal mass nonunifromity for (a) uncoated targets and (b) planar CH targets coated with 800 Å of Au.

FY15 CEA Experiments at the Omega Laser Facility

The Commissariat à l'énergie atomique et aux énergies (CEA) conducted 25 target shots on the OMEGA laser in FY15 for the campaigns discussed below.

Direct-Drive Shock-Timing Study on OMEGA

Principal Investigators: F. Girard, F. Philippe, V. Tassin, O. Landoas, T. Caillaud, S. Laffite, and J. L. Bourgade (CEA); D. T. Michel, V. Yu. Glebov, C. Stoeckl, F. J. Marshall, J. Katz, and W. J. Armstrong (LLE); J. A. Frenje (MIT); and R. Mancini (University of Nevada, Reno)

In inertial confinement fusion (ICF) with lasers, the implosion of a capsule can be driven either directly by the laser in the direct-drive scheme or indirectly by x rays created by laser-energy conversion irradiating a high-*Z* hohlraum in the indirect-drive scheme. Independent of the scheme, energy coupling to the capsule can be an issue, making it difficult to study the implosion. One advantage of a laser direct-drive experiment is the ability of accurate time-resolved measurement of laser-energy coupling, which is why the direct-drive configuration is the perfect platform to study implosion physics.

The implosion study performed in FY14 and FY15 at the Omega Laser Facility is a test of our prediction capability to get implosion time history, which is determined by the implosion velocity. It therefore relies on the knowledge of the energy that the capsule actually absorbs. These campaigns consist of studying direct-drive target stability and shock timing by varying the following:

- pulse shapes (square, two step, or two steps truncated) and, therefore, laser energy
- gas fill (DD, DD + Ar, or DT)
- fill pressure (10 or 15 bars)
- laser irradiation uniformity (uniform or arbitrary P4 irradiation mode)
- capsule shell thickness (20 or 25 μm)

Configurations include a stable platform (one shock) and more-unstable multishock configurations, which are similar to ignition target configurations. Experimental objectives are absorption laser measurements, ablation-front emission of the imploding capsule, core x-ray imaging in addition to core neutron imaging obtained on the same viewing axis, neutron performance (neutron yield, bang time, and ion temperature), ρR measurements, and tracer (Ar and Ti) spectroscopy.

The capsules are irradiated by the 60 OMEGA beams, where the beams are smoothed by distributed phase plates (DPP's), polarization smoothing (PS), and smoothing by spectral dispersion (SSD). In FY14, we used SG4 distributed phase plates, which have a super-Gaussian order of ~4.1, where 95% of laser energy is inside an 860-μm-diam circle. In FY15, we used SG5 phase plates, which have a super-Gaussian order of about 5, where 95% of laser energy is inside an 820-μm-diam circle. In addition to on-target focal-spot spatial uniformity improvement, laser energy in the wings of the spatial profile is reduced with SG5 phase plates compared to SG4.

Laser-irradiation variations have been tested with different pulse shapes (square, two steps, and two step truncated) and an arbitrarily imposed nonuniform laser drive. The laser uniformity was controlled by reducing the energy on two beam cones by 30% and 35%. The overall laser energies delivered on target are very close to expected values. Brillouin backscattered powers vary from 2% to 6% and stimulated Raman scattering (SRS) powers are negligible on all shots. The absorbed laser-energy percentage deduced from calorimeter measurements ranged from 60% to 70% for the square pulse shape and are even higher for two-step pulse shapes, where absorbed energy values reach 70% to 80%.

General Atomics capsules tested in FY14 and CEA capsules tested in FY15 had an inner diameter of 875±25 μm. Capsules made by CEA for FY14 were slightly smaller with an inner diameter of 825±25 μm and a 100-nm-thick titanium layer coated on the plastic shell located 1 μm from the inner surface. All capsules had an 80-nm-thick external aluminum coating to maintain gas inside the capsule. The real DT mixture has been characterized and was precisely the following: T:34%, D:60%, and a hydrogen compound estimated to be 5%.

For FY15, the main parameter variation to be tested was for the shell thickness to reach more-unstable implosion regimes. The ablator thickness was reduced from 25±1 μm to 20±1 μm. All capsules were the same size and had a 100-nm-thick external aluminum coating. The real DT mixture had been improved and was precisely T:60%, D:40%, and the hydrogen compound was estimated to be less than 0.1%.

Direct-drive implosions of DD, DD-Ar, and DT-filled CH capsules conducted during these two shot days with different laser pulse shapes (Fig. 144.145) gave neutron-yield ranges from

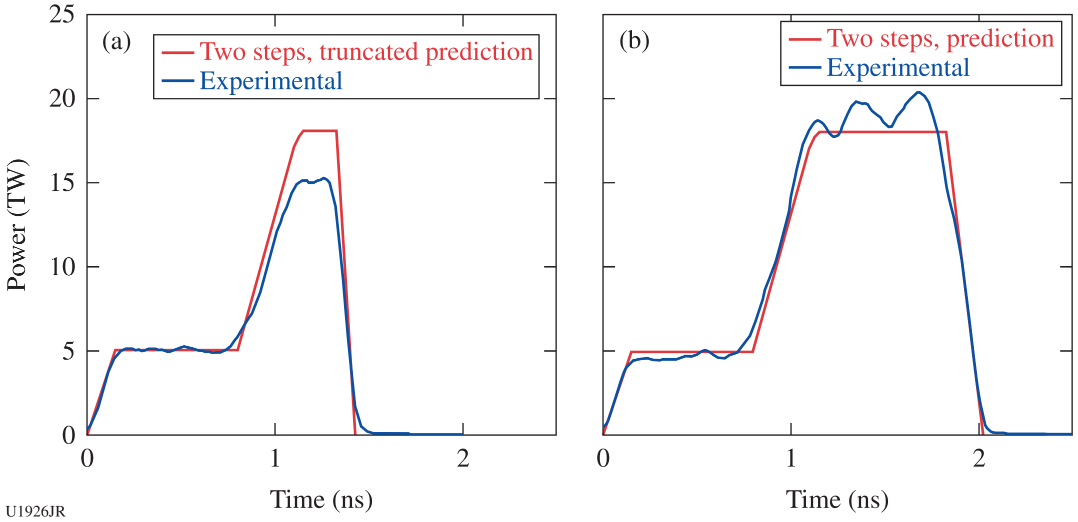

Figure 144.145
New laser pulse shapes tested in this campaign. The red line represents the predicted pulse shape and the blue line represents the experimental pulse shape.

4×10^9 to 2.7×10^{11} for D–D implosions and from 2×10^{12} to 2.7×10^{13} for D–T implosions.

Post-shot simulation results used actual DT compositions and laser irradiation configurations (SG4 and SG5 DPP's). Measured neutron yields are very different from simulated ones for capsules that have a titanium layer inside the shell, showing that the titanium layer significantly perturbs the implosion performance in terms of temperature reached by the core at the time of neutron emission and the way it is taken in simulations (Fig. 144.146). It is interesting to note that faster implosion regimes reached with the thinner capsule shell are reproduced by simulation in the same way as a thicker shell tested previously. Reduction of cross-beam energy transfer (CBET) effects with the use of SG5 phase plates in FY15 and, therefore, better agreement with simulation that does not simulate laser energy losses from CBET will have to be scrutinized.

From FY14 results, bang times defined as the peak neutron-production time are very well reproduced by the code for all cases, and neutron yields go from stable configuration with the square pulse shape and two-step pulse shape to unstable ones with spectroscopic tracers of titanium. In FY15, more-unstable configurations were tested with a thinner shell capsule reduced to 20 μm (25 μm in FY14). This series of experiments has benefited from improved DT mixture with a lower hydrogen contamination, and the new phase plate SG5 whose purpose is the mitigation of CBET losses with the help of better spatial uniformity in the spatial profile (higher order of super-Gaussian) compared to the SG4 one. Preliminary results from FY15 data show very good agreement between experimental and simulated bang times (Fig. 144.147).

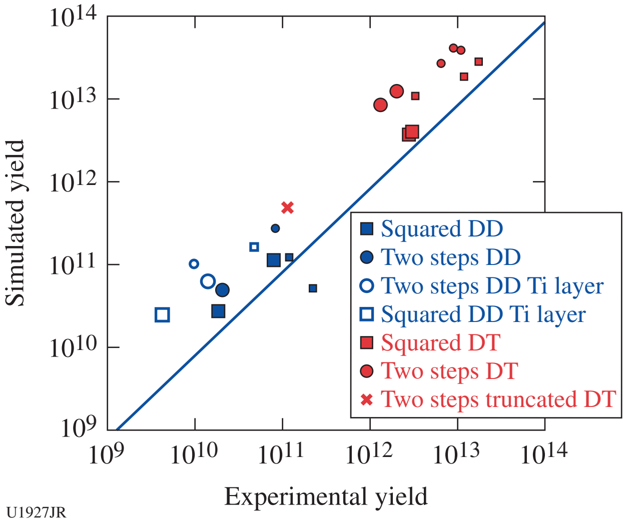

Figure 144.146
Neutron-yield comparison between simulation and experimental results obtained in FY14 and FY15 (small icons refer to a thinner shell tested in FY15).

According to FY14 and FY15 results, bang times are well reproduced by simulations, showing that capsule implosion timings are well understood. This also means that bang-time value discrepancies observed on indirect-drive implosions are caused by energy-coupling physics to the capsule inside the hohlraum that are incorrectly taken into account in numerical simulations.

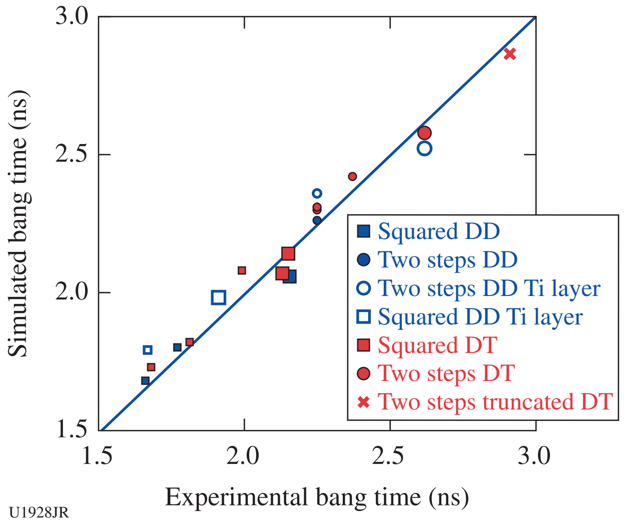

Figure 144.147
Bang-time comparisons between simulation and experimental results obtained in FY14 and FY15.

A system that produces neutron and x-ray images simultaneously on the same axis through the same aperture (penumbral) has been successfully tested. This diagnostic has given good-quality images on both channels that give direct and spatially localized comparison in shape and size of the core x-ray emission and neutron emission zones (cf. Ref. 97).

Ablation-front position evolution with time and, consequently, capsule size and implosion speed was measured by using a soft x-ray imaging system. This information is available during the x-ray emission window, i.e., when the laser is turned on and slightly after. In FY14, maximum speed values between 220 to 250 km/s are obtained at the end the laser pulse for all cases, whatever the pulse shape, gas filling, or irradiation uniformity (Fig. 144.148).

Summary of Neutron-Induced Signals Generated on Close Coaxial Cables During OMEGA High-Yield Neutron Shots

Principal Investigators: J. L. Bourgade, J. L. Leray, B. Villette, O. Landoas (CEA-DAM-DIF); and V. Yu. Glebov, T. C. Sangster, and G. Pien (LLE)

Since the first evidence of this effect in 2002 on OMEGA high-yield DT neutron shots (see Ref. 98), it has been well demonstrated that high-pulsed, 14-MeV neutron irradiation can drive a transient current on coaxial cables.[99]

Since that date and almost every subsequent year during each annual neutron “derby,” shot days on OMEGA have been devoted to testing this effect on various cables and irradiation geometries.

To simplify the insertion of these cables, a special payload tool called “CEA-VD” (vulnerability diagnostic) has been devel-

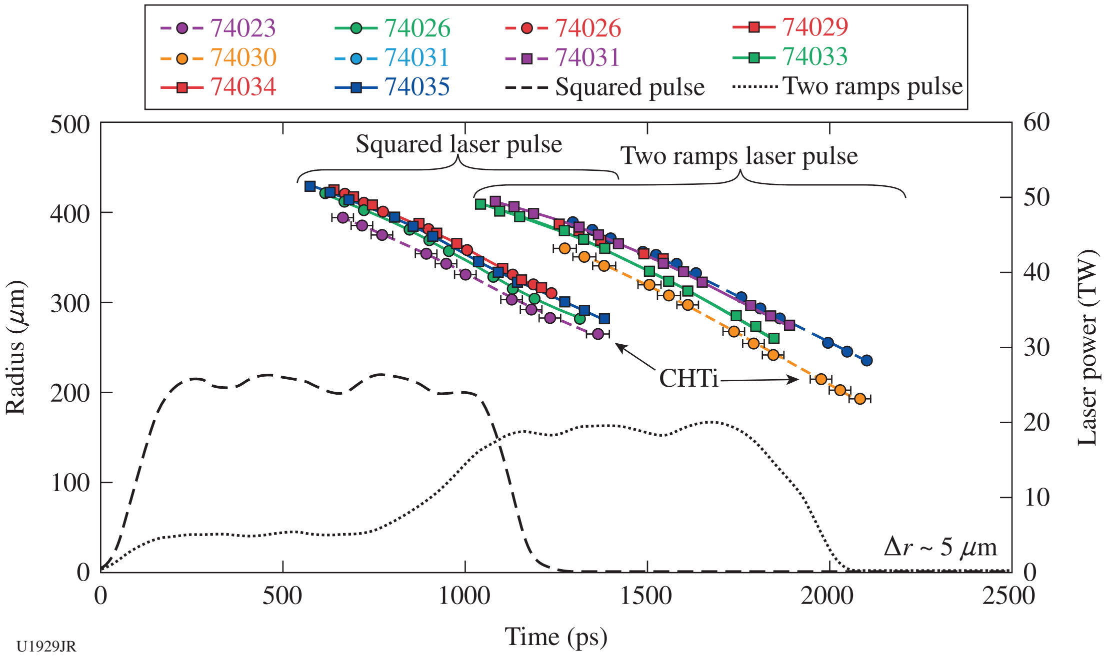

Figure 144.148
Evolutions of capsule size versus time for FY14 capsules where two pulse shapes were tested.

oped to protect and easily position these cables [using a ten-inch manipulator (TIM)] as close as possible to the neutron source produced at the OMEGA target chamber center (TCC) without breaking the target chamber vacuum. Figure 144.149(a) shows this device ready to be mounted on a TIM cart and inserted into a TIM inside the OMEGA target chamber vacuum. The closest right part of this nose cone can be set at ~22 cm from the TCC, where the neutron source is produced by implosion of a DT-filled microballoon. At these distances, the neutron flux on these coaxial cables is similar on OMEGA (where the neutron source is at its maximum around 10^{14} over 4π) to the one for a 10^{16} neutron source on 4π at a distance of 5 m (target chamber radius) for the National Ignition Facility or Laser Mégajoule, which allowed us to check and measure neutron irradiation effects.

Inside this protective nose cone (used for the OMEGA plasma debris issues), one cable at a time can be mounted inside an electromagnetic pulse (EMP) protective cylindrical pipe with an internal diameter of 38 mm. Figure 144.149(b) shows that when this cover is removed, the cable's protective pipe and some other detectors or devices are exposed to this OMEGA intense neutron flux (see, for example, Ref. 100). To avoid any interactions from the hard x rays generated by the laser–plasma instabilities generated by laser interaction on the DT target, a 3-mm-thick tungsten foil is added in front of the protective pipe so only energetic neutrons can reach the cable under test.

Since 2002, many coaxial cables over a wide range of dimensions, materials, and shapes have been exposed to the OMEGA neutron source and their signals recorded. From all the geometries tested during these past years, we have selected the best one for the 3.56-mm (0.141-in.)-diam semirigid "SMA"-type cable used on some of our high-bandwidth detectors [as our coaxial x-ray detectors (XRD's) used on OMEGA DMX (see Ref. 101)] to maximize the neutron-induced signal on the restricted space available for this test inside the 38-mm-diam protective pipe.

Figure 144.150(a) shows the three assembly parts of the protective pipe and the cable geometry tested over the past two years (and the irradiation direction from the neutrons). Figure 144.150(b) shows an enlarged photo of the closest parts of the cable itself engulfed in a black plastic cylinder and araldite glue, exposed to the neutrons flux.

The coaxial cable is serpentine shaped with two spiral shapes to increase the length of the exposed cable as much as possible over the available 38-mm-diam pipe ($L \sim 300$ mm). We chose to use two distinct serpentines placed next to each other and as close as possible along the neutron path to record two signals on the same shot at a nearly equal distance from the neutron source (229/245 mm). Our goal was to be able to discriminate between two magnetic-field levels on the same shot to record their effect on each serpentine: one at a Fe–Nd–B permanent magnet maximum surface field (~4000 G) and the other to a desired value of close to 0 Gauss. Moreover, to obtain the temporal separation needed to record each signal separately on the same scope, each serpentine is connected to the other one by a 1-m-long coaxial cable (~6-ns time separation) wrapped (2 × 60-cm cable length) inside the protective pipe along its length. Finally, to avoid inducing a signal pileup after reflection to the open end of the cable, a second 0.5-m-long coaxial cable is added on the free serpentine end and is connected to a 50-Ω resistive adaptation (no electrical reflection of the signals generated on each serpentine).

Unfortunately the restricted available space between the two serpentines does not allow us to shield enough of the first ser-

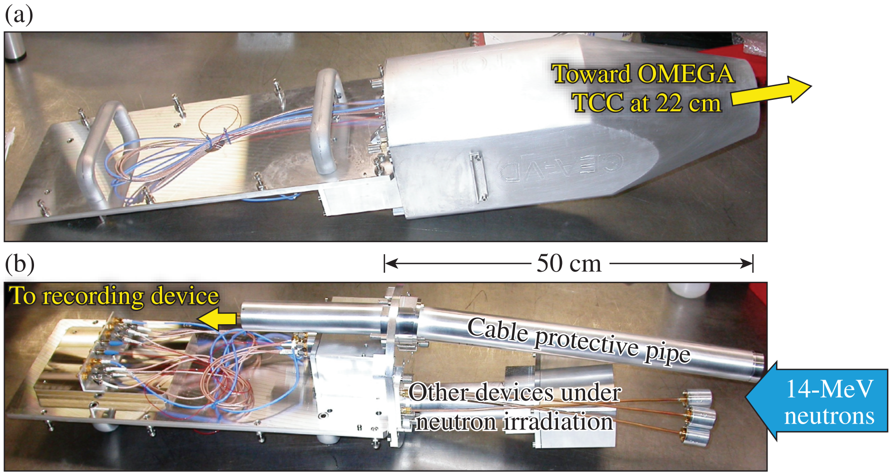

Figure 144.149
(a) CEA-VD payload is ready for insertion into a ten-inch manipulator (TIM) on OMEGA. (b) The protective cover has been removed to show the internal parts irradiated by the OMEGA neutron flux and the protective pipe used to irradiate the coaxial cable.

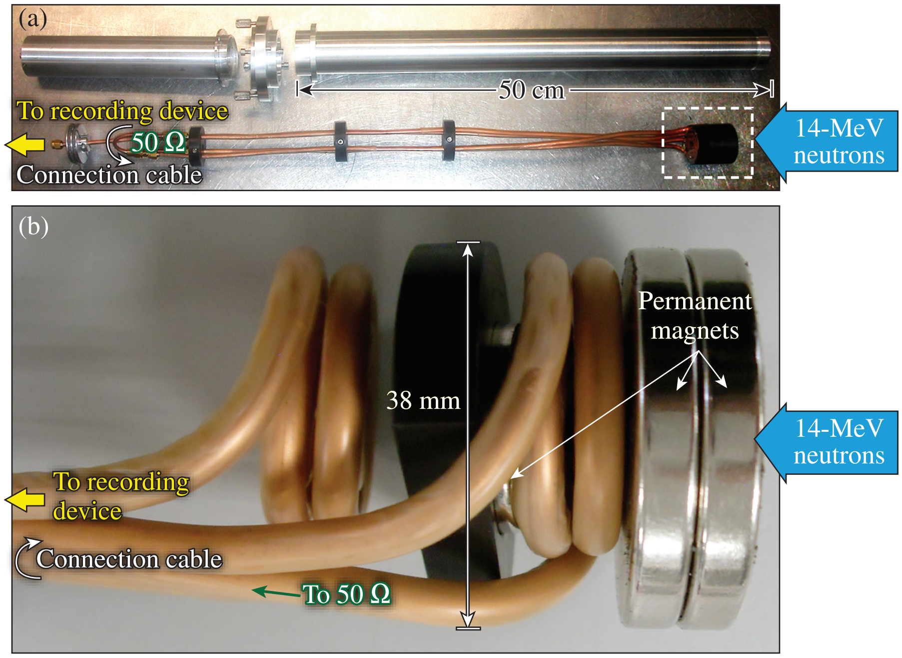

U1931JR

Figure 144.150
(a) The protective pipe (in three parts) and the SMA coaxial cable arrangement. (b) Enlarged view of the dashed rectangle in (a) with the plastic and araldite protection removed, showing the coaxial cable wrapped into two serpentines and the permanent magnets (silvered disks).

pentine's localized magnetic field to get a sufficiently low (down to few gauss only) magnetic field for our second serpentine. So we decided to use the two serpentines together on the actual magnetic conditions generated by the permanent magnets of the first serpentine. Even though the second serpentine's magnetic field is lower than the first one, we decided to use it as is.

In FY14 we tested this double-serpentine device on OMEGA high-yield neutron shots with the permanent magnets demagnetized (by heating them above their Curie temperature to avoid their magnetic field).

In FY15 we again magnetized this same device by placing it into a high-dc magnetic field generated by a powerful solenoid at the CNRS "Laboratoire National des Champs Magnétiques Intenses" de Grenoble (France). To get the maximum magnetic field into our permanent magnets, the solenoid was able to generate step by step up to 6 T over a few minutes.

Figure 144.151 shows the evolution in time of the FY14 (without magnetic field) and the FY15 (with magnetic field) signals on the same scale (neutron yield 3×10^{13} in FY14 and up to 7.5×10^{13} in FY15).

The first peak is associated with the second serpentine placed farthest from the neutron source. Its lower signal level in comparison to the second peak is induced by an increased distance to the source and also by the neutron absorption inside the araldite glue and the coaxial cable material present between them [equivalent to ~15 mm of CHON (araldite glue surrounding the coaxial cable)].

The effect of the magnetic field is obvious from Fig. 144.151 by the drastic decrease in the signal with respect to the FY14 case (without B magnetic field) by a factor of ~12 and by also taking linearly into account the higher neutron yield for the FY15 case (with a magnetic field). Moreover, some changes in the temporal

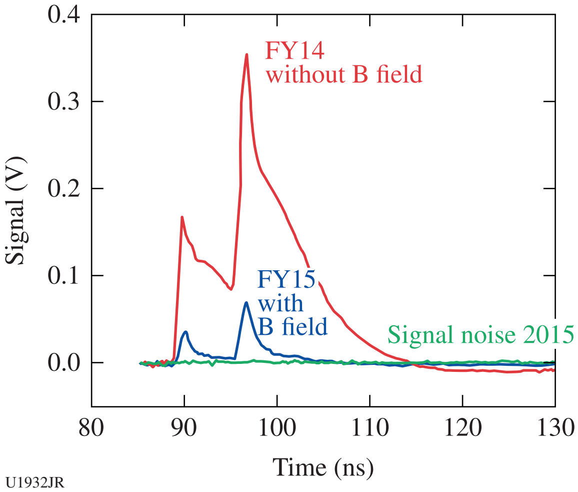

U1932JR

Figure 144.151
The evolution of the signals in time without (FY14, red) and with (FY15, blue) the magnetic field of the same serpentine-shaped coaxial cable on high-yield OMEGA neutron shots, together with the signal recorded on a low-neutron-yield shot (green, shot 77372, 2.2×10^{12}) showing the signal noise of such a measurement chain.

shapes of these signals can be found especially on their trailing edge (much-less trailing signal after its maximum peak for the magnetic-field case). Finally, the ratio of both peaks of the two serpentines (with and without a magnetic field) remains constant in spite of a weaker magnetic field on the second serpentine (first peaks on the Fig. 144.151), proving that the strength of the magnetic field can be lower than on the first serpentine, producing a similar decreasing effect on the signal level.

Further investigations are needed, theoretically and by simulation (with the Geant4 code) to take into account the effect of this magnetic field on the generated proton recoils that generate the measured prompt and delayed currents in level and time; experimental investigations are also needed, if possible, on FY16's neutron derby shot days, to check (as already demonstrated in the past on other coaxial cable devices) the effects of the proton recoils induced into the CHON and able to cross the Cu exterior layer of the coaxial cable for the most energetic of them to generate a current inside it.

CMOS Active Pixel Sensor on OMEGA: Reduced Neutron-Induced Perturbation on X-Ray Imaging Using the Global Reset Technique

Principal Investigator: P. Paillet

Co-investigators: V. Goiffon, S. Girard, O. Duhamel, S. Darbon, A. Rousseau, A. Chabane, P. Cervantes, P. Magnan, J.-L. Bourgade, V. Yu. Glebov, G. Pien, and T. C. Sangster

Radiation-tolerance studies of a complementary metal–oxide–semiconductor (CMOS) image sensor used in plasma diagnostics have been performed as part of a collaboration among CEA, the Institut Supérieur de l'Aéronautique et de l'Espace (ISAE, Toulouse), and the University of Saint-Etienne. Previous experiments performed in FY13 and FY14 demonstrated the relevance of a developed hardening technique to remove parasitic signals induced by the neutron pulse occurring during a DT shot. The CMOS sensor is now part of a basic x-ray imaging diagnostic composed of a pinhole array and a thin layer of P43 (a long-decay-time scintillator) layered on the sensor surface. This diagnostic was inserted via a ten-inch manipulator (TIM) into the chamber and exposed to neutron yields produced by OMEGA DT shots to record an x-ray self-emission image of the imploding target. Successful images from the x-ray self-emission of imploding targets have been recorded for shots with high neutron yields. As expected, the global reset mode efficiently reduced the transient perturbation (parasitic white pixels) without degrading the image quality. This year the neutron yields reached very high values (up to ~10^{14} n), a factor of 10 higher than during the FY14 campaign, and our basic diagnostic was able to provide images of the imploding targets (see Fig. 144.152) without a neutron-induced parasitic signal.

This FY15 campaign demonstrated the ability to use an imaging system based on APS sensors to record an image of the x-ray self-emission of an imploding target during very high neutron yield DT shots on OMEGA. Further improvements in the experiment design will be completed during the next neutron campaign in FY16, investigating evolutions, investigating evolutions and new concepts of APS image sensors.

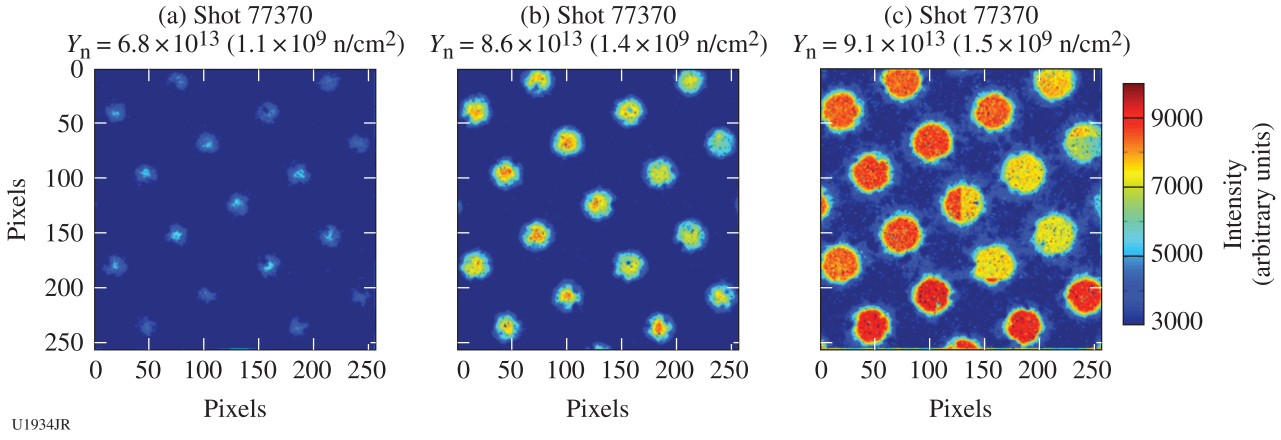

Figure 144.152
Typical image recording on the APS sensor, for neutron yields in the range of 7 to 9 × 10^{13}. The global reset mode is used for all images, proving that its efficiency makes it possible to image x-ray self-emission of an imploding target without a neutron-induced parasitic signal.

Investigations on Neutron-Induced Electric Currents in Dielectrics Used in Coaxial Cables Near Inertial Confinement Fusion Experiments

Principal Investigators: J.-L. Leray, J.-E. Sauvestre, J. Baggio, S. Bazzoli, J.-L. Bourgade, O. Duhamel, J. Gazave, and P. Paillet (CEA/DIF); and V. Yu. Glebov, T. C. Sangster, and G. Pien (LLE)

To date, neutron fluxes produced nearby in fusion reactors have not been of great concern for electrical equipment involved in diagnostics because the flux and fluence of the ionizing burst had relatively mild effects. However, as recently as the 1990s, we managed to observe milliamps of currents across a medium-power silicon transistor at the collector electrode in experiments near the target of the PHEBUS laser. As the neutron yield dramatically increased, some new phenomena were, therefore, likely to occur. Attention was paid to the effect of neutrons in dielectrics. Effectively, for the first time on OMEGA, coaxial cables distinctly produced a complex signal, as shown in a companion report in this review.[102] This very short signal always consists of a peak, seeming to reproduce the neutron flux, followed by a "delayed" longer component able to last for several nanoseconds. Also noteworthy, the signal is observed on a resistive load even when no voltage is applied to the cable; i.e., the cable itself acts as a current generator. In other words, the cable acts as a detector producing the so-called "radiation-induced electromotive force" with two components: the prompt one and the delayed one. How will these components evolve if one applies a voltage, if one changes the cable size, or the geometry (line, warped cable, cable with an angle with respect to the particle flux)? Technologically, the cables' inner conductors are usually insulated with polyethylene, $(-\mathrm{CH_2}-)_n$, referred to as PE, but sometimes polytetraflurorethylene $(-\mathrm{CF_2})_n$, also called PTFE or Teflon$^{\mathrm{TM}}$ or, more rarely, polyetherethetketone (PEEK), a thermoplastic that is tough, strong, rigid, and creep resistant, able to print in 3-D, has excellent radiation resistance, and, importantly, is compatible with use under high vacuum. What happens to the current response, amplitude, duration, and charge if the cable dielectrics nature is changed?

To answer these intriguing questions and develop a consistent model, we first defined a specific mock-up in a plane geometry sandwiched between two electrodes that has been proposed and always used throughout DT fusion campaigns as a canonical configuration. This mock-up consists of aluminum electrodes in a 1-cm^2 area sandwiching a dielectric (Fig. 144.153). It has been specially designed to evacuate the residual air during vacuum pumping and to allow very high bandwidth transfer of the signal across the measurement coax. A cylinder of 5 mm of tungsten was plugged into the front side of the mock-up to screen the plasma x ray resulting from the shot. The peak signals the linear dependence on the neutron flux. The model of this neutron-induced current without a biasing voltage applied is based on the movement of the ion recoiling from the neutron interactions with the dielectric (mainly the bulk of the dielectric). The signal depends on the angle between the neutron flux and the disk axis. The signal cancels when the beam is perpendicular to the disk plane because of the symmetry of the charged recoils' distribution. The new neutron-induced electromotive force effect, the orders of magnitude, and the angular dependence were computed using the Monte Carlo code Geant4, and the excellent fit was published in 2008 (Ref. 103).

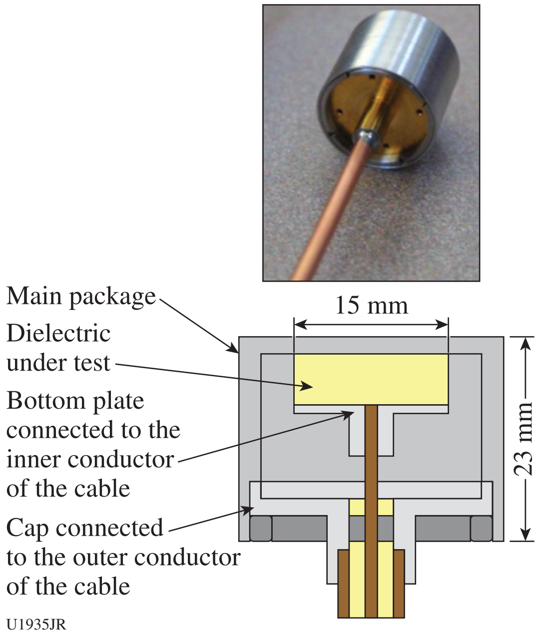

Figure 144.153
Experimental canonical detector mock-up for high-bandwidth measurement of transients developed at electrodes by inserting a dielectric.

In the second phase of the study, both the prompt and delayed signals were described for the first time in the context of very short pulses of neutrons and in the presence of an electric field from –1 kV/cm to 1 kV/cm (Fig. 144.154). The use of much faster recorders that provided a 7-GHz analog bandwidth with a maximum sampling rate of 50 GS/s was permitted to obtain better resolution of the signals in PE, PTFE, and PEEK. Here, the classical effect is the radiation-induced conductivity that occurs after the ionizing recoils have excited the electrons (and holes) in the dielectrics along their tracks. The electric field modulates the charge-carrier currents. The prompt and delayed components of the radiation-induced conductivity were

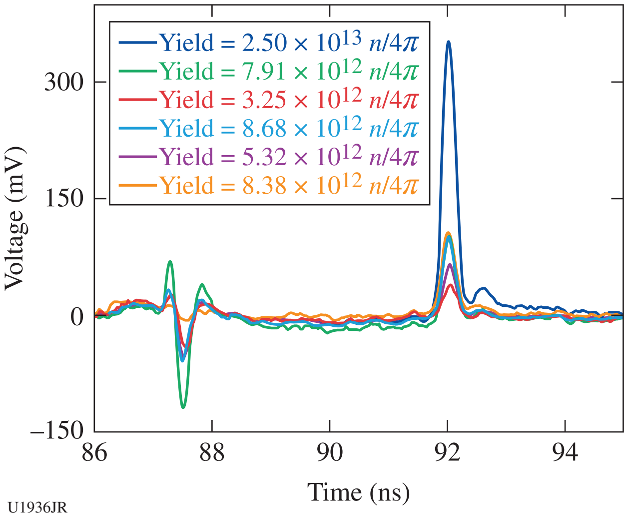

Figure 144.154
Voltage signals on 50 Ω provided by the canonical detector with a PE dielectric disk located 28.8 cm from the neutrons' source at various neutron yields. The first peak—negative signal—after 87 ns is caused by an x-ray pulse emitted by plasma-generating photoelectrons; the second—positive signal—and third pulses are attributed to 14-MeV neutrons arriving on the disk, generating a prompt signal (positive peak) at 92 ns caused by neutron recoils and a second peak after 92.5 ns (smaller, delayed) caused by bipolar diffusion of charges (i.e., electron first and, later, holes) to the electrodes.

modeled using classical drift and diffusion of charge carriers in dielectrics in 2012 (Ref. 99). Models were used to determine values of the lifetime of electrons and holes in dielectrics, in the subnanosecond to nanosecond range according to the dielectrics. This study and modeling made it possible to assess the shape of the effect of ICF neutrons and compare with prior measurements of FY13 (Ref. 104) with literature, which up to now treated only the effects on longer pulses from electron and x-ray bunches produced by LINAC's.

We will now focus on applying these models and basic material parameters to realistic cables in coaxial linear and folded geometries.

REFERENCES

1. G. Malamud *et al*., High Energy Density Phys. **9**, 672 (2013).
2. J. Cowan, Los Alamos National Laboratory, private communication (2015).
3. W. C. Wan *et al*., Phys. Rev. Lett. **115**, 145001 (2015).
4. F. Miniati, ETH Zurich, private communication (2015).
5. A. B. Zylstra, "Using Fusion-Product Spectroscopy to Study Inertial Fusion Implosions, Stopping Power, and Astrophysical Nucleosynthesis at OMEGA and the NIF," Ph.D. thesis, Massachusetts Institute of Technology, 2015.
6. H. G. Rinderknecht, "Studies of Non-Hydrodynamic Processes in ICF Implosions on OMEGA and the National Ignition Facility," Ph.D. thesis, Massachusetts Institute of Technology, 2015.
7. J. A. Frenje, P. E. Grabowski, C. K. Li, F. H. Séguin, A. B. Zylstra, M. Gatu Johnson, R. D. Petrasso, V. Yu. Glebov, and T. C. Sangster, Phys. Rev. Lett. **115**, 205001 (2015).
8. G. Kagan, D. Svyatskiy, H.G. Rinderknecht, M. J. Rosenberg, A. B. Zylstra, C. K. Huang, and C. J. McDevitt, Phys. Rev. Lett. **115**, 105002 (2015).
9. A. B. Zylstra, J. A. Frenje, P. E. Grabowski, C. K. Li, G. W. Collins, P. Fitzsimmons, S. Glenzer, F. Graziani, S. B. Hansen, S. X. Hu, M. Gatu Johnson, P. Keiter, H. Reynolds, J. R. Rygg, F. H. Séguin, and R. D. Petrasso, Phys. Rev. Lett. **114**, 215002 (2015).
10. M. J. Rosenberg, C. K. Li, W. Fox, A. B. Zylstra, C. Stoeckl, F. H. Séguin, J. A. Frenje, and R. D. Petrasso, Phys. Rev. Lett. **114**, 205004 (2015).
11. H. G. Rinderknecht, M. J. Rosenberg, C. K. Li, N. M. Hoffman, G. Kagan, A. B. Zylstra, H. Sio, J. A. Frenje, M. Gatu Johnson, F. H. Séguin, R. D. Petrasso, P. Amendt, C. Bellei, S. Wilks, J. Delettrez, V. Yu. Glebov, C. Stoeckl, T. C. Sangster, D. D. Meyerhofer, and A. Nikroo, Phys. Rev. Lett. **114**, 025001 (2014).
12. H. G. Rinderknecht, M. J. Rosenberg, A. B. Zylstra, B. Lahmann, F. H. Séguin, J. A. Frenje, C. K. Li, M. Gatu Johnson, R. D. Petrasso, L. F. Berzak Hopkins, J. A. Caggiano, L. Divol, E. P. Hartouni, R. Hatarik, S. P. Hatchett, S. Le Pape, A. J. Mackinnon, J. M. McNaney, N. B. Meezan, M. J. Moran, P. A. Bradley, J. L. Kline, N. S. Krasheninnikova, G. A. Kyrala, T. J. Murphy, M. J. Schmitt, I. L. Tregillis, S. H. Batha, J. P. Knauer, and J. D. Kilkenny, Phys. Plasmas **22**, 082709 (2015).
13. M. J. Rosenberg, F. H. Séguin, P. A. Amendt, S. Atzeni, H. G. Rinderknecht, N. M. Hoffman, A. B. Zylstra, C. K. Li, H. Sio, M. Gatu Johnson, J. A. Frenje, R. D. Petrasso, V. Yu. Glebov, C. Stoeckl, W. Seka, F. J. Marshall, J. A. Delettrez, T. C. Sangster, R. Betti, S. C. Wilks, J. Pino, G. Kagan, K. Molvig, and A. Nikroo, Phys. Plasmas **22**, 062702 (2015).
14. A. B. Zylstra, J. A. Frenje, F. H. Séguin, J. R. Rygg, A. Kritcher, M. J. Rosenberg, H. G. Rinderknecht, D. G. Hicks, S. Friedrich, R. Bionta, N. B. Meezan, R. Olson, J. Atherton, M. Barrios, P. Bell, R. Benedetti, L. Berzak Hopkins, R. Betti, D. Bradley, D. Callahan, D. Casey, G. Collins, E. L. Dewald, S. Dixit, T. Döppner, M. J. Edwards, M. Gatu Johnson, S. Glenn, G. Grim, S. Hatchett, O. Jones, S. Khan, J. Kilkenny, J. Kline, J. Knauer, G. Kyrala, O. Landen, S. LePape, C. K. Li, J. Lindl, T. Ma, A. Mackinnon, M. J.-E. Manuel, D. Meyerhofer, E. Moses, S. R. Nagel, A. Nikroo, T. Parham, A. Pak, R. D. Petrasso, R. Prasad, J. Ralph, H. F. Robey, J. S. Ross, T. C. Sangster, S. Sepke, N. Sinenian, H. W. Sio, B. Spears, R. Tommasini, R. Town, S. Weber, D. Wilson, C. Yeamans, and R. Zacharias, Phys. Plasmas **22**, 056301 (2015).
15. N. M. Hoffman, G. B. Zimmerman, K. Molvig, H. G. Rinderknecht, M. J. Rosenberg, B. J. Albright, A. N. Simakov, H. Sio, A. B. Zylstra, M. Gatu Johnson, F. H. Séguin, J. A. Frenje, C. K. Li, R. D. Petrasso, D. M. Higdon, G. Srinivasan, V. Yu. Glebov, C. Stoeckl, W. Seka, and T. C. Sangster, Phys. Plasmas **22**, 052707 (2015).

16. M. J. Rosenberg, C. K. Li, W. Fox, I. Igumenshchev, F. H. Séguin, R. P. J. Town, J. A. Frenje, C. Stoeckl, V. Glebov, and R. D. Petrasso, Phys. Plasmas **22**, 042703 (2015).

17. M. J. Rosenberg, A. B. Zylstra, F. H. Séguin, H. G. Rinderknecht, J. A. Frenje, M. Gatu Johnson, H. Sio, C. J. Waugh, N. Sinenian, C. K. Li, R. D. Petrasso, P. W. McKenty, M. Hohenberger, P. B. Radha, J. A. Delettrez, V. Yu. Glebov, R. Betti, V. N. Goncharov, J. P. Knauer, T. C. Sangster, S. LePape, A. J. Mackinnon, J. Pino, J. M. McNaney, J. R. Rygg, P. A. Amendt, C. Bellei, L. R. Benedetti, L. Berzak Hopkins, R. M. Bionta, D. T. Casey, L. Divol, M. J. Edwards, S. Glenn, S. H. Glenzer, D. G. Hicks, J. R. Kimbrough, O. L. Landen, J. D. Lindl, T. Ma, A. MacPhee, N. B. Meezan, J. D. Moody, M. J. Moran, H.-S. Park, B. A. Remington, H. Robey, M. D. Rosen, S. C. Wilks, R. A. Zacharias, H. W. Herrmann, N. M. Hoffman, G. A. Kyrala, R. J. Leeper, R. E. Olson, J. D. Kilkenny, and A. Nikroo, Phys. Plasmas **21**, 122712 (2014).

18. A. B. Zylstra, J. A. Frenje, F. H. Séguin, D. G. Hicks, E. L. Dewald, H. F. Robey, J. R. Rygg, N. B. Meezan, M. J. Rosenberg, H. G. Rinderknecht, S. Friedrich, R. Bionta, R. Olson, J. Atherton, M. Barrios, P. Bell, R. Benedetti, L. Berzak Hopkins, R. Betti, D. Bradley, D. Callahan, D. Casey, G. Collins, S. Dixit, T. Döppner, D. Edgell, M. J. Edwards, M. Gatu Johnson, S. Glenn, S. Glenzer, G. Grim, S. Hatchett, O. Jones, S. Khan, J. Kilkenny, J. Kline, J. Knauer, A. Kritcher, G. Kyrala, O. Landen, S. LePape, C. K. Li, J. Lindl, T. Ma, A. Mackinnon, A. Macphee, M. J.-E. Manuel, D. Meyerhofer, J. Moody, E. Moses, S. R. Nagel, A. Nikroo, A. Pak, T. Parham, R. D. Petrasso, R. Prasad, J. Ralph, M. Rosen, J. S. Ross, T. C. Sangster, S. Sepke, N. Sinenian, H. W. Sio, B. Spears, P. Springer, R. Tommasini, R. Town, S. Weber, D. Wilson, and R. Zacharias, Phys. Plasmas **21**, 112701 (2014).

19. M. J. Rosenberg, C. K. Li, W. Fox, I. Igumenshchev, F. H. Séguin, R. P. J. Town, J. A. Frenje, C. Stoeckl, V. Glebov, and R. D. Petrasso, Nat. Commun. **6**, 6190 (2014).

20. C. M. Huntington, F. Fiuza, J. S. Ross, A. B. Zylstra, R. P. Drake, D. H. Froula, G. Gregori, N. L. Kugland, C. C. Kuranz, M. C. Levy, C. K. Li, J. Meinecke, T. Morita, R. Petrasso, C. Plechaty, B. A. Remington, D. D. Ryutov, Y. Sakawa, A. Spitkovsky, H. Takabe, and H. S. Park, Nat. Phys. **11**, 173 (2015).

21. C. J. Waugh, M. J. Rosenberg, A. B. Zylstra, J. A. Frenje, F. H. Séguin, R. D. Petrasso, V. Yu. Glebov, T. C. Sangster, and C. Stoeckl, Rev. Sci. Instrum. **86**, 053506 (2015).

22. J. Rojas-Herrera, H. G. Rinderknecht, A. B. Zylstra, M. Gatu Johnson, D. Orozco, M. J. Rosenberg, H. Sio, F. H. Seguin, J. A. Frenje, C. K. Li, and R. D. Petrasso, Rev. Sci. Instrum. **86**, 033501 (2015).

23. M. J. Rosenberg, A. B. Zylstra, J. A. Frenje, H. G. Rinderknecht, M. Gatu Johnson, C. J. Waugh, F. H. Séguin, H. Sio, N. Sinenian, C. K. Li, R. D. Petrasso, V. Yu. Glebov, M. Hohenberger, C. Stoeckl, T. C. Sangster, C. B. Yeamans, S. LePape, A. J. Mackinnon, R. M. Bionta, B. Talison, D. T. Casey, O. L. Landen, M. J. Moran, R. A. Zacharias, J. D. Kilkenny, and A. Nikroo, Rev. Sci. Instrum. **85**, 103504 (2014).

24. L. Willingale, A. G. R. Thomas, P. M. Nilson, H. Chen, J. Cobble, R. S. Craxton, A. Maksimchuk, P. A. Norreys, T. C. Sangster, R. H. H. Scott, C. Stoeckl, C. Zulick, and K. Krushelnick, New J. Phys. **15**, 025023 (2013).

25. R. Betti, C. D. Zhou, K. S. Anderson, L. J. Perkins, W. Theobald, and A. A. Solodov, Phys. Rev. Lett. **98**, 155001 (2007).

26. R. Nora, W. Theobald, R. Betti, F. J. Marshall, D. T. Michel, W. Seka, B. Yaakobi, M. Lafon, C. Stoeckl, J. A. Delettrez, A. A. Solodov, A. Casner, C. Reverdin, X. Ribeyre, A. Vallet, J. Peebles, F. N. Beg, and M. S. Wei, Phys. Rev. Lett. **114**, 045001 (2015).

27. W. Theobald, R. Nora, W. Seka, M. Lafon, K. S. Anderson, M. Hohenberger, F. J. Marshall, D. T. Michel, A. A. Solodov, C. Stoeckl, D. H. Edgell, B. Yaakobi, A. Casner, C. Reverdin, X. Ribeyre, A. Shvydky, A. Vallet, J. Peebles, F. N. Beg, M. S. Wei, and R. Betti, Phys. Plasmas **22**, 056310 (2015).

28. H. Chen, S. C. Wilks, J. D. Bonlie, E. P. Liang, J. Myatt, D. F. Price, D. D. Meyerhofer, and P. Beiersdorfer, Phys. Rev. Lett. **102**, 105001 (2009).

29. H. Chen, S. C. Wilks, D. D. Meyerhofer, J. Bonlie, C. D. Chen, S. N. Chen, C. Courtois, L. Elberson, G. Gregori, W. Kruer, O. Landoas, J. Mithen, J. Myatt, C. D. Murphy, P. Nilson, D. Price, M. Schneider, R. Shepherd, C. Stoeckl, M. Tabak, R. Tommasini, and P. Beiersdorfer, Phys. Rev. Lett. **105**, 015003 (2010).

30. H. Chen, G. Fiksel, D. Barnak, P.-Y. Chang, R. F. Heeter, A. Link, and D. D. Meyerhofer, Phys. Plasmas **21**, 040703 (2014).

31. O. V. Gotchev, J. P. Knauer, P. Y. Chang, N. W. Jang, M. J. Shoup, III, D. D. Meyerhofer, and R. Betti, Rev. Sci. Instrum. **80**, 043504 (2009).

32. H. Chen, F. Fiuza, A. Link, A. Hazi, M. Hill, D. Hoarty, S. James, S. Kerr, D. D. Meyerhofer, J. Myatt, J. Park, Y. Sentoku, and G. J. Williams, Phys. Rev. Lett. **114**, 215001 (2015).

33. H. Chen, D. D. Meyerhofer, S. C. Wilks, R. Cauble, F. Dollar, K. Falk, G. Gregori, A. Hazi, E. I. Moses, C. D. Murphy, J. Myatt, J. Park, J. Seely, R. Shepherd, A. Spitkovsky, C. Stoeckl, C. I. Szabo, R. Tommasini, C. Zulick, and P. Beirsdorfer, High Energy Density Phys. **7**, 225 (2011).

34. G. Fiksel, W. Fox, A. Bhattacharjee, D. H. Barnak, P.-Y. Chang, K. Germaschewski, S. X. Hu, and P. M. Nilson, Phys. Rev. Lett. **113**, 105003 (2014).

35. M. Brüllmann *et al*., Phys. Lett. B **25**, 269 (1967).

36. G. Hale, Los Alamos National Laboratory, private communication (2015).

37. D. K. Spaulding *et al*., Phys. Rev. Lett. **108**, 065701 (2012).

38. B. Militzer, High Energy Density Phys. **9**, 152 (2013).

39. J. S. Ross *et al*., Rev. Sci. Instrum. **85**, 11E613 (2014).

40. J. S. Ross *et al*., Phys. Rev. Lett. **110**, 145005 (2013).

41. J. R. Rygg, J. H. Eggert, A. E. Lazicki, F. Coppari, J. A. Hawreliak, D. G. Hicks, R. F. Smith, C. M. Sorce, T. M. Uphaus, B. Yaakobi, and G. W. Collins, Rev. Sci. Instrum. **83**, 113904 (2012).

42. S. Ivancic, D. Haberberger, H. Habara, T. Iwawaki, K. S. Anderson, R. S. Craxton, D. H. Froula, D. D. Meyerhofer, C. Stoeckl, K. A. Tanaka, and W. Theobald, Phys. Rev. E **91**, 051101(R) (2015).

43. D. E. Fratanduono *et al*., J. Appl. Phys. **116**, 033517 (2014).

44. D. T. Casey, D. T. Woods, V. A. Smalyuk, O. A. Hurricane, V. Y. Glebov, C. Stoeckl, W. Theobald, R. Wallace, A. Nikroo, M. Schoff, C. Shuldberg, K. J. Wu, J. A. Frenje, O.L. Landen, B. A. Remington, and G. Glendinning, Phys. Rev. Lett. **114**, 205002 (2015).

45. M. D. Knudson and M. P. Desjarlais, Phys. Rev. B **88**, 184107 (2013).

46. D. G. Hicks, T. R. Boehly, J. H. Eggert, J. E. Miller, P. M. Celliers, and G. W. Collins, Phys. Rev. Lett. **97**, 025502 (2006).

47. M. Millot *et al*., Science **347**, 418 (2015).

48. Y. Ping, D. G. Hicks, B. Yaakobi, F. Coppari, D. Fratanduono, S. Hamel, J. H. Eggert, J. R. Rygg, R. F. Smith, T. R. Boehly, and G. W. Collins, Phys. Rev. Lett. **111**, 065501 (2013).

49. Y. Ping, D. G. Hicks, B. Yaakobi, F. Coppari, J. Eggert, and G. W. Collins, Rev. Sci. Instrum. **84**, 123105 (2013).

50. Y. Ping, A. Fernandez-Panella, H. Sio, A. Correa, R. Shepherd, O. Landen, R. A. London, P. A. Sterne, H. D. Whitley, D. Fratanduono, T. R. Boehly, and G. W. Collins, Phys. Plasmas **22**, 092701 (2015).

51. R. F. Heeter, S. B. Hansen, K. B. Fournier, M. E. Foord, D. H. Froula, A. J. Mackinnon, M. J. May, M. B. Schneider, and B. K. F. Young, Phys. Rev. Lett. **99**, 195001 (2007).

52. K. B. Fournier *et al*., Phys. Rev. Lett. **92**, 165005 (2004).

53. K. B. Fournier, J. H. Satcher, M. J. May, J. F. Poco, C. M. Sorce, J. D. Colvin, S. B. Hansen, S. A. MacLaren, S. J. Moon, J. F. Davis, F. Girard, B. Villette, M. Primout, D. Babonneau, C. A. Coverdale, and D. E. Beutler, Phys. Plasmas **16**, 052703 (2009).

54. F. Pérez, J. J. Kay, J. R. Patterson, J. Kane, B. Villette, F. Girard, C. Reverdin, M. May, J. Emig, C. Sorce, J. Colvin, S. Gammon, J. Jaquez, J. H. Satcher Jr., and K. B. Fournier, Phys. Plasmas **19**, 083101 (2012).

55. F. Pérez *et al*., Phys. Plasmas **21**, 023102 (2014).

56. F. Pérez *et al*., Phys. Plasmas **22**, 113112 (2015).

57. S. Root *et al*., Sandia National Laboratories, Albuquerque, NM, SAND2013-4974C (2013); R. J. Magyar, S. Root, and T. R. Mattsson, J. Phys.: Conf. Ser. **500**, 162004 (2014).

58. S. Chandrasekhar, *Radiative Transfer* (Dover Publications, New York, 1960).

59. C. A. Back *et al*., Phys. Plasmas **7**, 2126 (2000).

60. C. A. Back *et al*., Phys. Rev. Lett. **84**, 274 (2000).

61. T. Afshar-rad *et al*., Phys. Rev. Lett. **73**, 74 (1994).

62. P. Keiter *et al*., Phys. Plasmas **15**, 056901 (2008).

63. T. S. Perry *et al*., J. Quant. Spectrosc. Radiat. Transf. **51**, 273 (1994).

64. A. S. Moore *et al*., J. Quant. Spectrosc. Radiat. Transf. **159**, 19 (2015).

65. J. Massen *et al*., Phys. Rev. E **50**, 5130 (1994).

66. J. M. Taccetti *et al*., Rev. Sci. Instrum. **83**, 023506 (2012).

67. D. Hoarty *et al*., Phys. Rev. Lett. **82**, 3070 (1999).

68. D. Hoarty *et al*., Phys. Plasmas **6**, 2171 (1999).

69. S. Blinnikov *et al*., High Energy Density Phys. **9**, 17 (2013).

70. P. Höflich, in *High Energy Density Laboratory Astrophysics*, edited by G. A. Kyrala (Springer Netherlands, 2005), pp. 87–92.

71. L. J. Suter *et al*., Phys. Plasmas **3**, 2057 (1996).

72. T. S. Perry *et al*., Astrophys. J. Suppl. Ser. **127**, 433 (2000).

73. C. C. Smith, J. Quant. Spectrosc. Radiat. Transf. **81**, 451 (2003).

74. C. A. Haynam *et al*., Appl. Opt. **46**, 3276 (2007).

75. T. M. Guymer *et al*., Phys. Plasmas **22**, 043303 (2015).

76. T. R. Boehly, D. L. Brown, R. S. Craxton, R. L. Keck, J. P. Knauer, J. H. Kelly, T. J. Kessler, S. A. Kumpan, S. J. Loucks, S. A. Letzring, F. J. Marshall, R. L. McCrory, S. F. B. Morse, W. Seka, J. M. Soures, and C. P. Verdon, Opt. Commun. **133**, 495 (1997).

77. D. Hoarty *et al*., Phys. Rev. Lett. **78**, 3322 (1997).

78. O. Willi *et al*., Astrophys. J. Suppl. Ser. **127**, 527 (2000).

79. J. MacFarlane *et al*., presented at the 34th Meeting of the Division of Atomic, Molecular and Optical Physics, Boulder, CO, 20–24 May 2003 (Paper J1.181).

80. P. A. Keiter *et al*., Rev. Sci. Instrum. **79**, 10E918 (2008).

81. D. G. Stearns *et al*., Rev. Sci. Instrum. **57**, 2455 (1986).

82. D. G. Stearns *et al*., Rev. Sci. Instrum. **60**, 363 (1989).

83. D. K. Bradley *et al*., Rev. Sci. Instrum. **66**, 716 (1995).

84. C. R. Danly *et al*., Rev. Sci. Instrum. **86**, 043503 (2015).

85. P. L. Volegov *et al*., J. Appl. Phys. **118**, 205903 (2015).

86. I. V. Igumenshchev, F. J. Marshall, J. A. Marozas, V. A. Smalyuk, R. Epstein, V. N. Goncharov, T. J. B. Collins, T. C. Sangster, and S. Skupsky, Phys. Plasmas **16**, 082701 (2009).

87. G. Kagan and X.-Z. Tang, Phys. Lett. A **378**, 1531 (2014).

88. P. Amendt *et al*., Phys. Rev. Lett. **105**, 115005 (2010).

89. H. W. Herrmann, J. R. Langenbrunner, J. M. Mack, J. H. Cooley, D. C. Wilson, S. C. Evans, T. J. Sedillo, G. A. Kyrala, S. E. Caldwell, C. S. Young, A. Nobile, J. Wermer, S. Paglieri, A. M. McEnvoy, Y. Kim, S. H. Batha, C. J. Horsfield, D. Drew, W. Garbett, M. Rubery, V. Yu. Glebov, S. Roberts, and J. A. Frenje, Phys. Plasmas **16**, 056312 (2009).

90. J. R. Rygg, J. A. Frenje, C. K. Li, F. H. Séguin, R. D. Petrasso, J. A. Delettrez, V. Yu. Glebov, V. N. Goncharov, D. D. Meyerhofer, S. P. Regan, T. C. Sangster, and C. Stoeckl, Phys. Plasmas **13**, 052702 (2006).

91. W. R. Peltier and C. P. Caulfield, Annu. Rev. Fluid Mech. **35**, 135 (2003); J. D. Woods, J. Fluid Mech. **32**, 791 (1968).

92. D. P. Lathrop and C. B. Forest, Phys. Today **64**, 40 (2011); H. Xu *et al*., Astrophys. J. Lett. **698**, L14 (2009); S. A. Balbus and J. F. Hawley, Rev. Mod. Phys. **70**, 1 (1998); T. Ebisuzaki, T. Shigeyama, and K. Nomoto, Astrophys. J. Lett. **344**, L65 (1989); I. Hachisu *et al*., Astrophys. J. Lett. **358**, L57 (1990).

93. T. Yabe, H. Hoshino, and T. Tsuchiya, Phys. Rev. A **44**, 2756 (1991); N. J. Zabusky, Annu. Rev. Fluid Mech. **31**, 495 (1999).

94. Y. Zhou *et al*., Phys. Plasmas **10**, 1883 (2003); Y. Zhou, H. F. Robey, and A. C. Buckingham, Phys. Rev. E **67**, 056305 (2003); Y. Zhou, Phys. Plasmas **14**, 082701 (2007).

95. S. A. Slutz *et al*., Phys. Plasmas **17**, 056303 (2010).

96. M. R. Gomez *et al*., Phys. Rev. Lett. **113**, 155003 (2014).

97. *LLE Review Quarterly Report* **140**, 315, Laboratory for Laser Energetics, University of Rochester, Rochester, NY, LLE Document No. DOE/NA/1944-1202 (2014). Copies may be obtained from the National Technical Information Service, Springfield, VA 22161.

98. *LLE Review Quarterly Report* **96**, 284, Laboratory for Laser Energetics, University of Rochester, Rochester, NY, LLE Document No. DOE/SF/19460-509, NTIS Order No. PB2006-106668 (2003). Copies may be obtained from the National Technical Information Service, Springfield, VA 22161.

99. J. L. Leray *et al*., IEEE Trans. Nucl. Sci. **59**, 1289 (2012).

100. *LLE Review Quarterly Report* **136**, 313, Laboratory for Laser Energetics, University of Rochester, Rochester, NY, LLE Document No. DOE/NA/28302-1142 (2013). Copies may be obtained from the National Technical Information Service, Springfield, VA 22161.

101. J. L. Bourgade *et al*., Rev. Sci. Instrum. **72**, 1173 (2001).

102. J. L. Bourgade, V. Allouche, J. Baggio, C. Bayer, F. Bonneau, C. Chollet, S. Darbon, L. Disdier, D. Gontier, M. Houry, H. P. Jacquet, J.-P. Jadaud, J. L. Leray, I. Masclet-Gobin, J. P. Negre, J. Raimbourg, B. Villette, I. Bertron, J. M. Chevalier, J. M. Favier, J. Gazave, J. C. Gomme, F. Malaise, J. P. Seaux, V. Yu. Glebov, P. Jaanimagi, C. Stoeckl, T. C. Sangster, G. Pien, R. A. Lerche, and E. Hodgson, Rev. Sci. Instrum. **75**, 4204 (2004).

103. J. L. Leray, S. Bazzoli, J. E. Sauvestre, and V. Yu. Glebov, IEEE Trans. Nucl. Sci. **55**, 3060 (2008).

104. J.-L. Leray *et al*., in *3rd International Conference on Advancements in Nuclear Instrumentation Measurement Methods and Their Applications (ANIMMA)* (IEEE, Marseille, France, 2013), pp. 1–8.